

Neutrinos from gamma-ray bursts, and the multi-messenger connection

Dissertation zur Erlangung
des naturwissenschaftlichen Doktorgrades
der Julius-Maximilians-Universität Würzburg



vorgelegt von
Philipp Baerwald
aus Marburg

Würzburg, 2013

Eingereicht am: 30.09.2013
bei der Fakultät für Physik und Astronomie

1. Gutachter: Priv.-Doz. Dr. Walter Winter
2. Gutachter: Prof. Dr. Friedrich Röpke
3. Gutachter:
der Dissertation.

1. Prüfer: Priv.-Doz. Dr. Walter Winter
2. Prüfer: Prof. Dr. Friedrich Röpke
3. Prüfer: Prof. Dr. Raimund Ströhmer
im Promotionskolloquium.

Tag des Promotionskolloquiums: 17.12.2013

Doktorurkunde ausgehändigt am:

Kurzzusammenfassung

In dieser Arbeit beschäftigen wir uns mit dem Zusammenhang von Gammablitz (GRBs) und ultra-hochenergetischer kosmischer Strahlung (UHECR) sowie mit den Möglichkeiten, wie dieser Zusammenhang überprüft werden kann. Der zur Zeit erfolgsversprechendste Ansatz basiert auf der Detektion von hochenergetischen Neutrinos, die mit der Beschleunigung von kosmischer Strahlung assoziiert werden. Wir zeigen detailliert, wie die prompte Emission im Bereich der Gammastrahlung mit der Voraussage eines Neutrinosignals zusammenhängt. Ein besonderes Augenmerk legen wir hierbei auf die Wechselwirkung von Photonen und Protonen. Am Beispiel der aktuellen Analyse des ANTARES Neutrinoobservatoriums zu Neutrinos von Gammablitz zeigen wir, wie sich numerische Voraussagen von älteren analytischen Methoden unterscheiden. Des Weiteren diskutieren wir Möglichkeiten, wie die Teilchen der kosmischen Strahlung aus einem Gammablitz entkommen können, wenn die ultra-hochenergetische kosmische Strahlung nur aus Protonen bestehen würde. Wir vergleichen dazu das meistens angenommene Entkommen in Form von Neutronen mit einer neuen Komponente von direkt ausströmenden Protonen. Auch zeigen wir, dass die unterschiedlichen Komponenten, die zur kosmischen Strahlung beitragen, stark von den verwendeten Parametern der Gammablitz abhängen, und überprüfen die Modelle an einigen ausgewählten Gammablitz. In einem weiteren Schritt führen wir die Überlegungen zu dem Zusammenhang von Gammablitz und ultra-hochenergetischer kosmischer Strahlung fort, in dem wir mittels eines einfachen Propagationscodes für kosmische Strahlung eine Verbindung zwischen dem Quellmodell für Gammablitz und den Beobachtungsdaten der kosmischen Strahlung herstellen. Wir überprüfen, inwieweit sich die beobachteten Energiedichten der kosmischen Strahlung mittels unseres einfachen Modells realisieren lassen und welche Konsequenzen dies für die Voraussagen der prompten Neutrinoemission von Gammablitz sowie den kosmogenischen Neutrinos hat. Außerdem gehen wir der Frage nach, wie die vorausgesagten prompten Neutrinoemissionen von einer endlichen Lebenszeit der Neutrinos beeinflusst werden würden. In einem letzten Kapitel übertragen wir das verwendete grundlegende Quellmodell mit photohadronischen Wechselwirkungen auf eine andere Klasse von Quellen, am Beispiel von Voraussagen für den Mikroquasar Cygnus X-3.

Abstract

In this work, we take a look at the connection of gamma-ray bursts (GRBs) and ultra-high-energy cosmic rays (UHECR) as well as the possibilities how to verify this connection. The currently most promising approach is based on the detection of high-energy neutrinos, which are associated with the acceleration of cosmic rays. We detail how the prompt gamma-ray emission is connected to the prediction of a neutrino signal. We focus on the interactions of photons and protons in this regard. At the example of the current ANTARES GRB neutrino analysis, we show the differences between numerical predictions and older analytical methods. Moreover, we discuss the possibilities how cosmic ray particles can escape from GRBs, assuming that UHECR are entirely made up of protons. For this, we compare the commonly assumed neutron escape model with a new component of direct proton escape. Additionally, we will show that the different components, which contribute to the cosmic ray flux, strongly depend on the burst parameters, and test the applicability on some chosen GRBs. In a further step, we continue with the considerations regarding the connection of GRBs and UHECR by connecting the GRB source model with the cosmic ray observations using a simple cosmic ray propagation code. We test if it is possible to achieve the observed cosmic ray energy densities with our simple model and what the consequences are regarding the prompt GRB neutrino flux predictions as well as the cosmogenic neutrinos. Furthermore, we consider the question of neutrino lifetime and how it affects the prompt GRB neutrino flux predictions. In a final chapter, we show that it is possible to apply the basic source model with photo-hadronic interactions to other types of sources, using the example of the microquasar Cygnus X-3.

*“Dicebat Bernardus Carnotensis nos esse quasi nanos gigantum umeris insidentes,
ut possimus plura eis et remotiora videre, non utique proprii visus acumine, aut
eminentia corporis, sed quia in altum subvehimur et extollimur magnitudine
gigantea”*

*“Bernhard von Chartres sagte, wir seien gleichsam Zwerge, die auf den Schultern
von Riesen sitzen, um mehr und Entfernteres als diese sehen zu können – freilich
nicht dank eigener scharfer Sehkraft oder Körpergröße, sondern weil die Größe der
Riesen uns emporhebt.”*

– Johannes von Salisbury: *Metalogicon* 3,4,46-50

Contents

1. Introduction	1
1.1. Gamma-ray bursts	5
1.1.1. Historical overview and basic models	5
1.1.2. The internal shock model	10
1.2. High-energy neutrinos	17
1.2.1. Properties of neutrinos	17
1.2.2. Detection methods for astrophysical neutrinos	20
2. Neutrino flux predictions based on GRB data	25
2.1. The Waxman-Bahcall approach for neutrino spectra from GRBs	25
2.2. The Guetta et al. model and its extensions	28
2.3. The NeuCosmA model	30
2.4. Statistical effects affecting neutrino flux predictions	41
2.5. The current ANTARES GRB neutrino analysis	50
3. Models for UHECR escape from GRBs	57
3.1. The classic neutron escape model for CR escape	57
3.2. Possible leakage of CR protons from GRBs	59
3.3. Identifying different CR escape regimes	64
3.4. Application to specific GRBs	72
4. Probing GRBs as the sources of UHECR	77
4.1. A simple framework for CR injection and propagation	77
4.2. The combined results for UHECR, prompt GRB neutrinos, and cosmogenic neutrinos	83
5. Effect of neutrino lifetime	87
5.1. The redshift-dependent decay framework	87
5.2. The effect of decay on GRB neutrino fluxes	90
6. An example for neutrinos from microquasars	97
7. Summary and conclusions	101
8. Outlook	105
A. NeuCosmA	121
B. Cosmology and special relativity effects	124
C. Photon-photon interactions	129

1. Introduction

Even though it has already been more than 100 years since the discovery of the cosmic rays through Rudolph Hess [1], the question of their origin still remains. Different experiments over the years have refined the picture of the (nearly) unperturbed power-law extending over more than 12 orders of magnitude, see Fig. 1.1 as well as discussion in, *e.g.*, Ref. [2]. Even the theoretically predicted cutoff [3, 4] (“GZK-cutoff”) at energies beyond 10^{11} GeV is now considered to have been observed as recent updates from air shower experiments, see in Ref. [5] and references therein, suggest. There is now the accepted view that there are two distinct components: a galactic and an extra-galactic. The lower energies are assumed to be dominated by galactic sources, while the highest energies can only be reached on scales beyond the size of our galaxy, see, *e.g.*, Ref. [6]. However, the actual sources of the ultra-high-energy cosmic rays (UHECR) have so far not been identified. There are several models for known source classes based on their observation in photons. Some of these models include the acceleration of charged particles, such as electrons and protons, to the observed energies. Still, the mere existence of promising candidate models is not sufficient. A clear correlation of a charged cosmic ray and such a suggested source is still an open issue, which is complicated by the deflection of the charged particles in the intergalactic as well as galactic magnetic fields. Hence, we (so far) cannot identify the sources of cosmic rays based on the observations in photons.

To overcome this problem, current searches for astrophysical sources are being extended to include new messengers which are connected to the “classic” messengers, photons and CR. Here, the most promising new messengers are neutrinos, with the properties of neutrinos being their main advantage. Neutrinos are electrically neutral and nearly massless particles which only interact via weak interactions. Due to these properties, they can travel unperturbed over long distances through space. Other than the charged cosmic rays, they are not deflected by magnetic fields. Also, they do not get absorbed by matter, such as intergalactic dust, which is a major advantage over photons of various frequencies. In astrophysical sources, there are several mechanisms considered which can lead to the production of neutrinos. One is of course the production of neutrinos during the fusion processes inside stars. These neutrinos from fusion processes are at an energy of eV to MeV, depending on the actual process. At slightly higher energies, still several MeV, there are the supernova neutrinos, such as the ones detected from SN1987A [8, 9]. However, when discussing even higher energies, generally two possibilities to produce UHE neutrinos are considered. The first possibility is the interaction of two protons (pp interactions) leading to the production of pions and subsequent decay into neutrinos. For energies close to (but not directly at) the threshold of inelastic scattering, the

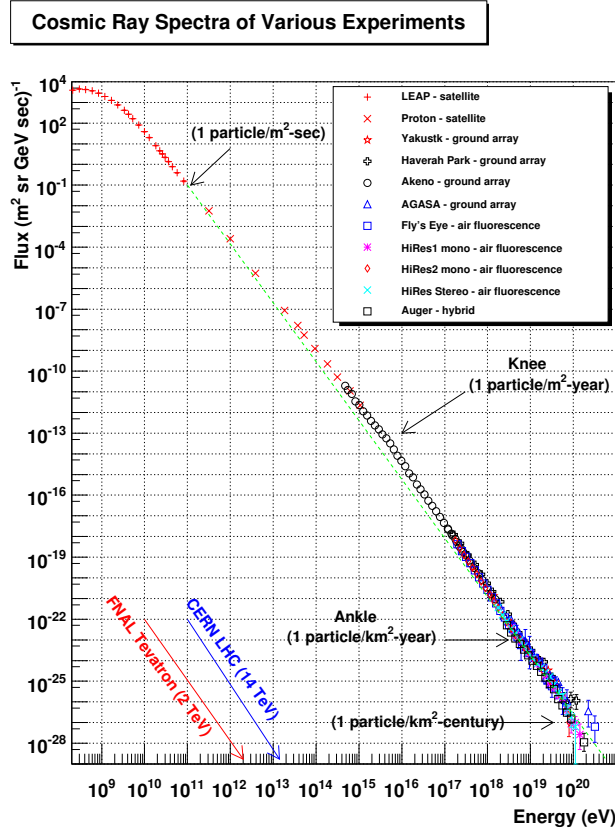


Figure 1.1.: The cosmic ray flux over energy. The graph shown here was created by W. Hanlon [7], based on the famous Swordy-plot [2].

pp interaction cross section is dominated by

$$p + p \rightarrow p + \Delta^+ \rightarrow \begin{cases} p + n + \pi^+ & 1/3 \text{ of all cases} \\ p + p + \pi^0 & 2/3 \text{ of all cases} \end{cases}, \quad (1.1)$$

with additional processes such as fragmentation into multiple pions gaining importance at higher energies, see, *e.g.*, discussion in Ref. [10]. The high-energy processes lead to a roughly equal number of π^+ to π^- , which is not given for the Δ^+ -resonance. These kinds of interactions are thought to be the dominant type of interaction in some active galaxy nuclei (AGN) or in some supernova remnants (SNR). Even though most of the observed spectra suggest a leptonic jet according to current emission models, there are also some examples for hadronic dominated jets. On the other hand, there is always the possibility of interactions of protons and photons as long as both types of particles are present at sufficiently high energies and densities. These photohadronic ($p\gamma$) interactions are most of the time approximated by the dominating $\Delta(1232)$ -resonance, leading to the simple reaction chain:

$$p + \gamma \rightarrow \Delta^+ \rightarrow \begin{cases} n + \pi^+ & 1/3 \text{ of all cases} \\ p + \pi^0 & 2/3 \text{ of all cases} \end{cases}. \quad (1.2)$$

In both pp and $p\gamma$ interactions, the neutrinos are produced in the decay of the charged pions, *i.e.* in the formulas shown above due to π^+ . This leads to a basic

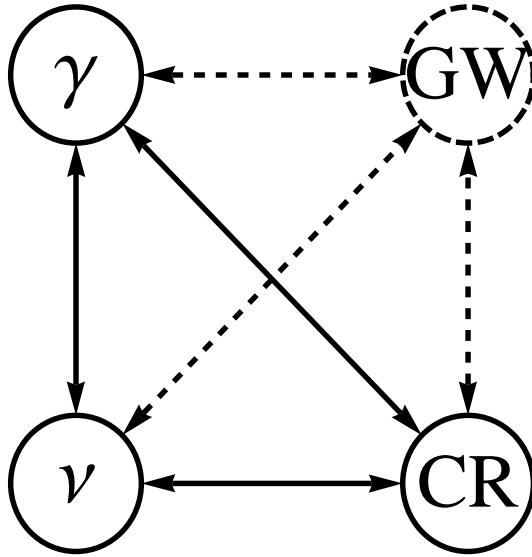


Figure 1.2.: This sketch depicts the basic concept of current multi-messenger physics. Currently, the triangle of cosmic rays (CR), photons (γ), and neutrinos (ν) is a popular picture in the literature. Due to the first detection of cosmic neutrinos, see Refs. [12, 13], the idea of combining several types of messengers has gotten a huge boost. Especially, the connection of the “classical” messengers CR and several wavelengths of γ with “new” messengers, such as ν , is currently a field of great research interest. However, to also pay respect to the work done in connection with short GRB, the depiction here is extended by the gravitational waves (GW).

connection neutrinos, photons, and cosmic rays, as depicted schematically in Fig. 1.2. In said figure, each type of messenger is represented by a circle, with the arrows representing the connection based on the (particle) physics involved in the source model. This interplay of the three different messengers is often depicted as a triangle. Here, we have however chosen an extended version which also includes gravitational waves (GW), due to recent work in this field, see, *e.g.*, Ref. [11] for a review. The connection of GW to the other messengers is a bit more complicated and ambiguous, which is represented by the dashed arrows. We will, nonetheless, focus only on the neutrinos in following.

To detect these high-energy neutrinos, gigantic neutrino telescopes, such as ANTA-RES [14] or the first $\mathcal{O}(1 \text{ km}^3)$ -telescope IceCube [15], are needed. Especially, the possible detection of the first 28 ultra-high-energy cosmic neutrino events, recently reported by the IceCube collaboration, see Refs. [12, 13], has sparked lots of interest in the community, see *e.g.* Refs. [16, 17, 18, 19, 20, 21, 22, 23, 24, 25, 26, 27, 28]. However, as Lipari pointed out in Ref. [28], one of the main challenges for the detection of astrophysical neutrinos remains the separation of the signal neutrinos from the background of so-called atmospheric muons and neutrinos, which are created in shower events in the Earth’s atmosphere. These backgrounds can however be reduced by cuts on the recorded data. Especially information on incident direction as well as the expected timing of an event can help to distinguish a neutrino sig-

nal from the atmospheric background. Here, transient events are one possibility to obtain both information on the direction as well as the timing. Examples for transient sources are flares of active galaxy nuclei (AGN) or microquasars (MQ), and gamma-ray bursts (GRBs). In the work presented here we will focus on GRBs.

In the about 50 years since their discovery, GRBs have been a mystery. They were only discovered by chance by the American VELA satellites, which were designed to monitor nuclear tests on Earth. Due to the confidentiality of the data, it took years till this discovery was made public [29]. In the subsequent time, a plethora of possible models for GRBs was created and numerous satellite missions were launched to study these phenomena. Based on the isotropic distribution of the recorded data, it could be deduced that these events could be of extragalactic origin. This was later confirmed by optical afterglow measurements, which allowed for the calculation of the bursts redshift. Today, there is the consensus that there are at least two distinct types of burst which can be differentiated based on their spectral properties in photons. On the one hand, there are the so-called “long-soft” bursts (LSB), which have a long duration and relatively soft spectra (= comparably steep dropping spectra with few high-energy photons). Their duration was set to be longer than 2 seconds based on the BATSE data. On the other hand, there are “short-hard” bursts (SHB), which have a shorter duration but have a higher contribution from high-energy photons to the total spectrum. The current view is that the LSB are connected to the collapse of a massive star, supported by the connection of GRB to core-collapse supernovae (SN), see Refs. [30, 31]. The low number of observed afterglows for SHB is currently one of the limiting factors for identifying the source of these events, see Refs. [32, 33]. The currently most accepted theory is that short bursts are connected to the merger of two compact objects, such as a neutron star-neutron star (NS-NS) merger or a black hole-neutron star (BH-NS) merger. Due to the assumed nature of these events, they are a prime target as sources of gravitational waves, and extended multi-messenger searches. We will however focus on long bursts due to the more established nature of their progenitors, with recent work indicating a common progenitor for LSBs up to $z \simeq 8$ [34].

From a neutrino astrophysics point of view, the currently most popular model is the so-called fireball model. It describes a GRB as the result of the relativistic expansion of a plasma (fire-)ball [35, 36, 37]. Based on ideas developed for expanding radio sources, this model gives a relatively simple description of how the observed radiation is enhanced due to relativistic boosting. What exactly produces the radiation is not fixed in the most generic version of this model. There are however extensions of the fireball model such as the internal shock model which introduces the collision of ejected shells among themselves [38, 39, 40]. These collisions lead to the creation of collision-less shocks and give rise to Fermi acceleration of the charged particles inside the shell. The accelerated electrons then promptly lose their gained energy in form of synchrotron radiation which is then observed as the gamma-rays here on Earth. This description of the creation mechanism of the gamma-rays has however several caveats and does not describe all features seen in GRB light curves. Hence, there are several other models, such as photospheric emission models or magnetic reconnection models, see, *e.g.*, Refs. [41, 42] for reviews. Each model has its own advantages, with no model totally convincing the community at this stage.

1.1. Gamma-ray bursts

In the following sections, we will take a closer look at GRBs in general as well as their models. We will first go into the history of GRBs, and will review what is so far known about these objects. We will then have a closer look at the internal shock model for GRB fireballs. We also include a table of the commonly used quantities at the end of this section.

1.1.1. Historical overview and basic models

Of the different objects and events in the universe, gamma-ray bursts (GRBs) are among the most mysterious. Even though they are quite short lived compared to the lifetime of stars, they manage to outshine most known objects in that short time. Similar like supernovae can outshine their host-galaxy, GRBs outshine everything, including active galaxy nuclei (AGN). Their (isotropic equivalent) energy output over the few seconds of their prompt emission phase is of about the same order as a solar mass M_{\odot} ($\sim 2 \cdot 10^{54}$ erg). Nonetheless, nearly 50 years after the initial discovery of these bursts of gamma-radiation, we still do not know how these cataclysmic events are formed.

The initial detection of a GRB happened by chance through a satellite program of the US Department of Defense in 1967. The so-called *Vela* satellites were designed to monitor the abidance of the Nuclear Test Ban Treaty. For this purpose, they had omni-directional gamma-ray detectors to notice any nuclear explosions down on Earth. Even though the focus of the satellites was to monitor Earth, some detected signals could be identified as coming from outer space. Since the military could not identify the origin of these mysterious, short blips, the results were finally made public in 1973, see Ref. [29], six years after the initial detection. During that stage, the investigation of GRBs had two key issues, which limited the directional information: On the one hand, GRBs are quite rare and detection only happens by chance. This together with the short duration of the bursts make extensive measurements impossible. And on the other hand, it is impossible to focus gamma-rays with current technology in a way such as we can focus optical light. Even now, more than 40 years after the first detection, there are no sharp “images” in gamma-rays of the bursts. The ambiguity led to a plethora of models which tried to describe and in a sense explain the origin of GRBs, see *e.g.* Ref. [43]. However, it should take more than 25 years till astrophysicists could make another significant step deciphering these strange events.

The launch of the *Compton Gamma-Ray Observatory (CGRO)* in 1991 marked the start of a further important mission in the process of understanding GRBs. For a summary of the mission’s results, see Ref. [44]. Especially the all-sky survey for the BATSE instrument was of great interest, as the distribution of bursts across the sky was nearly isotropic with next-to-no dipole or quadrupole moments [45]. This was a clear indication that GRBs are not of galactic origin, with an origin from an extended galactic halo or even from cosmological distances possible. Moreover, the latter

possibility indicated that the energy output of the source must be enormous during a very short period of time. Based on the measured short-scale variations of the measured gamma-ray fluxes, it was deduced that also the interaction volume must be comparably small. One of the conclusions drawn from this observation was the consideration that GRBs must be related to relativistic effects, or more precisely with the formation of a relativistically expanding e^\pm - γ -fireball, similar to the relativistic expanding radio sources proposed by Rees in Ref. [46]. Due to several problems of this basic model, from the energy distribution over the actual duration¹ of a burst to the rapid variability of the observed light curves, an additional ingredient in the form of shocks needed to be introduced. The main motivation for this was the non-thermal energy distribution of the observed photons. In this “fireball shock scenario”, there are two possible reasons for the shocks: either the ejected material runs into the surrounding medium, as proposed by Meszaros and Rees [36], or the ejected material is made up of several components which can collide among each other, leading to the formation of internal shocks. As long as the densities of the colliding material is low enough that the shock region can be considered as optically thin, it is possible that the radiation can simply escape the source. An overview of these kinds of models can be found in reviews, such as Refs. [41, 42], and references therein.

A further step was done when the existence of lower energetic afterglows, a consequence of the external shocks in the generic fireball shock model, could be experimentally proven in 1997. The Italian-Dutch satellite *Beppo-SAX* was able to detect fading X-ray images connected to GRBs, see Ref. [48]. These X-ray images allowed for the extraction of the burst’s position after 4 to 6 hours of processing time. Hence it was possible to do follow-up observations in the optical or other wavelength bands, see *e.g.* Ref. [49]. The additional information gained from these multi-wavelength observations enabled the identification of possible host galaxies as well as the derivation of the burst’s redshift, thereby confirming the cosmological nature of the bursts, see Refs. [50, 51]. The next generation of satellites after the end of the *CGRO* and *Beppo-SAX* missions brought a further piece to the picture, by allowing even more accurate GRB afterglow measurements. The *HETE-2* satellite managed the first unambiguous association of a GRB with a SN, even though the delay between the initial detection of a burst and the afterglow measurements was still some hours. Nonetheless, GRB030329 could clearly be correlated to SN2003dh, see Refs. [30, 31].

Another significant wave of advances started with the launch of the *Swift* multi-wavelength afterglow satellite in 2004, see *e.g.* Ref. [52] and references therein. The great breakthrough of the mission was the capability to measure the afterglow within minutes of the initial detection of a burst. This finally enabled the measurement of the light curves during the transition phase between prompt emission and the

¹The definition of the duration T_{90} which we use in this work is taken from the *Fermi* Catalog [47]: “The 90% burst duration, in seconds. T90 measures the duration of the time interval during which 90% of the total observed counts have been detected. The start of the T90 interval is defined by the time at which 5% of the total counts have been detected, and the end of the T90 interval is defined by the time at which 95% of the total counts have been detected.”

afterglow. Also, due to the different instruments on board the satellite, a burst could be simultaneously measured in gamma-rays, X-rays, and in the optical. This feature led to the detection afterglows of short bursts, as it greatly enhanced the response in different wavelengths to a trigger, see Refs. [32, 33]. Moreover, the bursts detected by *Swift* broke through the symbolic barrier of $z = 6$ in redshift. Even though the number of bursts detected from redshifts $z \geq 6$ is quite small, the frontier has gradually shifted to higher values. Nowadays, with the *Fermi* satellite providing most of the data, the record stands at a redshift of $z = 9.35$ for GRB090429B, see Ref. [53]. While the *Swift* satellite was focused on connecting the gamma-rays to the lower-energetic photons, *Fermi* again focuses more on the gamma-rays themselves. The two instruments on board the satellite can detect bursts over nearly seven orders of magnitude, with nearly seamless transition among energy bands. The lower energy range from < 10 keV up to > 25 MeV is covered by the Gamma-ray Burst Monitor (GBM), which scans the whole sky at all times (minus the part occulted by Earth), taken from Ref. [47]. The upper part of the energy spectrum is covered by the second instrument, the Large Area Telescope (LAT). The LAT can detect events in the range from from 20 MeV up to 300 GeV, however, the field-of-view of the instrument is restricted to about 2 sr (20% of the full sky). Hence, the GBM is used to record pre-trigger information as well as acting as an “alert monitor” for the LAT. Depending on signals detected in the GBM, the whole satellite can be repositioned, allowing the LAT to detect the burst as well. Furthermore, the angular resolution of the LAT is much better than the one of the GBM ($< 0.5'$ to $\sim 3^\circ$), taken from Ref. [47]. Therefore the repositioning additionally helps with the localization of a burst. A current problem is, however, that the number of bursts actually detected in the LAT is quite low ($\sim 7\%$), see Ref. [54]. It is currently discussed if this is due to the spectra of most GRBs not extending to as high energies as initially thought or if this discrepancy is of other origin. One possible source of improved detection could come from the new PASS8 data analysis algorithm for the event reconstruction, see discussion in Ref. [55]. In a first analysis, this significantly increased the number of photon events for a limited sample of bursts detected in the LAT.

Based on the information gained from the different satellite experiments (and connected ground based measurements) mentioned in the previous paragraphs, it is now firmly believed that bursts are connected to the end of the life of certain kinds of stars and that there are at least two distinct populations of bursts, see reviews such as Refs. [41, 42]. The “long soft” bursts are considered to be connected to the core collapse of a massive star ($m \gtrsim 30 M_\odot$) to a black hole, based on the correlation to core-collapse supernovae, see Refs. [56, 37]. Recent work indicates that these bursts have a common type of progenitor up to $z \simeq 8$, see discussion in Ref. [34]. These bursts are generally identified to have a duration longer than 2 s. The bursts with a shorter duration are mostly “short hard” bursts, and are assumed to be connected to the merger of two compact objects. This can be either the merger of neutron star binaries (NS-NS) or neutron star-black hole (NS-BH) mergers which lead to the release of the observed radiation, see *e.g.* Refs. [57, 58] for model descriptions. The separation based on the duration is unfortunately not very accurate, depends on the chosen energy band, and also on the instrument doing the measurement. The value of 2 s was derived from the population studies done with the BATSE catalog, as detailed

in Ref. [59], and was still valid for newer BATSE catalogs such as Ref. [60]. This value unfortunately differs for other instruments, especially with different energy ranges. A nice comparison of this can be seen in Fig. 7 of Ref. [61]. Therefore, the duration may not be the best identifier of the two burst populations. However, the multi-wavelength data which is now available has introduced the spectral shape as an additional identifier. Depending on the amount of high-energy gamma-rays compared to the amount of low energy gamma-rays, bursts can also be classified as “soft” (most energy in lower energy ranges) or as “hard” (more high-energy emission). Still, the details of the models are still unclear apart from this. One important recent addition to the models was the introduction of jets. Especially for long bursts this feature helped to resolve problems with the energy budget of the fireball model. Compared to the previously assumed isotropic emission, the actual energy release significantly decreased when assumed to be coming from a jet. This assumption of GRBs being connected to jets is backed by observations of afterglows in X-rays as well as the optical. Several light curves in these energy bands show a break or steepening of the spectrum. This feature is interpreted as an edge effect as the ejecta slow down in the external medium. Due to relativistic beaming, it is not relevant if the emission is actually from a sphere or from a jet, as long as the jet opening angle $\theta_j > 1/\Gamma$, with Γ being the bulk Lorentz factor of the jet. When the jet slows down and Γ decreases, a point is reached where the light cone from the relativistic boosting is larger than the actual jet. At this stage, there is an observable difference between a sphere and a jet. In case of the sphere, it would be possible to “see” more parts of the sphere’s surface, partially countering the loss due to the lower Γ through a higher emission area. For a jet, these contributions from fainter outer parts are missing. The result is expected to be a break towards a steeper decline in the afterglow spectrum. The inferred jet opening angles of long GRBs are suspected to be in the range of $\theta_j = 5^\circ - 20^\circ$, which would be sufficient for assumed boost factors of about $\Gamma = 300$. A problem with obtaining these values is always that the actually correct description of a GRB jet is so far unknown, and that several models are still viable. Inside the relativistically boosted light cone the boost factor can actually vary by a factor of two based on the viewing angle. As already detailed by Meszaros in his review [42], Doppler boosting and Doppler factors should actually be used instead of the simple Lorentz factors. On top of that, the jet may be structured in one way or the other. However, for sake of simplicity we will assume a uniform jet and neglect the variation of the Doppler factor due to the viewing angle, using the Lorentz factors as done in the literature.

Nonetheless, there are currently three classes of models which are being discussed as the origin of the prompt gamma-ray emission of the bursts. There are the internal shock models, which we will focus on during this work and will be discussed in the next subsection, but there are also photospheric models as well as magnetic reconnection models, which all have their advantages and disadvantages. For photospheric emission models, the radiation is assumed to originate from thermal electrons inside the plasma, which was already part of the original fireball models, see Refs. [35, 62, 63]. As the fireball expands and the plasma heats up due to energy redistribution, the electrons also emit photons, see, *e.g.*, Ref. [64] for a current model. These thermal photons can again interact with the electrons via

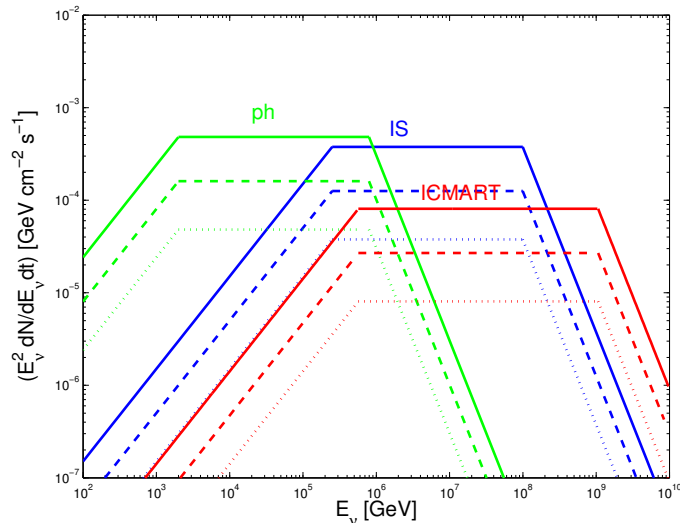


Figure 1.3.: Neutrino flux predictions for different GRB models taken from Zhang and Kumar [68]. Depicted are the color-coded predictions for a photospheric model (“ph”), an internal shock model (“IS”), and for the ICMART model. The prediction for each model is distinctly different.

Compton scattering. Especially Inverse Compton scattering can lead to high-energy photons. When the density of the plasma further decreases, the fireball reaches the so-called photospheric radius R_{ph} where the photons decouple from the plasma. This photospheric radius can actually be dependent on the wavelength of the photons. Multi-wavelength measurements indicate a delayed onset of the high-energy emission, as can be seen from *e.g.* the multi-wavelength observation of GRB110731A in Ref. [65]. Hence, it might be the case that the highest energy photons can only escape when the density of the burst has decreased due to the expansion of the burst. The production of neutrinos would also happen near this photospheric radius, which is smaller than the radius at which internal collisions are expected to happen, as discussed in Ref. [66]. On the other hand, the jet could also be powered by magnetic reconnection processes, such as in the Internal-Collision-Induced Magnetic Reconnection and Turbulence (ICMART) model by Zhang and Yan [67]. In these models, the turbulent reconnection of magnetic fields inside the plasma lead to an additional acceleration while also Inverse Compton scattering and internal collisions also play a role. The radius at which the photohadronic interaction happen here are expected to be larger than for the internal shock model. Moreover, the particle as well as energy densities for all three models are different, hence all three models give different predictions in neutrinos, as discussed by Zhang and Kumar [68], see Fig. 1.3. In said figure, the neutrino flux predictions for a photospheric model (“ph”, green curves), an internal shock model (“IS”, blue curves), and for the ICMART model (red curves). The prediction for the photospheric model is the highest in flux level, but at the lowest neutrino energies. The prediction for the internal shock model is only slightly lower, but at significantly higher energies. The ICMART model predicts even higher energies for the neutrinos, but the flux is lower. It should therefore be possible to distinguish the different models based on the neutrino observations.

1.1.2. The internal shock model

In the internal shock model, the radiation is assumed to come from shock accelerated electrons which lose their energy due to synchrotron radiation. The acceleration of the electrons is assumed to occur due to the collision of different matter shells, which in turn had been ejected by a central engine. Based on the geometry of a burst and several general considerations, it is possible to derive most of the parameters which are connected to this model. While basic forms of the internal shock model were proposed in Refs. [38, 39, 40], we use the basic description and considerations given in Ref. [69] as well as Ref. [70].

The basic assumption of the fireball model is that a central engine ejects shells of a certain thickness. These shells all have different bulk velocities Γ , with the range of variation among Lorentz factors being of the order of $\Delta\Gamma/\Gamma \sim 1$. Technically, the shells get accelerated till they reach their maximal velocity at their photospheric radius and then start to coast with a constant bulk velocity. At a later stage, the shells start to overtake each other giving rise to collisions. The distance from the central engine where this happens is called the collision radius R'_c (in the shock rest frame (SRF)). The value of this radius can be calculated from the observed variability time t_v of the light curves, as explained in Refs. [69, 70]:

$$R'_c \simeq 2\Gamma^2 c \frac{t_v}{1+z} \quad . \quad (1.3)$$

In the formula shown above, we have already extended the original formula by the contribution of the redshift z . We will include the redshift in all necessary formulas and we give a quick review why this is necessary in Appendix B. For the currently inferred values of the Lorentz factor Γ together with the obtained values of z , it can be assumed that $R'_c \simeq 10^{13} - 10^{14}$ cm, with c in Eq. (1.3) being the speed of light. Before continuing with the description of the internal shock model, we first want to explain why R'_c is primed, while other units, such as t_v , are not. In this work, we will be using a number of different frames of reference, which we will denote distinctly. The first frame is the aforementioned shock rest frame (SRF), denoted by primed units; x' . As the name suggests, it is the frame in which the shock, which is assumed to effectively give rise to the gamma-rays, is at rest. Moreover, an important property of this frame is that the emitted photon spectrum as well as other particle spectra are isotropic. This will become relevant, when we discuss the particle physics in more detail in Sec. 2.3. The second frame is the observer's frame, which is the frame in which the actual observations are done. Unprimed units denote quantities in the observer's frame; x . Since we also need to take into account the effects of the cosmological expansion, we additionally need a third frame, which connects the other two frames. For this we use the so-called source frame. It is connected to the SRF through Lorentz transformations, while the observer's frame and the source frame are connected via z . We denote quantities in the source frame with a tilde; \tilde{x} .

The thickness of a shell can also be estimated based on causality, with the short scale variations being assumed to reflect the size of a causally connected region,

namely a shell. Hence, the size of a shell can be estimated to be

$$\Delta R' \simeq \Gamma c \frac{t_v}{1+z} \quad , \quad (1.4)$$

which is similar to the collision radius. A basic depiction (and description) of how these quantities are derived can be found in, *e.g.*, Ref. [71]. For all basic (neutrino) calculations, as in Ref. [70], it has been assumed that these quantities are fixed and do not evolve with time. For the following description of the other quantities, we will assume that these parameters do not evolve. We will, however, discuss in Sec. 3.2 how our picture changes when parameters can evolve with time.

The two aforementioned length scales both depend on the so-called variability time t_v . In theory, a relatively simple connection between the observed variability and the geometry of the burst exists. However, it is most of the time not as certain what actually is the fastest variation or if the variations are really induced by the geometry or not. In the picture of the prompt emission coming from a larger number of shells, it might also be possible that the observed variations are due to different shell thicknesses, different distances between shells, or due to collisions with different relative velocities. Hence, this temporal variation of the spectrum is different for each burst, and can even differ among energy bands. These differences among energy bands might be due to an effect introduced by the measurement process or some aspect of the emission process which is not understood yet. In summary, one has to admit that there is no clear definition of t_v so far, but work is currently being done on this aspect, see *e.g.* Ref. [72]. Typical values for t_v are normally cited to range from $\sim 10^{-3}$ s up to 1 s, see Ref. [73].

The second parameter defining the two length scales given in Eqs. (1.3) and (1.4) is the bulk Lorentz factor Γ . Similar to the group velocity in a wave packet, the Lorentz factor Γ describes the collective motion of the ejecta. Depending on the scale that is considered, the equivalent to the phase velocity is now either the velocities of the different particles or even the velocities of individual shells. According to Ref. [69], the ejecta are assumed to be accelerated due to energy transfer between the photon and the particle fields, until a maximum is reached. The upper bound for this acceleration is normally estimated by assuming that all energy has been transferred to kinetic energy. At this stage, it is assumed that the photons decouple from the plasma, at the so-called photospheric radius R_{ph} . Beyond this point, the shells are assumed to coast with constant velocity (or Γ). During this coasting phase, the shells start to collide, which is assumed to start at the aforementioned collision radius R_c from Eq. (1.3). The shells can further collide during propagation until they get decelerated when running into the external medium, at a radius R_{ext} ; $R_{\text{ext}} \gg R_c \gg R_{\text{ph}}$. For simplicity reasons, it is normally assumed that all collisions happen at the fixed radius R_c , which we will also adopt for the most part of this work. As mentioned before, we will briefly discuss the effect of the propagation in Sec. 3.2, but more realistic models in the future should incorporate this evolution. Nonetheless, deriving values of Γ from the available photon data is somewhat problematic. Even though there are a number of methods which attempt to derive Γ from observations, none has fully convinced so far. The usually used method is founded on the constraints due to the pair creation threshold for high-energy emission, based

on Ref. [74]. In said reference, it is discussed that a Lorentz factor $\Gamma \gtrsim 100$ is needed to ensure that the source is optically thin to non-thermal high-energy photons. This estimate facilitates the consideration that the calculation simplifies when boosting to the SRF. Hence, it is possible to estimate the minimal Γ needed to just reach the threshold for e^\pm -pair production inside the source using the highest observed photon energy of a burst. We will discuss this pair creation cutoff in a bit more detail in Appendix C, however in the context of the maximal escaping photon energy, not for the estimation of the Lorentz factor. On the other hand, Γ can also not be much higher than 1000 as it would lead to significant synchrotron losses of the protons, see Ref. [75]. Other methods which try to derive Γ from the observational data are the afterglow onset method [76], the early external forward emission method [77], as well as the attempt of deriving a correlation of Γ and $L_{\gamma,\text{iso}}$ for a simpler determination of Γ , see Ref. [78]. In the influential GRB neutrino paper by Guetta et al. [70], a method similar to the pair creation cutoff from Ref. [74] is used. Instead of focusing on the not well known maximal escaping photon energy, the method in Ref. [70] utilizes the observed break energy of the photon spectrum. With their approach the authors obtained that the most common Lorentz factor is $\Gamma \simeq 300$.² This value of $\Gamma \simeq 300$ (or $\Gamma \simeq 10^{2.5}$) has been adopted as the standard value of the Lorentz factor in the literature, see *e.g.* Refs. [42, 70, 73, 75].

Apart from Γ and t_v , there are a number of other quantities which can be derived from the observed light curve. In Table 1.1, we have listed most of the commonly used quantities together with a short definition of each quantity. The different parameters listed in the table also have (if known) their “standard” values listed, such as $\Gamma = 300$ or $t_v = 10^{-2}$ s. For most bursts, the observed photon spectrum follows the so-called Band functions [80] which is essentially a broken power-law. Therefore, the properties of the photon spectrum can be defined by the break energy $\varepsilon'_{\gamma,b}$ (in the SRF), and the lower and the upper photon spectral index α_γ and β_γ , respectively. These quantities can be found in Table 1.1 as well as the (photon) flux F_γ and the fluence \mathcal{F}_γ , which normalize the spectra. As is detailed in the descriptions inside Table 1.1, there are several possibilities to define the flux. Essentially, the flux is the amount of energy detected per unit time per unit area. However, depending on the chosen energy range as well as the time interval, the result can vary. Due to the variation in time, it is sometimes of interest to have knowledge of the highest (“peak”) flux $F_{\gamma,p}$ during the whole duration T of a burst. On the other hand, sometimes the time variations are not of interest at all and the total energy deposited per unit area during the duration is needed. This is given by the fluence \mathcal{F}_γ and is essentially just F_γ integrated over time. The effect of the energy range is either treated by specifying the energy range or by using a bolometric value, such as $\mathcal{F}_{\gamma,\text{bol}}$, which is defined over the whole energy range. When additionally the distance to the GRB is known (via the redshift z , see discussion in Appendix B), F_γ can be used to calculate the

²On a only partially related note, it is quite peculiar that the actual distribution of the Lorentz factors of GRBs obtained in Ref. [70] and the distribution of Doppler factors of AGN jets shown in Fig. 3 of Ref. [79] are of similar shape. This might be a hint towards a basic underlying concept for all relativistic jets, and that the actual boost factors involved in GRB observations should be Doppler factors, not pure Lorentz factors. Unfortunately, at this stage this is pure speculation.

luminosity $L_{\gamma,\text{iso}}$ for an assumed isotropic source. Moreover, the isotropic equivalent energy $E_{\gamma,\text{iso}}$ can be calculated with this approach. As stated before, the isotropic equivalent energy should be corrected by the size of the jet (compared to a full sphere), but this can be neglected for general calculations due to the relativistic boosting. During this work, we will regularly refer to the values found in Table 1.1 to describe our basic internal shock fireball model.

With the knowledge of the energy $E_{\gamma,\text{iso}}$ or the luminosity $L_{\gamma,\text{iso}}$ of a burst as well as the volume of the shells, based on the collision radius and the shell thickness, it is also possible to calculate the energy density inside the burst. Even though we only have observation data in photons, it is possible to derive estimates for other energy densities such as the protons, which are assumed to carry the bulk of the (kinetic) energy. Another important component is, however, the magnetic field B . There is currently still some debate about the values of the magnetic field inside the shock regions of a burst. It was suggested in Ref. [81] that values in the range from 10^4 to 10^7 G should be expected for GRBs. As we discussed in Ref. [82], a detailed detection of the neutrino flux shape could give insight on the magnetic field values. As this is not yet possible, partition arguments are normally used to estimate the magnetic field. Based on afterglow measurements, equipartition between the photons and the magnetic field is assumed, see Refs. [83, 84]. With this approach, it is possible to estimate that the energy density in electrons and/or photons U'_γ should be roughly the same as the energy density of the magnetic field U'_B . In turn, the energy density in $[\text{erg cm}^{-3}]$ can be used to calculate the magnetic field strength (in [G])³:

$$U'_B = \frac{B'^2}{8\pi} \quad . \quad (1.5)$$

One of the further results which can be derived from the connection of GRBs and core-collapse SN is that the distribution of GRBs in z should follow roughly the star formation history. Even though it is not clear what fraction of stars actually results in GRBs or if that fraction changes in z , it is much easier to obtain the star formation rate (SFR) compared to the GRB rate, solely based on observation statistics. Of the different existing SFR models, we will be using the parameterization suggested by Hopkins and Beacom [85], based on the initial mass function proposed by Baldry and Glazebrook, see Ref. [86]. In the work by Hopkins and Beacom, the star formation rate density $\dot{\rho}_*$ (in $M_\odot \text{Mpc}^{-3} \text{yr}^{-1}$) is given to be

$$\dot{\rho}_* \propto \begin{cases} (1+z)^{3.44} & 0 < z \leq 0.97 \\ 10^{1.09} \cdot (1+z)^{-0.26} & 0.97 < z \leq 4.48 \\ 10^{6.66} \cdot (1+z)^{-7.8} & 4.48 < z \leq 6 \end{cases} \quad , \quad (1.6)$$

where we left out the actual normalization constant $\dot{\rho}_*(0)$ on purpose, as it is effectively irrelevant for the GRB rate. The cutoff introduced by Hopkins and Beacom for the SFR at $z_{\text{max}} = 6$ is due to the lack of statistics at higher redshifts. Even

³We will use Gaussian cgs-units throughout this work, if not noted otherwise. This has the advantage that we can use relations such as $1 \text{ G} = 1 \sqrt{\text{erg cm}^{-3}}$. Moreover, we will be using the relation $1 \text{ erg} = 624.15 \text{ GeV}$.

though there are some bursts with higher measured z , it is still hard to probe regions beyond $z = 6$. Therefore, we will keep this cutoff in the work presented here. For the translation from SFR to number of GRBs in z , we will use the approach suggested by Kistler et al. [87], which is a continuation of Ref. [85]:

$$\frac{d\dot{N}}{dz} = F(z) \frac{\mathcal{E}(z) \dot{\rho}_*(z)}{\langle f_{\text{beam}} \rangle} \frac{dV/dz}{1+z} . \quad (1.7)$$

In this approach, several factors are incorporated, which can change the observed number of bursts from the actual distribution. The factor $F(z)$ represents the fraction of bursts which are either too faint to be observed or for which it is not possible to obtain a redshift value. For simplicity reasons, we will assume that this factor is one, as it is also has been discussed by the authors in Ref. [87]. The authors reasoned that for a high enough luminosity $L_{\gamma, \text{iso}}$ all bursts should be visible over the whole z range, which is being observed. Hence, $F(Z)$ would be just a constant, and only set by the probability to derive a z value for a burst. The factor $\langle f_{\text{beam}} \rangle$ takes into account the fraction of bursts which are not observable due to beaming effects. Moreover, Kistler et al. introduced the factor $\mathcal{E}(z)$ to parameterize the number of stars resulting in GRBs. By comparing a sample of GRBs to the result expected from Ref. [85], they concluded that $\mathcal{E}(z) = \mathcal{E}_0(1+z)^{1.2}$ is the best correction to the SFR to describe the observational data up to $z = 4$, but should also be applicable to higher redshifts, see Ref. [87]. Note that even in said reference \mathcal{E}_0 is not determined and kept as a free parameter, as we do as well. Nonetheless, this correction factor effectively implicates that the amount of star deaths resulting in GRBs is higher at high values of z . For the pure SFR, given in Eq. (1.6), the peak corresponds to the “typical value” of redshift for a GRB, $z = 1 - 2$, as stated in Ref. [73]. For the strong evolution case (with the correction factor $\mathcal{E}(z)$), the peak number of GRBs, however, shifts to $z = 2 - 3$. The last factor is the comoving volume correction given by

$$\frac{dV/dz}{1+z} = \frac{4\pi d_H d_{\text{com}}^2(z)}{(1+z) \sqrt{\Omega_m(1+z)^3 + \Omega_\Lambda}} , \quad (1.8)$$

which is a consequence of the cosmological model. Here, we use the Hubble distance $d_H \approx 4.26$ Gpc, the comoving distance d_{com} (as defined in Eq. (B.8) in Appendix B), and the densities $\Omega_m = 0.27$ and $\Omega_\Lambda = 0.73$, as given in Table B.1. An explanation of the different factors can be found in Appendix B. Moreover, it is useful for several calculations to define an adimensional redshift evolution function $\mathcal{H}(z)$ by normalizing the GRB rate density, from Eq. (1.6), with the local rate density, leading to

$$\mathcal{H}(z) = (1+z)^\alpha \frac{\dot{\rho}_*(z)}{\dot{\rho}_*(0)} , \quad (1.9)$$

where the additional factor $(1+z)^\alpha$ is also included, to allow for different redshift scaling, as in Ref. [87]. As stated earlier, when using this function, the local rate $\dot{\rho}_*(0)$ is not needed, as it drops out through the normalization $\mathcal{H}(z=0) = 1$.

Name	Symbol	Units	Definition
Fluence	\mathcal{F}_γ	erg cm^{-2}	time integrated radiative flux (depends on energy band); energy per unit area
Fluence_25_1000	\mathcal{F}_{25}	erg cm^{-2}	time integrated radiative flux in the 25 – 1000 keV energy band; energy per unit area
Bolometric fluence	$\mathcal{F}_{\gamma,\text{bol}}$ (or S_{bol})	erg cm^{-2}	time integrated radiative flux integrated over whole energy range (or summed over all energy bands); energy per unit area
Flux	F_γ	$\text{erg s}^{-1} \text{cm}^{-2}$	radiative flux; energy per unit area and unit time
Peak flux	$F_{\gamma,p}$	$\text{erg s}^{-1} \text{cm}^{-2}$	highest radiative flux in a one second interval (during a burst)
Bolometric isotropic equivalent energy	$E_{\gamma,\text{iso,bol}}$	erg	equivalent energy of an emitting sphere derived from the observed bolometric photon fluence (integrated number of particles over energy) <i>typical value:</i> 10^{53} erg
Total isotropic equivalent energy	$E_{\text{iso,tot}}$	erg	equivalent energy of an emitting sphere in all “kinds” of energies, <i>i.e.</i> in e^\pm , p , B , or any other possible contribution
lower photon spectral index	α_γ	1	lower spectral index of the observed photon spectrum, assuming a broken power law or a Band function <i>typical value:</i> 1
upper photon spectral index	β_γ	1	upper spectral index of the observed photon spectrum, assuming a broken power law or a Band function <i>typical value:</i> 2
photon break energy	$\varepsilon'_{\gamma,b}$	keV	energy of the break in the power law spectrum (in the SRF), or peak energy in case of the Band function <i>typical value:</i> 1 keV

Continued on next page

Name	Symbol	Units	Definition
Burst duration	T	s	time between first and last recorded photon event of a burst
T-90 (T-45)	T_{90} (T_{45})	s	time during which 90% (45%) of the total energy are observed <i>typical value:</i> 10 s
Variability time	t_v	s	time of variation in (time resolved) flux spectrum (depends on energy band) <i>typical value:</i> 10^{-2} s
Isotropic equivalent luminosity	L_{iso}	erg s^{-1}	isotropic energy output through a sphere per unit time (nature of energy output not specified) <i>typical value:</i> $L_{\gamma,\text{iso}} = 10^{52} \text{ erg s}^{-1}$
L-90 (L-45)	L_{90} (L_{45})	erg s^{-1}	isotropic energy output through a sphere per unit time during period in which 90% (45%) of the total energy are observed (nature of energy output not specified)
Peak luminosity	L_p	erg s^{-1}	isotropic energy output through a sphere per unit time during highest flux period (nature of energy output not specified)
Photon energy density	U_γ	erg cm^{-3}	energy density in photons
Energy density of the magnetic field	U_B	erg cm^{-3}	energy density in the magnetic field
Redshift	z	1	cosmological distance measure <i>typical value:</i> 2
Lorentz factor	Γ	1	boost factor due to relativistic motion <i>typical value:</i> 300 (or $10^{2.5}$)

Table 1.1.: The commonly used quantities in the internal shock model for GRB fireballs with their symbols, their generally used units, and a short definition. The quoted typical values are all for long GRBs only. Moreover, the conversion $1 \text{ erg} = 624.15 \text{ GeV}$ is usually used to connect particle energies with energies of cosmic objects.

1.2. High-energy neutrinos

In the following sections, we want to discuss the neutrinos as particles themselves. We will first review the basic properties of neutrinos. We will give a short historical overview, followed by a brief introduction to neutrino mixing with its parameters. In a second section, we will discuss how neutrinos can actually be detected in telescopes and how the different flavors can be distinguished.

1.2.1. Properties of neutrinos

The neutrino, as a new particle, was proposed by W. Pauli in 1930 to resolve conceptual problems with the interpretation of the results of detailed radioactive decay measurements [88]. The term “neutrino” itself was only coined later by E. Fermi in 1934 to describe that the particle is electrically neutral (“neutr-”) while having a tiny interaction cross-section or mass (“-ino”, from Italian), see Ref. [89]. In principle, this already summarizes the most important properties of the neutrinos. Even though it took decades after the initial proposition of the neutrinos, we now know that they are spin-1/2 leptons associated with the three known lepton families; ν_e (discovered in 1956, see Ref. [90]), ν_μ (discovered in 1962, see Ref. [91]), and ν_τ (discovery finally announced in July 2000 by the DONUT collaboration [92]). The magnitude of the interaction cross-section can be attributed to the property of only being subject to weak interactions. Moreover, the Wu-experiment showed in 1956 that weak decays are maximally parity violating [93]. Only a year later, it was shown by the group of M. Goldhaber that the helicity of neutrinos is always left-handed, while anti-neutrinos are right-handed, see Ref. [94]. However, these results are nowadays causing problems as measurements of solar, atmospheric, reactor, and accelerator neutrinos in the last two decades have shown that there are discrepancies between the theoretical prediction and the actually measured fluxes.

The idea for resolving this discrepancies was proposed by B. Pontecorvo in 1957, see Refs. [95, 96], long before there was actual experimental proof of neutrino oscillations. However, similar to N. Cabibbo trying to preserve universality of weak interactions [97], Z. Maki, M. Nakagawa, and S. Sakata proposed a difference between the mass-eigenstates and the weakly interacting flavor-eigenstates to resolve problems with the observed leptonic decay rates of hyperons (baryons with at least one strange quark) [98]. Even though their initial proposal was only for two states, it is nowadays assumed that the flavor states $|\nu_\alpha\rangle$ with $\alpha = e, \mu, \tau$ are connected to the mass eigenstates $|\nu_j\rangle$ via a mixing matrix, see *e.g.* Ref. [99],

$$|\nu_\alpha\rangle = \sum_j U_{\alpha j}^* |\nu_j\rangle \quad . \quad (1.10)$$

The entries for the mixing matrix $U_{\alpha j}$ can be derived from neutrino oscillation experiments, with the actual size of the matrix also being subject of discussion. Current cosmological data, see *e.g.* Ref. [100], as well as the electroweak precision measurements of the Z -boson width (see Ref. [101] and references therein for current status)

suggest that there are only three “active” (weakly interacting) neutrino species, the aforementioned ν_e , ν_μ , and ν_τ . For these three active states, most of the neutrino oscillation data⁴ can be described with help of three mass eigenstates ν_j , *e.g.* ν_1 , ν_2 , and ν_3 . These mass eigenstates must be light, $\sum m_i < 0.85 \text{ eV}$ (conservative estimate from *Planck*-CMB data [100]) or $m < 2 \text{ eV}$ (taken from Ref. [101], from tritium decay), and not equal, $m_1 \neq m_2 \neq m_3$. Even though the exact mass of the different mass states is unknown, there is already quite a good handle on the mass squared difference Δm^2 , taken from Ref. [101], based on the 3-neutrino mixing scheme described in said review,

$$\begin{aligned} \Delta m_{21}^2 &= m_2^2 - m_1^2 = (7.50 \pm 0.20) \cdot 10^{-5} \text{ eV}^2 \quad , \\ |\Delta m_{31}^2| &= |m_3^2 - m_1^2| = (2.32_{-0.08}^{+0.12}) \cdot 10^{-3} \text{ eV}^2 \quad . \end{aligned} \quad (1.11)$$

The first mass difference, Δm_{21}^2 , is derived from the comparison of the measured solar neutrino flux to detailed theoretical calculations. Our model of the fusion chains inside the Sun predicts only the production of ν_e , while the measured ν_e flux here on Earth is significantly below the predicted amount. This discrepancy can however be resolved with the aforementioned mixing of the neutrino states, which allows for transitions among the flavor states during flight. The second mass difference, $|\Delta m_{31}^2|$, can be related to the flux of neutrinos produced by cosmic rays hitting the Earth’s atmosphere. In these interactions, mainly ν_μ are produced. Note that for this mass difference the sign is so far unknown. Due to this, there are two possible ordering schemes: one with ν_3 being the heaviest state (“normal hierarchy”), and one with ν_3 being the lightest one (“inverted hierarchy”).

Even though the experimental data has shown that neutrinos must have a mass, there is still the unknown element of how this mass is obtained. This problem is closely related to the fundamental question about the “nature” of neutrinos, *i.e.* if neutrinos are Dirac or Majorana fermions. In theory, the electric neutrality of neutrinos allows them to be their own anti-particle, based on the definition that anti-particles are the electric charge conjugate of a particle, such as the positron e^+ being the anti-particle of the electron e^- . If neutrinos are actually their own anti-particles, then they would be classified as Majorana fermions χ . This would allow for the neutrino masses to be generated by so-called Majorana mass terms; basic form in Lagrangian: $m_L \bar{\chi}_L^c \chi_L$. However, there are also considerations claiming that leptons carry a quantum number L , which represents the lepton number. This lepton number L is assumed to be conserved in particle interactions, with neutrinos ν_α carrying $L = +1$ and antineutrinos $\bar{\nu}_\alpha$ $L = -1$. Hence, mass generation using Majorana mass terms would no longer be possible as particles and anti-particles are distinctly different. In this case, the left-handed neutrinos ν_L and right-handed antineutrinos $\bar{\nu}_R$ need to be complemented by right-handed neutrinos ν_R and left-handed antineutrinos $\bar{\nu}_L$. This scenario applies to Dirac fermions, which generate the mass by the interaction of left- and right-handed particles; basic form in Lagrangian: $m_D \bar{\nu}_L \nu_R$.

⁴There are some experiments, such as LSND [102], see also overview in Ref. [101], which hint at the possible existence of sterile neutrinos, and/or some additional heavy mass eigenstates. However, we will not discuss these more general concepts in the context of this work.

Parameter	best fit	mixing angle	derived value
$\sin^2 \theta_{12}$	$0.307^{+0.018}_{-0.016}$	θ_{12}	0.587
$\sin^2 \theta_{23}$	$0.386^{+0.024}_{-0.021}$	θ_{23}	0.670
$\sin^2 \theta_{13}$	$0.0241^{+0.0025}_{-0.0025}$	θ_{13}	0.156
δ_{CP}	1.08π		

Table 1.2.: The first two columns represent the best fit values with 1σ errors for the three-flavor neutrino oscillation parameters, taken from Ref. [106]. These results are derived from global data including solar, atmospheric, reactor (including Daya Bay, Double Chooz, and RENO) and accelerator (*e.g.* T2K and MINOS) experiments, according to Ref. [106]. The last two columns, however, are the values for the mixing angles we use in our work. These values are derived from the best fit values in the second column. As it was discussed in Ref. [107], the uncertainties of these mixing parameters have a relatively small effect on the neutrino flux predictions (from GRB). For comparison reasons, see how the uncertainty bounds in Fig. 1.4 have decreased from the beginning of this work (left plot) to the end of this work (right plot).

In the work presented here, we will treat the neutrinos as Dirac fermions with three flavor and three mass eigenstates, neglecting any additional sterile states. This choice of neutrino nature gives rise to the following neutrino mixing matrix $U_{\alpha j}$, which is commonly called Pontecorvo-Maki-Nakagawa-Sakata (PMNS) matrix U_{PMNS} :

$$U_{\text{PMNS}} = \begin{pmatrix} c_{12}c_{13} & s_{12}c_{13} & s_{13}e^{-i\delta_{\text{CP}}} \\ -s_{12}c_{23} - c_{12}s_{23}s_{13}e^{-i\delta_{\text{CP}}} & c_{12}c_{23} - s_{12}s_{23}s_{13}e^{-i\delta_{\text{CP}}} & s_{23}c_{13} \\ s_{12}s_{23} - c_{12}c_{23}s_{13}e^{-i\delta_{\text{CP}}} & -c_{12}s_{23} - s_{12}c_{23}s_{13}e^{-i\delta_{\text{CP}}} & c_{23}c_{13} \end{pmatrix} . \quad (1.12)$$

In this representation of the matrix, the rows stand for the flavors e , μ , and τ , while the columns do so for the mass eigenstates 1, 2, and 3, taken from Ref. [101] (without Majorana phases). Moreover, the mixing matrix shown above uses the short hand notation $c_{ij} = \cos(\theta_{ij})$ and $s_{ij} = \sin(\theta_{ij})$ with θ_{ij} being the neutrino mixing angle among mass eigenstates $i, j = 1, 2, 3$. The Dirac CP-violating phase is denoted as δ_{CP} . Since recent measurements by Daya Bay [103], Double Chooz [104, 105], and RENO [104] have ruled out the possibility of $\theta_{13} = 0$, δ_{CP} now also needs to be considered when discussing the current mixing parameters. If not noted otherwise, the current mixing angles for normal hierarchy, as derived in Ref. [106], are used. The best fit values are given in Table 1.2 with 1σ errors, as in Ref. [106], together with the actual values for the parameters used in our calculations.

When considering the evolution of a flavor state in time, we can factorize a phase based on the energy $E_j = \sqrt{\vec{p}^2 c^2 + m_j^2}$, giving

$$|\nu_\alpha(t)\rangle = \sum_j e^{-iE_\alpha t} U_{\alpha j}^* |\nu_j\rangle . \quad (1.13)$$

Since the energies E_j are different for unequal masses m_j (assuming that \vec{p} is the same for all mass eigenstates), the superposition of the different mass eigenstates changes with time. When we calculate the probability to observe a neutrino of flavor β after a time t from a neutrino which was initially of flavor α from the absolute

square of the amplitude, $P_{\alpha\beta} = |\langle \nu_\beta | \nu_\alpha(t) \rangle|^2$, we obtain an oscillation term from the time evolution. As neutrinos are for all our purposes ultra-relativistic particles, we can approximate $E_j \approx |\vec{p}|c + m_j^2/(2|\vec{p}|c)$, and derive an oscillation length

$$L_{\alpha\beta} \equiv \frac{4\pi E c}{\Delta m_{\alpha\beta}^2} \quad , \quad (1.14)$$

when using the energy $E = |\vec{p}|c$ and changing the variable to the length $x = ct$. $\Delta m_{\alpha\beta}^2$ is the difference of the mass squares as given in Eq. (1.11). The important aspect of this oscillation length is that depending on the neutrino energy and the length traveled, the probability to detect a certain neutrino flavor changes. These are the so-called flavor oscillations. In case of cosmological sources, the neutrino flavor oscillations simplify to an averaged neutrino mixing since distances are long enough ($x \gg L_{\alpha\beta}$) for decoherence to take effect (and prevent further oscillations). Hence, the probability for a neutrino of flavor α being detected as a neutrino of flavor β is given by

$$P_{\alpha\beta} = \sum_{j=1}^3 |U_{\alpha j}|^2 |U_{\beta j}|^2 \quad , \quad (1.15)$$

taken from Ref. [108]. As long as three flavor states and three stable mass eigenstates are assumed, the $U_{\alpha j}$ are just the entries of U_{PMNS} from Eq. (1.12). Using these mixing probabilities $P_{\alpha\beta}$, one can easily calculate the expected flux ϕ in flavor α based on the predicted fluxes without mixing,

$$\phi_{\nu_\alpha} = \sum_{\beta=e,\mu,\tau} P_{\alpha\beta} \phi_{\nu_\beta} \quad . \quad (1.16)$$

Note that the fluxes ϕ_{ν_β} are subject to other propagation effects such as adiabatic losses, which are discussed in Appendix B.

1.2.2. Detection methods for astrophysical neutrinos

Once the neutrinos reach Earth there is still the issue of the detection. While during propagation through space the small interaction cross-section of neutrinos is a valuable advantage, it is a hindrance when it comes to the detection of neutrinos. The possible number of processes used for the detection is small, limited by the nature of the weak interactions. The currently used methods utilize the detection of secondary leptons through characteristic photons of annihilation processes (low energy range), via the detection of Cherenkov radiation (high-energy range), or from the material response to the passing lepton (Askaryan effect; very high energies). The first positive neutrino detection was achieved using a β -capture (or inverse β -decay) set-up to detect low energy (reactor) neutrinos, see Ref. [90],

$$\bar{\nu}_e + p^+ \rightarrow e^+ + n \quad . \quad (1.17)$$

The experimental verification was based on the coincidental detection of a flash from a e^+e^- -pair annihilation together with a signal from a slow neutron. At higher

energies, as expected for astrophysical neutrinos, this method of coincident detection is no longer sufficient and other means needed to be introduced.

As stated before, the high-energy neutrinos are nowadays mostly detected through the Cherenkov radiation of the secondary leptons. Note, that the definition of “high-energy” for astrophysical neutrinos is $E_\nu \geq 100$ MeV, according to Ref. [109]. At these energies, the secondary particles are still highly relativistic and can be detected by various event topologies. In case of charged current (CC) interactions, the associated products of the neutrino collision with a nucleus are the appropriate charged leptons, *e.g.* a muon μ^- for a ν_μ . When these secondary particles are still highly relativistic while they travel through the medium and their velocity exceeds the speed of light inside the material, they induce a characteristic blueish radiation in the material by polarization (and subsequent relaxation) of the atoms along the path of the particles (Cherenkov radiation). This radiation can be detected inside the medium itself with optical modules, if the medium is transparent in the optical band. An example for optical modules in general are the Digital Optical Modules used in IceCube, which consist of a photomultiplier tube and a single board data acquisition computer (for digitizing the data). Instrumenting a large volume of $\mathcal{O}(1 \text{ km}^3)$ and more is currently one of the main limiting factors for the sensitivity of current experiments, as already pointed out in Ref. [109]. Depending on the lifetime of the secondary particle and the further interactions with the medium, different event topologies are obtained. Here, the aforementioned muons present a special case as they live long enough (compared to taus) and do not lose energy too rapidly (compared to electrons). Hence, the path of the muons through the (optically transparent) medium can be reconstructed as a track with adequate instrumentation. These tracks have the major advantage that one can obtain additional directional information on the incident neutrino. Even though the nature of particle interactions always introduces a certain irreducible uncertainty on the reconstruction of the neutrinos, current neutrino telescopes have now reached accuracies of about 1° . The IceCube collaboration can reconstruct tracks with an angular resolution better than 0.2° (for the 40- and 59-string configurations of IceCube), taken from Ref. [110], while the ANTARES collaboration is down to 0.5° for reconstructions in the Mediterranean Sea, see Ref. [111]. These accuracies are nowhere near the ones obtained with measurements in optical or radio astronomy, especially radio interferometry, but can already give a valuable indication of the direction. This directional information most of the time comes at the expense of an accurate energy reconstruction of the muon, since the muon tracks are rarely fully contained in the detector. Moreover, fluctuations in the radiation processes additionally lead an uncertainty on the correlation of observed photons and lost muon energy. The muon energy reconstruction is therefore always only a lower estimate. On the other hand, electrons and taus are mainly detectable through particle showers, when produced through CC interactions. Electrons quickly lose their energy in the formation in an electromagnetic shower, which induces a nearly spherical glow of Cherenkov radiation. When these shower events are fully contained inside the detector, they allow for much better energy reconstruction than muon tracks. However, directional information on the incident neutrino is much harder to obtain. For tau leptons, hadronic showers accompany their production in CC interactions as well as their decay into a muon.

The main difference between hadronic and electromagnetic showers is the presence of further particles, such as muons and different kinds of mesons, in hadronic showers while electromagnetic showers are only made out of electrons/positrons and photons. Depending on the decay length of the tau, it is now possible to detect either one or two showers, with the decay path length of taus given by $\Gamma c\tau_\tau \sim 50(E_\tau/\text{PeV})\text{ m}$, with τ_τ the lifetime of the tau, taken from Ref. [112]. For energies below a few PeV, the decay length of the tau is so short that the tau track cannot be distinguished from the hadronic shower, and only the track of the muon (from the tau decay) can be detected apart from the shower. This topology is called a lollipop event. For even higher tau energies, the two showers can be distinguished and are connected by a tau track, giving rise to a so-called double-bang event, see Ref. [112] for a discussion. Even though cascades do have the advantage of the better energy resolution for events which are fully contained in the detector, they actually have several drawbacks apart from the worse directional information. Since the cascades need to be close⁵ to or at least partially inside the actually instrumented volume, the effective volume for cascades is much smaller than for muon tracks. Additionally, it is currently only partially possible to distinguish hadronic from electromagnetic showers. Due to this, most of the analyses do not separate electromagnetic from hadronic showers, but only report the sum of all shower events, *e.g.* Refs. [12, 13]. Moreover, cascades have the problem that they have the additional background from neutral current (NC) interactions of all flavors producing hadronic showers. Hence, shower events are affected by a contamination from NC interactions. On the other hand, neutrino induced showers can (in theory) be also detected as nearly horizontal (or up-going) extensive air showers (EAS) inside the atmosphere for neutrino energies above EeV. These EAS can be measured by cosmic ray detectors, such as the *Pierre Auger Observatory*, or by monitoring the dark night sky for nitrogen fluorescence with pixelated optical detectors, as done by the Fly’s Eye group, see discussion in Ref. [109]. As a rule of thumb, it is expected that it is more likely to detect a track event than a shower event. For the next generation of telescopes, the Askaryan effect is being considered as a viable alternative to allow for even larger effective volumes, as this effect allows for detection in the radio window (below 100 MHz) or via acoustic waves. The Askaryan effect itself is similar to the Cherenkov effect, as it is described to be due to the polarization/energy deposition of the secondary particles. However, the response of the material is at much lower frequencies. Different experiments, such as ANITA [113, 114], RICE [115, 116], or the up-coming ARA [117], facilitate this effect to detect high-energy neutrinos.

Nonetheless, the two different event topologies allow for additional observables, which should fulfill the following two requirements, according to Ref. [118]:

1. They take into account the unknown flux normalization.
2. They take into account the detector properties.

A simple solution to fulfill the first requirement are so-called flavor ratios. Flavor ratios are ratios of the measured neutrino fluxes of different flavors. Since shower

⁵As a rough estimate for a shower, we can assume a sphere with a $\sim 100\text{ m}$ radius for a TeV parent particle.

events represent $\nu_e + \nu_\tau$ and (muon) tracks ν_μ (neglecting backgrounds), it is possible to interpret the ratio of shower events to tracks as the flavor ratio

$$\hat{R} = \frac{\phi_{\bar{\nu}_\mu + \nu_\mu}}{\phi_{\bar{\nu}_e + \nu_e} + \phi_{\bar{\nu}_\tau + \nu_\tau}} \quad , \quad (1.18)$$

with ϕ being the summed neutrino and antineutrino flux at the detector, taken from Ref. [119].⁶ This definition has the advantage that it is independent of the unknown flux normalization, as it cancels in the ratio. An example for the predicted flavor ratio for neutrino emission from a GRB can be seen in Fig. 1.4. As stated before, it is currently difficult to distinguish electromagnetic and hadronic showers in neutrino telescopes. Therefore it is better to treat ν_e and ν_τ equally. Nonetheless, the interpretation of these flavor ratios also needs to be done with great care as they are somewhat idealized quantities. In case of the showers, the backgrounds from NC-induced shower events need to be taken into account, while the muon tracks can also be induced by atmospheric muons or atmospheric neutrinos as well as a possible misidentification of tau events. Another problem is the different statistics of track and shower events — even though the statistics of UHE neutrino events are currently still very low in general. Still, flavor ratios can be a useful tool for the search for new physics effects, see Ref. [121] for a review.

⁶There has been a recent publication that suggests a slight redefinition of the flavor ratio \hat{R} , which would be better suited for the highest energies according to the authors of Ref. [120]. Still, for now the separation into tracks and showers is the best we can do.

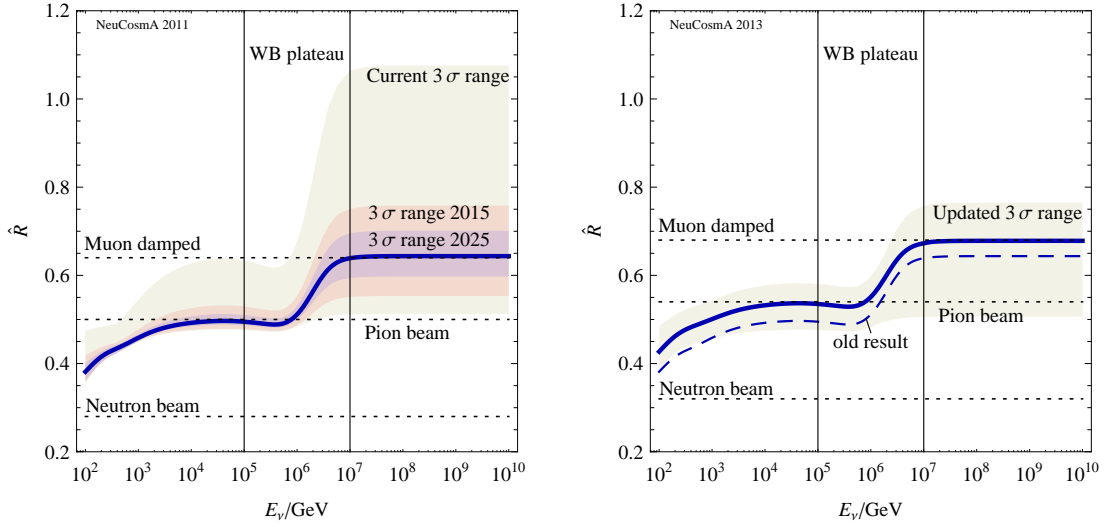


Figure 1.4.: As an example for the flavor ratio \hat{R} from Eq. (1.18), we show the predicted flavor ratio at the observer for a numerical reproduction of the Waxman-Bahcall (WB) GRB neutrino spectrum; details on calculation can be taken from chapter 2. The left plot is taken from Ref. [107] and depicts the result after neutrino mixing on basis of data from 2010, including $\theta_{13} = 0$. The thick blue solid curve depicts the result for the best-fit values, while the shaded regions depict the 2010 (“current”) as well as two predicted uncertainties, see labels in plot. The right plot is an updated version of the previous plot, using the values from Table 1.2. Since $\theta_{13} > 0$ is now experimentally verified, we have an additional parameter in flavor mixing with the CP-phase δ_{CP} . The additional parameter as well as fewer years of data lead to the uncertainty in the right plot being not yet as low as the prediction for 2015, shown in the left plot. However, during the progress of this work, the uncertainty on the flavor ratio has already been greatly reduced; compare the “current” (left plot) and the “updated” uncertainty (right plot). Due to the update of the mixing parameters, all curves, including the reference sources, have been shifted up by about a factor of 0.04.

2. Neutrino flux predictions based on GRB data

In case of GRBs, the photohadronic interactions are considered to be the main production mechanism of neutrinos. The Δ -resonance approximation proposed by Waxman and Bahcall (WB) [122, 123] is normally used to calculate the production of neutrinos in GRBs, with the decay of the charged pions giving rise to the neutrinos, see Eq. (1.2). For this reason, we will first review the original GRB flux model as proposed by Waxman and Bahcall. We will then discuss how this model was extended for an application to real burst-by-burst analyses. As a third step, we will show how our detailed treatment of the particle physics involved (as well as corrections to the analytical formulas) change the neutrino flux prediction. Then, in a fourth section, we will discuss how statistics and unknown parameters introduce an additional uncertainty on the neutrino flux predictions. In a final section, we will introduce an application of our approach to actual data at the example of the current ANTARES GRB analysis.

2.1. The Waxman-Bahcall approach for neutrino spectra from GRBs

As mentioned before, the calculation of the GRB neutrino flux as proposed by Waxman and Bahcall [122, 123] is a simple estimation of the (muon) neutrino flux based on general GRB properties. The key ingredients for the calculation are the knowledge of the proton and the photon spectra as well as that the Δ -resonance is the dominant contribution to the photohadronic interaction cross section. Based on the two flux shapes and the kinematics of resonant interactions, it is possible to predict the flux shape of the neutrino spectrum. The resulting flux prediction can be seen as a thin black dashed curve in Fig. 2.2. In general, the proton spectrum is considered to be a steady target spectrum in the rest frame of the source, and can be written as in Ref. [124] as

$$N'_p(E') = C'_p \cdot \begin{cases} E'^{-\alpha_p} \cdot \exp\left(-\frac{E'^2}{E'_{p,\max}{}^2}\right) & \varepsilon'_{p,\min} \leq E' \\ 0 & \text{else} \end{cases} \quad (2.1)$$

with the cutoff energy $E'_{p,\max}$ being derived by balancing acceleration gains and dominant losses, see Eq. (2.31) later this section. The low energy cutoff $\varepsilon'_{p,\min}$ (in the shock rest frame) is normally set to 1 GeV ($\approx m_p c^2$). The actual value of the minimal energy of the proton spectrum is still a point of discussion in the literature,

but assuming that the protons have at least $\Gamma m_p c^2$ after boosting can be considered a conservative estimate. The factor C'_p is the normalization of the proton spectrum, which will be kept free for the moment. According to Ref. [125], the shape of the proton spectrum is derived from the observed cosmic ray spectrum in the energy range between 10^{10} and 10^{12} GeV. This power-law shape is typical for non-thermal spectra, which are associated with shock acceleration. For simplicity reasons, it is normally assumed that the proton spectral index $\alpha_p \simeq 2$. However, it should be noted that plasma physics calculations indicate that shock acceleration should actually lead to $\alpha_p \simeq 2.2 - 2.3$, see discussion in Ref. [126]. The target photon spectrum $N'_\gamma(\varepsilon')$ is obtained from GRB observations. The photon spectra in the calculations by Waxman and Bahcall are considered to be broken power-laws or parameterized by the Band function¹, see Ref. [80]:

$$N'_\gamma(\varepsilon') = C'_\gamma \cdot \begin{cases} (\varepsilon'/\varepsilon'_{\gamma,\text{break}})^{-\alpha_\gamma} & \varepsilon'_{\gamma,\text{min}} \leq \varepsilon' < \varepsilon'_{\gamma,\text{break}} \\ (\varepsilon'/\varepsilon'_{\gamma,\text{break}})^{-\beta_\gamma} & \varepsilon'_{\gamma,\text{break}} \leq \varepsilon' < \varepsilon'_{\gamma,\text{max}} \\ 0 & \text{else} \end{cases} . \quad (2.2)$$

As for the proton spectrum, the factor C'_γ represents the (so far free) normalization of the photon spectrum. Unnormalized, the spectrum is fixed to 1 at the break energy $\varepsilon'_{\gamma,\text{break}}$. Below this break, the photon spectrum has the index α_γ and above it follows the index β_γ . Waxman and Bahcall assume that the standard values for these are $\alpha_\gamma \simeq 1$ and $\beta_\gamma \simeq 2$. Additionally, the parameterization given in Eq. (2.2) already includes (arbitrary) high- and low-energy cutoffs, $\varepsilon'_{\gamma,\text{max}}$ and $\varepsilon'_{\gamma,\text{min}}$. The reason for these is two-fold: On the one hand, there is so far no experimental evidence that the photon spectra extend to arbitrarily high or low energies, so the cutoffs actually have physical reason. On the other hand, we will later need them for the numerical calculations, since numerical calculations are always only discrete approximations of continuous problems. For the general discussion done by Waxman and Bahcall, these factors are, however, not needed.

What is actually needed for the calculation from Ref. [122] is the kinematic treatment of the Δ -resonance. Based on the fixed requirement to the center-of-mass energy for the production of a $\Delta(1232)$ -resonance, it is possible to calculate the needed proton and photon energies using the formula

$$E'_\gamma E'_p \geq \frac{m_\Delta^2 - m_p^2}{2(1 - \cos \theta'_{p\gamma})} . \quad (2.3)$$

As can be expected from the name $\Delta(1232)$ -resonance, the mass of the resonance is $m_\Delta \simeq 1232$ MeV [101]. Accordingly, $m_p \simeq 938$ MeV is the mass of the proton, while $\theta'_{p\gamma}$ is the angle between the proton and photon momenta in the center-of-mass frame. Based now on the break in the photon spectrum $\varepsilon'_{\gamma,\text{break}}$, it is possible to calculate at which energy the neutrino spectrum would also have a break. This is considered to be the first break of the neutrino spectrum, ε_ν^b . Moreover, the fixed energy of a resonant

¹Note that the original Band function has an additional exponentially decaying component above the photon break. We neglect this feature only for the sake of a better recalculation of the WB flux shape. This is not needed for a calculation to be successful, but purely cosmetic.

interaction also leads to the connection of the low-energy photons to the high-energy protons, and vice versa. Additionally, Waxman and Bahcall reason that the charged pions would also be subject to synchrotron losses, due to the magnetic fields present inside the GRB. Since the magnetic fields are needed for the acceleration, this effect is also always present. Hence, it is possible that the pions actually lose energy before they decay. This leads to a further break in the expected neutrino spectrum, ε_ν^s . Based on these considerations, Waxman and Bahcall derive a power-law spectrum with two breaks for the neutrinos, see Ref. [123] for a depiction. The assumed values for the breaks are given in the literature as $\varepsilon_\nu^b \approx 10^5$ GeV and $\varepsilon_\nu^s \approx 10^7$ GeV, see Ref. [73, 122]. We will discuss the calculation of both break energies in more detail in Sec. 2.3. For now, we only want to mention that the analytical parameterization of this spectrum (in the observer's frame) is given in Ref [73] to be

$$E_\nu^2 \frac{dN_\nu}{dE_\nu} = C_\nu \cdot \begin{cases} (E_\nu/\varepsilon_\nu^b)^{-\alpha_\nu} & \text{for } E_\nu < \varepsilon_\nu^b \\ (E_\nu/\varepsilon_\nu^b)^{-\beta_\nu} & \text{for } \varepsilon_\nu^b \leq E_\nu < \varepsilon_\nu^s \\ (E_\nu/\varepsilon_\nu^b)^{-\beta_\nu} (E_\nu/\varepsilon_\nu^s)^{-2} & \text{for } E_\nu \geq \varepsilon_\nu^s \end{cases} . \quad (2.4)$$

In this representation, dN_ν/dE_ν is the observed neutrino spectrum with E_ν being the neutrino energy at the observer. The spectral indices α_ν and β_ν can be calculated based on the proton and photon spectral indices, leading to $\alpha_\nu = \alpha_p - \beta_\gamma - 1 \approx -1$ and $\beta_\nu = \alpha_p - \alpha_\gamma - 1 \approx 0$, see *e.g.* Ref. [73]. Moreover, C_ν is the normalization of the neutrino spectrum at the lower break ε_ν^b . Waxman and Bahcall estimate what the upper bound on C_ν would be for neutrinos from GRB [123]. For this, they assumed that GRBs are the only source of UHECR in the range of 10^{10} to 10^{12} GeV. By using the observational data and estimates about the mean free path of cosmic rays in the universe, they obtain that the total energy injection from GRB would have to be about 10^{44} erg Mpc $^{-3}$ yr $^{-1}$ [123].² If now all of these cosmic rays are made up of protons³ and the protons all interact via photohadronic interactions, then this would give the upper bound for neutrinos based on CR observations. In Ref. [123], Waxman and Bahcall actually derive two bounds: one independent of the actual source models and one for GRBs. The general model uses the age of the universe, the fraction of proton energy obtained by the neutrinos, and the cosmic source evolution as parameters. Moreover, Waxman and Bahcall include that only about half the pions produced in photohadronic interactions are charged in form of an additional factor. They also include basic flavor mixing considerations. With the (more or less known) age of the universe and two different source evolution models, they obtain $C_\nu \simeq 0.9 \cdot 10^{-8}$ GeV cm $^{-2}$ s $^{-1}$ sr $^{-1}$ ($4.5 \cdot 10^{-8}$ GeV cm $^{-2}$ s $^{-1}$ sr $^{-1}$) as the upper bound for no evolution (evolution with the star formation rate), if the neutrinos obtain all the proton energy. This is, of course, only a theoretical upper bound, which is already above current sensitivity limits of neutrino telescopes. A more realistic bound is the one for GRBs as it uses particle physics considerations on the fraction of energy obtained by the neutrinos. Based on the π^+ production

²We will revisit the calculation of this bound again in Sec. 4.2, when we discuss the CR propagation code.

³Note that the composition of UHECR is still unclear. There are experimental hints for a ‘‘heavier’’ composition (with nuclei as CRs), see, *e.g.*, Ref. [127], as well as theoretical arguments, such as photodisintegration of nuclei, see, *e.g.*, Refs. [128, 129], that UHECR need to be protons.

and decay via the Δ -resonance, they estimate that the neutrinos would obtain about 1/20 of the initial proton energy, with the π^+ getting about 0.2 of the initial proton energy and the ν_μ getting about 1/4 of the energy of the intermediate π^+ . With this the upper bound of $C_\nu \approx 3 \cdot 10^{-9} \text{ GeV cm}^{-2} \text{ s}^{-1} \text{ sr}^{-1}$ is obtained, see Ref. [123]. A slightly different method to normalize the predicted neutrino spectra is proposed by Mannheim, Protheroe, and Rachen (MPR) in Ref. [130]. As done by Waxman and Bahcall, the authors of Ref. [130] derived source independent as well as source dependent bounds on the neutrino flux. One important difference is that they tried to make the calculation as self-consistent as possible with regards to gamma-ray and CR data by directly incorporating precomputed results from SOPHIA [131, 132].⁴ MPR also only discuss the escape of neutrons from the source, while protons are considered to be confined. Moreover, the observed CR spectrum is assumed to be the result of a large number of sources. The assumed trial spectra for the protons are $\propto E^{-1}$, as opposed to E^{-2} for the WB bound. Their main criticism towards WB is that the WB calculation is only valid for optically thin to neutron escape sources and only uses cosmic rays above 10^{10} GeV . They themselves claim that the extragalactic component of CRs starts at $3 \cdot 10^6 \text{ GeV}$ and that there is no GZK cutoff. This leads to two significant changes, as the authors themselves admit: On the one hand, the CRs with energies below 10^{10} GeV lead to an increase of the predicted neutrinos below 10^7 GeV . On the other hand, the increase of the neutrino prediction above 10^9 GeV is due to the CR spectrum extending unperturbed even though the CRs interact with the CMB (no cutoff). Hence, more CRs need to be injected which also leads to more neutrinos. As it was shown by recent CR data, this latter part is not true, since the GZK-cutoff has been observed, see discussion in Ref. [5]. The former part about what CR energies need to be considered is an open issue, even though the range above 10^{10} GeV seems a bit more conservative. Still, the WB bound and the MPR bound agree at an energy of about 10^9 GeV , which is also the point of the lowest neutrino flux prediction in the MPR case. Hence, both of these generic models are already ruled out from neutrino observations, even though the basic concept is still applicable. Moreover, the idea of applying the neutrino bounds to specific source models, to AGN in case of MPR [130] or to GRB for WB [123], is currently the most promising approach for theoretical neutrino bounds.

2.2. The Guetta et al. model and its extensions

Historically, the next step was the transition from normalizing over the whole (assumed) population of GRB via the UHECR observations to a calculation of the neutrino spectra on a burst-by-burst basis. For this, it is essential that something else than the cosmic rays is used for the normalization. Hence, under consideration of the energy equipartition arguments, which are based on afterglow observations, Guetta et al. [70] proposed a normalization using the observed gamma-ray spectra. One important aspect is also that the calculations presented in Ref. [70] already

⁴This is a subtle difference to our approach: We compute the photohadronic interactions during the calculation, while MPR used precalculated photohadronic results on the (energy) relations to draw their conclusions.

include the boosting from the observer's frame to the SRF and back. Moreover, the calculations also (partially) include the losses due to the expansion of the universe. Consequently, the observed first neutrino break energy, based on the observed photon energy, can be calculated with the phenomenological formula given in Ref. [70]:

$$\varepsilon_\nu^b = 7 \cdot 10^5 \frac{\Gamma_{2.5}^2}{(1+z)^2 \varepsilon_{\gamma,\text{break,MeV}}} \text{ GeV} \quad . \quad (2.5)$$

The notation used for this formula includes that the parameters are expressed in units of their standard value; $\Gamma = 10^{2.5} \Gamma_{2.5}$, $\varepsilon_{\gamma,\text{break}} = 1 \text{ MeV } \varepsilon_{\gamma,\text{break,MeV}}$. Note again, the primed quantities are considered to be in the SRF while unprimed quantities are considered to be in the observer's frame. Moreover, it is detailed in Ref. [70] how the synchrotron loss rate as well as the pion decay rate can be calculated based on the observed parameters, such as the luminosity $L_{\gamma,\text{iso}}$, the Lorentz factor Γ , or the variability time t_v . The resulting formula for the second break due to the pion synchrotron losses as given in Ref. [70] is

$$\varepsilon_\nu^s = \frac{10^8}{1+z} \epsilon_e^{1/2} \epsilon_B^{-1/2} L_{\gamma,\text{iso},52}^{-1/2} \Gamma_{2.5}^4 t_{v,-2} \text{ GeV} \quad . \quad (2.6)$$

Here, ϵ_e is the fraction of the total energy in electrons/photons and ϵ_B the corresponding fraction of energy stored in the magnetic field. The other quantities are again given in units of the standard value; $L_{\gamma,\text{iso}} = 10^{52} \text{ erg } L_{\gamma,\text{iso},52}$, $t_v = 10^{-2} \text{ s } t_{v,-2}$. Also, it can be inferred that there should be a second break one order of magnitude below the break given in Eq. (2.6) due to the different properties of the μ^+ (compared to the parent π^+). The authors also argue, how the fraction of energy a proton loses to pions f_π could be different from the average energy lost to pions per interaction, $\langle x_{p \rightarrow \pi} \rangle$, based on the possibility of multiple interactions. Hence, an energy dependent version of f_π is given in Ref. [70]. Together with an suggested approach of how to estimate the Lorentz factor Γ , it is possible calculate the normalization of the neutrino spectra based on the observed photon fluence F_γ , see Ref. [70]:

$$C_\nu \approx \frac{1}{8} \frac{1}{\epsilon_e} \frac{F_\gamma}{\ln(10)} 0.2 \frac{L_{\gamma,\text{iso},52}}{\Gamma_{2.5}^4 t_{v,-2} \varepsilon_{\gamma,\text{break,MeV}}} \quad . \quad (2.7)$$

For actual GRB neutrino searches, this formula is only slightly changed, to allow for a better integral definition of the different energies, as detailed by the IceCube collaboration in Ref. [133]. Instead of using Eq. (2.7) for the normalization, the calculation was changed to

$$\int_0^\infty dE_\nu E_\nu F_\nu(E_\nu) = \overbrace{\frac{1}{8}}^{x_{\pi \rightarrow \nu} = \frac{1}{2} \cdot \frac{1}{4}} \underbrace{\left(1 - (1 - \langle x_{p \rightarrow \pi} \rangle)^{\Delta R / \lambda_{p\gamma}}\right)}_{f_\pi} \overbrace{\frac{1}{f_e} \int_{1 \text{ keV}}^{10 \text{ MeV}} dE_\gamma E_\gamma F_\gamma(E_\gamma)}^{\text{energy in protons}} \quad . \quad (2.8)$$

The factor of $1/8$ in both equations represents the energy transferred from the pion to the neutrino. It consists of two factors: $1/2$ since only about 50% of all pions from the decay of the Δ -resonance are actually charged, and $1/4$ is again the average amount a neutrino inherits from its parent pion. The fraction of proton energy

lost due to pion production f_π has been changed in Eq. (2.8) to never be larger than 1, based on the reasoning that a proton can only lose all its energy due to photohadronic interactions.

Also, the energy in protons is now calculated by integrating over a certain energy range instead of using the (ambiguous) value of $L_{\gamma,\text{iso}}$. Guetta et al. [70] already mention that their derivation as in Eq. 2.7 suffers from the empirical derivation of the luminosity when the redshift is unknown, and additionally introduce an estimate without $L_{\gamma,\text{iso}}$. This approach without needing empirical formulas is applied to obtain the newer formula given by Eq. (2.8). Based on this model, the IceCube collaboration has published several studies in the last few years, which should have already given a signal according to the approach described above, see Refs. [134, 135]. Especially, it was stated in Ref. [135] that GRBs were excluded from being the sources of UHECR based on neutrino observations. However, as we show in Ref. [136] and as has been independently confirmed by other groups, see Refs. [137, 138], the analytical calculation described in this section still has several inaccuracies. These inaccuracies lead to an overestimation of the neutrino flux prediction. In the next section, we will detail how the calculation of the neutrino flux is correctly done in a self-consistent way for the internal shock model of GRB fireballs.

2.3. The NeuCosmA model

In this section, we want to detail how the neutrino spectra from a GRB are correctly calculated based on the particle physics involved. We will first take a closer look at the particle physics involved, and reason why numerical calculations are needed. We will also review the process of normalizing the different spectra, and point out how the calculation can be done in a self-consistent way for GRB fireballs in the internal shock model.

Even though the Δ -resonance, see Eq. (1.2), is the leading contribution to the photohadronic interaction cross-section, accelerator experiments on deep inelastic scattering have shown that the full photohadronic interaction cross-section consists of more than the $\Delta(1232)$ -resonance, see Ref. [101] and references therein. As can be seen from Fig. 2.1, taken from Ref. [139], there are several additional contributions to the full cross-section, such as direct production of pions (t -channel processes), higher resonances, and high-energy processes leading to the production of several pions. Especially these high-energy processes lead to a near constant interaction cross-section at higher energies. Additionally, these high-energy processes lead to π^- , even in the case for $p\gamma$ interactions (and vice versa to π^+ in case of $n\gamma$).⁵ The energies achieved in the interactions can be so high that also kaons can be produced, with K^+ being considered to be the dominant mode, see discussion in Ref. [140]. Moreover, one should not forget that free neutrons are actually unstable and decay,

⁵It needs to be considered that neutrons can also interact with photons, leading to the production of π^- . Due to isospin symmetry, the interaction cross-section for $n\gamma$ is the same as for $p\gamma$. This is especially important for systems with a high photohadronic interaction rate, as half the protons go to neutrons, which can interact again.

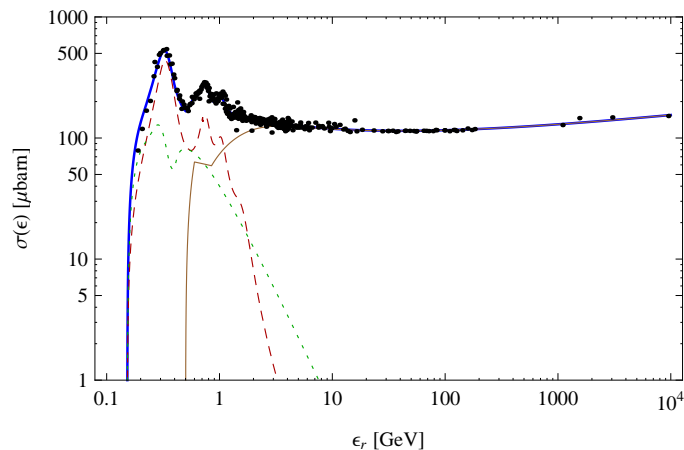


Figure 2.1.: The total photohadronic interaction cross section $\sigma_{p\gamma}$ (blue solid curve; $1 \mu\text{barn} = 10^{-30} \text{cm}^2$) as a function of photon energy in the proton rest frame ϵ_r , taken from Ref. [139]. The dots represent experimental data, as can be found in Ref. [101] (or earlier versions). Additionally, the contributions from baryon resonances (red dashed curve), direct pion production (t -channel; green dotted curve), and high-energy processes leading to multi-pion production (brown solid curve) are shown separately. The highest peak (at $\epsilon_r \approx 0.3 \text{ GeV}$) is the Δ -resonance. However, the non-vanishing cross section at values far above the Δ -resonance energy shows that a treatment using only the dominant resonance is not sufficient.

even though their lifetime (at rest) is comparably long with $\tau_n = (880.1 \pm 1.1) \text{ s}$, see Ref. [101].⁶ We consider the following decays leading to neutrinos:

$$\begin{aligned} \pi^+ &\rightarrow \mu^+ + \nu_\mu, \\ \mu^+ &\rightarrow e^+ + \nu_e + \bar{\nu}_\mu, \end{aligned} \quad (2.9)$$

$$\begin{aligned} \pi^- &\rightarrow \mu^- + \bar{\nu}_\mu, \\ \mu^- &\rightarrow e^- + \bar{\nu}_e + \nu_\mu, \end{aligned} \quad (2.10)$$

$$K^+ \rightarrow \mu^+ + \nu_\mu, \quad (2.11)$$

$$n \rightarrow p + e^- + \bar{\nu}_e, \quad (2.12)$$

$$\pi^0 \rightarrow \gamma + \gamma. \quad (2.13)$$

When we want to compute the result for actual particle spectra, the interactions of protons and photons need to be simulated or at least approximated. One possibility is the already mentioned Δ -resonance approximation of Waxman and Bahcall. This allows for an analytical, and therefore fast, calculation of the resulting spectra. As we recapped in Sec. 2.1, it is even possible to predict the flux shape by general considerations, see Eq. (2.4). Apart from the fixed energy of the Δ -resonance, an additional assumption is the usage of only head-on collisions, *i.e.* assuming that $\theta'_{p\gamma} = \pi$ in Eq. (2.3). Another possibility is to use a numerical code for the calculation of the photohadronic interactions. The currently most commonly used code is the

⁶For the calculations presented in this work, we are still using the old value of $\tau_n = (885.7 \pm 0.8) \text{ s}$ [141], since the change presented by the Particle Data Group in July 2012 is less than 1%, which is negligible for current astrophysical standards.

Monte-Carlo algorithm SOPHIA, see Ref. [131]. It is able to simulate the interactions of the particles using the full interaction cross-section as well as correctly reproducing the angular distributions of collisions at arbitrary collision angle $\theta'_{p\gamma}$. Even though the SOPHIA algorithm yields far more detailed results than the basic analytical approach — for a predefined set of types of input photon spectra — it has two major disadvantages. First of all SOPHIA is a Monte-Carlo-algorithm, which means that the outcome is probabilistic, and a larger number of runs is needed to get an idea of a common result. And secondly, intermediate particles are integrated out by SOPHIA, and losses of secondary particles are not treated individually. In recent years, in an attempt to combine the advantages of the analytical (WB) and the numerical (SOPHIA) approaches, a third option has been developed in form of semi-analytical numerical calculations. One example for this new approach is the NeuCosmA-code, see Refs. [107, 142] for a basic description, which incorporates the model Sim-B of Ref. [139] for the interaction cross-section. Said model is based on a novel approach, which combines the factorization of the interaction cross-section into different interaction types (see, *e.g.*, Refs. [143, 144]) with an analytical approach similar to the one used in Ref. [145], to reproduce the numerical results of SOPHIA for power-law and black body spectra, see Ref. [139].⁷ It is, however, extended in the aspect of treating the intermediate particles individually, which allows for the calculation of energy losses of the secondary particles, see Ref. [142]. Moreover, effects such as flavor mixing of the neutrinos or the helicity dependent decay of muons (based on Ref. [124]) are directly treated by the code. The main idea of the code is effectively solve the interaction rate formula, take from Ref. [139],

$$t'^{-1}_{p\gamma}(E'_p) = \int d\varepsilon'_\gamma \int_{-1}^{+1} \frac{d \cos \theta_{p\gamma}}{2} (1 - \cos \theta_{p\gamma}) n'_\gamma(\varepsilon'_\gamma, \cos \theta_{p\gamma}) \sigma_{p\gamma}(\varepsilon_r) \quad . \quad (2.14)$$

Here, $n'_\gamma(\varepsilon'_\gamma, \cos \theta_{p\gamma})$ is the density of target photons as a function of the photon energy ε'_γ , while $\sigma_{p\gamma}(\varepsilon_r)$ is the photohadronic interaction cross-section as a function of the photon energy in the nucleon/parent rest frame, given by $\varepsilon_r = E'_p \varepsilon'_\gamma / m_p (1 - \cos \theta_{p\gamma})$. By employing several simplifications, it is possible to efficiently calculate the interaction rate using this equation. The most important simplification is the parameterization of the interaction cross-section into the different interaction channels, with the full rate given by the sum over several partial rates; see Ref. [139] for details. In Fig. 2.2, we depict how different parts of the full interaction cross-section contribute to the neutrino flux prediction. In said plot, the contributions are grouped into the $\Delta(1232)$ -resonance, higher resonances, direct production of pions (t -channel processes), and the contribution from high-energy processes leading to multiple pions, see labels in plot. Compared to the analytical flux prediction by Waxman and Bahcall from Eq. (2.4) (thin dashed curve), especially the high-energy processes lead to a change in the flux shape, *i.e.* a rising slope instead of a plateau between the first and the second break. Moreover, we have included the result for the numerical calculation based on the parameters of the Δ -resonance specified by Waxman and Bahcall in Ref. [122] (thick dashed curve). As this curve shows, this parameterization is actually already equivalent to the

⁷The decay of the π^0 into two photons is similar to Ref. [146].

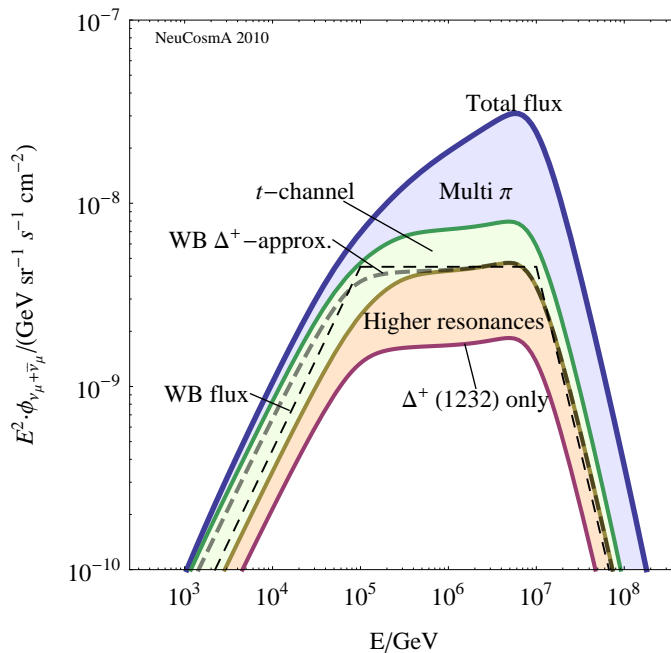


Figure 2.2.: The contributions of the full photohadronic interaction cross-section to the neutrino flux from π^\pm -decay as function of neutrino energy. The contributions are divided into the $\Delta(1232)$ -resonance, higher resonances, direct production of pions (t -channel processes), and the contribution from high-energy processes leading to multiple pions (see labels in plot). Additionally, the analytical WB flux shape from Eq. (2.4) (thin dashed curve) as well as the semi-analytical result (thick dashed curve) for the parameters of the WB Δ -resonance approximation, given in Ref. [122], are depicted. The figure is taken from Ref. [82].

$\Delta(1232)$ -resonance plus higher resonances, and even includes a low-energy contribution from the direct pion production. The WB Δ -resonance is therefore more than just $\Delta(1232)$, even though the analytical calculations do not consider this in their decays. The second important simplification compared to SOPHIA is that averaging is used to reduce the angular distribution to the most probable collision angle $\theta_{p\gamma}$ instead of simulating interactions with the full kinematics. This, however, implies that the calculations with NeuCosmA are done in a frame where the photon spectra are isotropic, so that the approximation $\langle\theta\rangle = \pi/2$, or $\langle\cos(\theta)\rangle = 0$, is actually valid. This should always be the case in the SRF of the GRB, as the proton as well as the photon spectrum should be isotropic in this frame. In summary, NeuCosmA represents a trade-off of accuracy and speed by using the full photohadronic interaction cross-section with a deterministic kinematics treatment. See Appendix A for a more detailed explanation.

A detailed treatment of the particle physics is, however, not done with the different contributions to the full photohadronic interaction cross-section. For a full description, also the added decay modes given in Eqs. (2.9)–(2.12) have to be included. Hence, we need to revisit the origin of the second break. It was already stated in Ref. [122] that this break is due to the synchrotron losses of the secondary particles. However, as mentioned in Ref. [70], it is not sufficient to only consider pions when calculating this break. The base logic of comparing the synchrotron loss rate $t'_{\text{syn}}{}^{-1}$ to the decay rate τ'^{-1} applies to all kinds of charged particles. Hence, we

need to calculate the critical energy, where decay and synchrotron losses balance, for each particle species individually. For this reason, we need the synchrotron loss rate (in Gaussian cgs units)

$$t'_{\text{syn}}{}^{-1}(E') = \frac{4 c q^4 B'^2 E'}{9 m^4} \quad (2.15)$$

with m being the rest mass of the charged particle (in [erg], using the relation $1 \text{ erg} = 624.15 \text{ GeV}$)⁸, E' the particle's energy (in [erg]), q the particle charge (in [Fr]⁹; for most particles this is just the elementary charge $e \simeq 4.803 \cdot 10^{-10} \text{ Fr}$) and B' the magnetic field (in [G]). The speed of light c is needed here as $c = 29\,979\,245\,800 \text{ cm s}^{-1}$. This needs to be compared to the decay rate

$$\tau'^{-1}(E') = \tau_0^{-1} \frac{m}{E'} \quad , \quad (2.16)$$

with τ_0^{-1} being the decay rate in the rest frame of the particle. The values for different particles can be taken from, *e.g.*, Ref. [101]. By assuming equality of the two rates, it is possible to obtain a critical energy ε'_c for each particle species:

$$\varepsilon'_c = \sqrt{\frac{9 m^5}{c \tau_0}} \cdot \frac{1}{2 q^2 B'} \quad . \quad (2.17)$$

This break in the spectrum of the secondary particle species directly translates into a break in the neutrino spectrum. It is, of course, not exactly at the same energy in the neutrino spectrum, since the neutrino only inherits a certain fraction of the parent particle's energy, *e.g.* about 1/4 in case of charged pions. Note that the critical energy given in Eq. (2.17) is insensitive to the sign of the charge of the particle, only the species is relevant. As we showed in Ref. [82] and can be seen in Fig. 2.3, the different parent particles in the detailed particle physics calculation lead to a splitting of the neutrino spectrum, resulting in a double peak with an additional high-energy component due to kaons. The total muon neutrino flux (solid blue curve) is the result of contributions from muon decays (thin green dashed curve), pion decays (thin yellow dotted curve), and kaon decays (thin gray dash-dotted curve). Each of these individual contributions has a similar shape to the one shown in Fig. 2.2, *i.e.* said figure shows the contribution from pion decays. However, the contributions have different critical energies based on their parent particles. The one for muons is at lower energies compared to the result for pions while the one for kaons is significantly higher, as can be easily verified by inserting the corresponding particle properties into Eq. (2.17). Moreover, the distribution for kaons is shifted to higher energies since kaons are only produced in high-energy processes while the pions and the muons are the result of the same decay chain.

Additionally, the flux shape is only marginally affected by flavor mixing. The produced electron neutrinos are mainly due the contribution from muon decays with

⁸We will use this conversion frequently throughout this work. In all plots, energies are given in [GeV], however, for the formulas these energies need to be converted to [erg].

⁹1 Fr = $1 \sqrt{\text{erg cm}}$

the component from neutron decays only dominating at low energies (not shown in plot). As a result, the muon peak in the double peak shape is slightly enhanced when flavor mixing is considered.¹⁰ While the classical WB model assumed a flavor composition ($\nu_e : \nu_\mu : \nu_\tau$) of (1 : 2 : 0) at the production site leading to (1 : 1 : 1) at the observer, NeuCosmA allows for an energy-dependent treatment of the flavor composition, in accordance with results presented by Murase and Nagataki [81], Lipari et al. [124], Kashti and Waxman [148], and others.

An example for the energy dependent flavor ratios \hat{R} (after flavor mixing) as a function of observed neutrino energy E_ν can be seen in Fig. 1.4, with the nominal prediction being depicted as a solid blue curve. Each of the two plots includes the flavor ratios for certain types of sources as dotted horizontal lines, with the definition for the sources as in Ref. [142]. The aforementioned standard case is denoted as “pion beam” (neutrinos from whole pion decay chain, as in Eq. (2.9)), while for the “muon damped” case only the muon neutrinos from the pion decays contribute since the muons lose energy through synchrotron losses before decaying. The value of the “neutron beam” is derived from the initial production of only one electron neutrino per neutron decay, see Eq. (2.12). When going down in energy, the flavor ratio starts at the level of the “muon damped” source as the contributions from muons are suppressed above about 10^6 GeV, compare to the contributions shown in left plot of Fig. 2.3. Below 10^6 GeV, the flavor ratio is consistent with the “pion beam” source. Only at the lowest energies (below 10^3 GeV) do the neutrinos from neutron decays gain importance and the flavor ratios drops towards a pure “neutron source”. The difference between the left plot and the right plot of Fig. 1.4 is the date when they were created. The left plot is from 2010, taken from Ref. [107], and still uses mixing angles from said year including $\theta_{13} = 0$. The uncertainties on the different mixing angles were still quite high at that stage, as can be seen from the large shaded area labeled “Current 3σ range”. Also, estimated uncertainties for the improving experimental precision in 2015 and 2025 (based on 2010 predictions) are included as gradually darker shaded bands.¹¹ The right plot, on the other hand, is the result of the same plot with the current (2013) mixing parameters as listed in Table 1.2. The nominal prediction (solid blue curve) is shifted up by about a factor of 0.04 compared to the old values (dashed blue curve). The same applies to the flavor ratios of the source types (dotted horizontal lines). The reason for this is mainly due to the measurement of $\theta_{13} > 0$. Moreover, the uncertainty band depicted as

¹⁰In the right plot of Fig. 2.3, the normalization of the muon neutrinos is still set to match the analytical WB flux prediction (thin dashed curve), as shown in Fig. 2.2. When we however use the integrated neutrino energy as the criterion for the normalization, the prediction is significantly lower (thin solid curve, labeled “total flux rescaled”). As can be seen from the yellow IceCube sensitivity limit, even the lower prediction should still have given a signal in IceCube. This issue is resolved when we introduce the self-consistent normalization based on the observed gamma rays later in this section. Finally, the differential sensitivity of Auger was included due to its capability to detect high-energy tau neutrino events [147], which could be visible due to the kaon component (plus flavor mixing).

¹¹The according uncertainties on the neutrino flux prediction are depicted as gray-shaded bands in the right plot of Fig. 2.3. Only the 2010 uncertainty is visible while the estimated ones for 2015 and 2025 are so small that they are below the thickness of the depicted curve. Hence, this uncertainty is negligible for astrophysical standards.

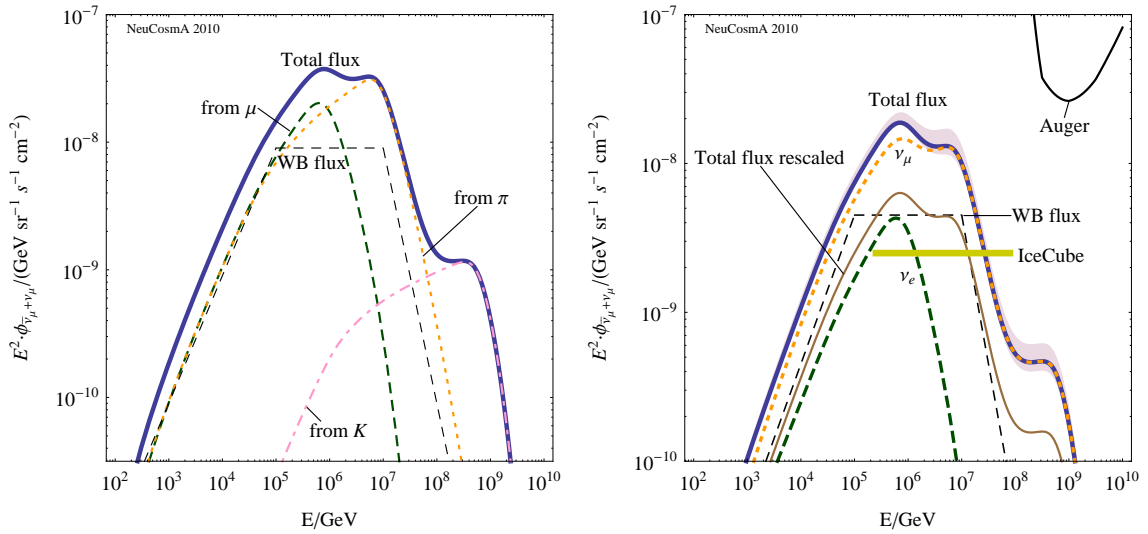


Figure 2.3.: In these two plots, taken from Ref. [82], we show how the predicted flux shape of the muon neutrino spectrum (thick solid blue curve) is changed due to the detailed particle physics treatment. In the left plot, it is detailed how the contributions from different parent particles, muons (dashed green curve), pions (dotted yellow curve), and kaons (gray dash-dotted curve), lead to the double peak structure with a high-energy component (due to kaons). The right plots shows that the general flux shape (solid blue curve) is unchanged when flavor mixing is included.

a shaded area along the nominal prediction is updated to the current uncertainties listed Table 1.2. Even though the uncertainty has significantly decreased compared to the 2010 values, it is still somewhat larger than the predicted 2015 uncertainty. This is not surprising as $\theta_{13} > 0$ directly leads to the CP-phase δ_{CP} being needed as an additional mixing parameter which again increases the uncertainty. For $\theta_{13} = 0$, as in the left plot, δ_{CP} could be treated as an arbitrary parameter.

To finally obtain a meaningful prediction of the neutrino flux, we still need to ensure that the spectra are correctly normalized. Since our code needs the particle (energy) densities, we first of all need to know what the actual energy output is. In this regard, it helps that due to the relativistic boosting, we can assume that the emission from the burst is isotropic, and not coming from a jet. Even though the actual energy output may actually be lower, we cannot tell from observations in gamma-rays, if the source is isotropic or not. Hence, we can use a simple isotropic formula, such as Eq. (B.12), which connects the observed flux with the luminosity. One important aspect of Eq. (B.12) is that it connects a quantity in the observer's frame (the flux F_γ) with one in the source frame (the luminosity L_{iso})¹². Hence, if we now want to use $L_{\gamma,\text{iso}}$ to calculate the energy $\tilde{E}_{\gamma,\text{iso}}$, we need to be aware that this calculation needs to be done in the source frame. It is therefore not possible to use the observed timescale, but the one corrected for the cosmic expansion. In case of neutrino flux predictions, it is normally assumed that it is sufficient to use average quantities, since the detection statistics in neutrino flux measurements are not high enough to give meaningful information on the temporal structure of the neutrino

¹²The luminosity is always in the source frame even though we do not denote it as \tilde{L} . This is only to match the convention in the literature.

flux. Therefore, instead of using the integrated luminosity over the duration \tilde{T}_{90} of the burst, we assume that it is sufficient to multiply the average luminosity with the duration. Consequently, the formula giving the energy $\tilde{E}_{\gamma,\text{iso}}$ in the source frame is

$$\tilde{E}_{\gamma,\text{iso}} = L_{\gamma,\text{iso}} \cdot \frac{T_{90}}{1+z} \quad , \quad (2.18)$$

which already includes the transformation of the observer's frame duration T_{90} to the source frame

$$\tilde{T}_{90} = \frac{T_{90}}{1+z} \quad . \quad (2.19)$$

As mentioned before, these formulas are only valid if we assume that $L_{\gamma,\text{iso}}$ is constant over T_{90} . This is, of course, not the case in reality. Real GRB light curves are rapidly varying, with the scale of these variations given by t_v , see discussion in Sec. 1.1.2. A naive estimate based on the variation is to assume that the burst consists of N identical shells, with the number of shells being calculated as

$$N = \frac{T_{90}}{t_v} \quad . \quad (2.20)$$

As can be easily imagined, this assumption of N identical shells giving rise to the burst is only a zeroth order approximation. A more realistic model would be to have different parameters for the different shells. There exist a number of models that allow for the calculation of artificial light curves based on several shells, see, *e.g.*, Refs. [39, 149]. In principle, it is possible to adapt these models to calculate the neutrino emission on a shell-per-shell-basis for a more detailed neutrino flux prediction from a (theoretical) burst. Nonetheless, for the calculations presented here, it is sufficient to assume that a burst consists of N identical shells. An additional aspect is the ambiguity of the luminosity/energy. As discussed in Sec. 1.1.2, there are subtle differences in the obtained results for the luminosity and/or energy depending on the energy range chosen for the calculation. For example, in Eq. (2.8), only the energy range from 1 keV to 10 MeV is used for the calculation of the energy in photons. This however neglects contributions from photons of higher or lower energy outside the specified range which can also contribute to the total energy. Bolometric quantities, such as the bolometric photon luminosity $L_{\gamma,\text{iso,bol}}$ or the corresponding bolometric energy $E_{\gamma,\text{iso,bol}}$, are defined to include the whole spectrum and not just a certain range. These should be used to calculate the total energy output of a burst. For this calculation of the total energy, it needs to be considered that $E_{\gamma,\text{iso,bol}}$ is only the energy in photons, which is only a certain fraction of the total energy. It is commonly assumed that in the internal shock model the emitted photons are directly connected to the electrons inside the fireball, either through synchrotron emission or through some other form of interaction. Hence, when we assume that the electrons lose all their energy as photons, then do the photons carry the fraction ϵ_e of the total energy $E_{\text{iso,tot}}$, and we can calculate $E_{\text{iso,tot}}$ using the formula, taken from Ref. [107],

$$E_{\text{iso,tot}} = \epsilon_e^{-1} \cdot E_{\gamma,\text{iso,bol}} \quad . \quad (2.21)$$

As discussed earlier in this section, our calculation of the photohadronic interactions needs to be done in the SRF, where both the photon and the proton densities are

isotropic. Based on basic considerations of relativistic boosting, we know that we can easily transform the energy to the SRF by $E'_{\text{iso,tot}} = E_{\text{iso,tot}}/\Gamma$. Since we however need the energy densities for our calculations, see *e.g.* Eq. (1.5), we also need the isotropic volume V'_{iso} (of a shell). Assuming that we have an observed burst, we can use the collision radius R'_c from Eq. (1.3) and the width of a shell $\Delta R'$ from Eq. (1.4) to estimate the volume

$$V'_{\text{iso}} \simeq 4\pi R'^2_c \cdot \Delta R' \quad (2.22)$$

$$\simeq 4\pi \left(2\Gamma^2 c \frac{t_v}{1+z}\right)^2 \cdot \left(\Gamma c \frac{t_v}{1+z}\right) \propto \Gamma^5 \quad , \quad (2.23)$$

assuming we have a thin shell ($R'_c \gg \Delta R'$), as discussed in Ref. [107]. While Eq. (2.22) is the general formula for any thin shell with a certain radius and a certain shell width, Eq. (2.23) only applies when the quantities are assumed to be fixed in the observer's frame. Especially, the strong dependence of V'_{iso} on Γ is a consequence of the choice to use observed timescales. Still, with these quantities we can now calculate the total energy density (per shell)

$$U'_{\text{tot}} = \frac{E'_{\text{iso,tot}}}{N V'_{\text{iso}}} \quad . \quad (2.24)$$

From this total energy density, it is now possible to derive different contributing energy densities, such as the energy density of the protons or the one of the magnetic field. As mentioned before, most of the time energy (equi-)partition arguments are used to compare the different parts to the total energy to another. In case of the magnetic field B , the corresponding fraction is ϵ_B . When we now want to use this to calculate the magnetic field strength B' from Eq. (1.5), we can directly relate the magnetic energy density to the energy density in photons giving

$$U'_B = \frac{\epsilon_B}{\epsilon_e} \cdot \frac{E'_{\gamma,\text{iso,bol}}}{N V'_{\text{iso}}} \quad \text{or} \quad B' = \sqrt{8\pi \frac{\epsilon_B}{\epsilon_e} \cdot \frac{E'_{\gamma,\text{iso,bol}}}{N V'_{\text{iso}}}} \quad . \quad (2.25)$$

As stated before, typical values for the energy fractions found in the literature are $\epsilon_B \sim \epsilon_e \simeq 0.1$, see, *e.g.*, Ref. [133]. For observed bursts, we can even derive a phenomenological formula for B' by inserting Eq. (2.23) and the standard values for the GRB parameters, already mentioned in Table 1.1, into Eq. (2.25), giving

$$B' \simeq 220 \left(\frac{\epsilon_B}{\epsilon_e}\right)^{\frac{1}{2}} \left(\frac{E_{\gamma,\text{iso,bol}}}{10^{53} \text{ erg}}\right)^{\frac{1}{2}} \left(\frac{\Gamma}{10^{2.5}}\right)^{-3} \left(\frac{t_v}{0.01 \text{ s}}\right)^{-1} \left(\frac{T_{90}}{10 \text{ s}}\right)^{-\frac{1}{2}} \left(\frac{1+z}{3}\right)^{\frac{3}{2}} \text{ kG} \quad , \quad (2.26)$$

taken from Ref. [107] and in consistency with Refs. [70, 116]. For a self-consistent model of a burst, it is essential that also the magnetic field inside the shock is known. In principle, plasma physics simulations can be done based on the magnetic field and the particle input to obtain the actual photon spectra (including synchrotron emission and Inverse Compton effect) as well as the maximal proton energy. A detailed calculation of these processes is needed for a final complete model of a GRB. However, for the sake of simplicity, we will not consider what the actual

processes are which lead to the acceleration of the electrons/photons as well as the protons. We will only use the heuristic argument that the particle spectra need to be there since we can detect them (or at least the photons). We will also assume that the observed photons are directly connected to the photons in the SRF, so that we can normalize the photon spectrum from Eq. (2.2) with the formula

$$\int \varepsilon' N'_\gamma(\varepsilon') d\varepsilon' = \frac{E'_{\gamma,\text{iso,bol}}}{N V'_{\text{iso}}} . \quad (2.27)$$

Note, that the normalization factor C'_γ is in $[\text{GeV}^{-1} \text{cm}^{-3}]$; $1 \text{ erg} = 624.15 \text{ GeV}$. For the proton spectrum, we can use a similar approach as for the photons, by comparing the electron/photon energy to the energy in protons. Normally, the ratio f_e is used in the literature for this purpose, which is the ratio of energy in electrons to energy in protons (f_e^{-1} : baryonic loading).¹³ Using the proton spectrum from Eq. (2.1), we obtain

$$\int E'_p N'_p(E'_p) dE'_p = \frac{1}{f_e} \frac{E'_{\gamma,\text{iso,bol}}}{N V'_{\text{iso}}} , \quad (2.28)$$

with the normally assumed value of $f_e \simeq 0.1$. While, however, the parameters of the photon spectrum are known from measurements, we need to make assumptions on the parameters of the proton spectrum. As stated before in Sec. 2.1, it is normally assumed that $\alpha_p \simeq 2$. For the full spectrum, as in Eq. (2.1), we nonetheless still need the maximal proton energy $E'_{p,\text{max}}$ before we can calculate the normalization factor C'_p . In principle, the calculation can be done in a similar fashion as the one for the critical energy of the secondaries, see Eq. (2.17). However, instead of comparing the decay and the synchrotron loss rate, we need to compare the acceleration rate with the dominant loss rate. Assuming efficient particle acceleration, the acceleration rate can be estimated based on the formulas from Ref. [6] as

$$t'_{\text{acc}}{}^{-1} = \eta \frac{c q B'}{E'} , \quad (2.29)$$

where η is the acceleration efficiency, and q the particle charge. Of course, the formula given in Eq. (2.29) is only an effective description of the acceleration via statistical processes (Fermi acceleration). As stated in Ref. [6], it only applies if the mean free path of the particles which should get accelerated is larger than their Larmor radius. A more detailed discussion of the said acceleration approach, as in Ref. [150], or of UHECR acceleration in plasmas in general, see, *e.g.*, the book by Schlickeiser [151], shows that such a treatment is a bit too simplistic. Nonetheless, we will use the aforementioned formula, since a more detailed treatment of the acceleration would include 3D simulations of the plasma, which is a different field by itself and goes beyond the scope of this work. Still, the acceleration rate needs to be compared to the different loss rates, such as the synchrotron loss rate $t'_{\text{syn}}{}^{-1}$ (see Eq. (2.15)), the photohadronic interaction rate $t'_{p\gamma}{}^{-1}$ (see Eq. (2.14)), and dynamical

¹³This definition of f_e is somewhat inconsistent with the definition of the other energy fractions ϵ_e and ϵ_B . The sum of all ϵ fractions should always give 1. However, for the standard values of $f_e \sim \epsilon_e \simeq 0.1$ the resulting ϵ_p would already be 1 and the sum larger than the plausible value. At some point in the future, this needs to be addressed, but for now we will keep the standard values as assumed in the literature.

rate of proton escape $t'_{\text{dyn}}{}^{-1}$. The dynamical escape rate is just the (inverse) time it takes an ultra-relativistic proton to cross the shell of width $\Delta R'$,

$$t'_{\text{dyn}}{}^{-1} = \frac{c}{\Delta R'} \quad . \quad (2.30)$$

This can easily be solved, when we assume that we can calculate the width using Eq. (1.4). Hence, $E'_{p,\text{max}}$ is obtained by solving the equation (see Ref. [152])

$$t'_{\text{acc}}{}^{-1}(E'_{p,\text{max}}) = \max [t'_{\text{dyn}}{}^{-1}, t'_{\text{syn}}{}^{-1}(E'_{p,\text{max}}), t'_{p\gamma}{}^{-1}(E'_{p,\text{max}})] \quad . \quad (2.31)$$

For most GRBs, it is sufficient to use $t'_{\text{dyn}}{}^{-1}$ and $t'_{\text{syn}}{}^{-1}$ for the calculation of $E'_{p,\text{max}}$, neglecting the effect of $t'_{p\gamma}{}^{-1}$. In the end, the important part is that target spectra from Eqs. (2.2) and (2.1) are correctly normalized.

Using all these ingredients, it is now possible to calculate a neutrino flux prediction based on the observed photon spectra. Based on the calculation of the photohadronic interactions and the weak decays, NeuCosmA returns the injection spectra Q' of the secondary particles (in $[\text{GeV}^{-1} \text{s}^{-1} \text{cm}^{-3}]$), including the ones for the neutrinos, see Appendix A for details. These need to be translated into an observable (neutrino) fluence \mathcal{F}^{sh} (in $[\text{GeV}^{-1} \text{cm}^{-2}]$, see Ref. [152]):

$$\mathcal{F}^{\text{sh}} = t_v V'_{\text{iso}} \frac{(1+z)^2}{4\pi d_L^2} Q' \quad . \quad (2.32)$$

As stated before, this can be related to the fluence of a whole burst by multiplying \mathcal{F}^{sh} with the number of shells N from Eq. (2.20).

An interesting aspect of this approach with a detailed particle physics treatment is that the new prediction is significantly lower than the one from the analytical approach described in Sec. 2.2. As we detailed in Ref. [136], several factors in the analytical approach lead to an overestimation of the neutrino flux prediction. The counterintuitive part in this regard is fact that our detailed particle physics treatment in NeuCosmA actually should lead to an enhancement of the neutrino production. However, as can be seen from Fig. 2.4, the enhancement of the flux prediction due to the detailed particle physics treatment (red arrow, labeled 2) is smaller than the correction on the neutrino flux normalization (blue arrow, labeled 1). It is curious that all the small inaccuracies of the analytical approach, such as the neglect of the energy losses of the secondaries in Eq. (2.8), add up to a large error instead of averaging out, see Ref. [136] for more details. Nonetheless, the experimental collaborations have picked up on this problem, and, with our help, ANTARES has published its first GRB neutrino results using a search optimized for a neutrino flux prediction obtained with NeuCosmA [153]. There are, however, additional uncertainties on the flux prediction which we want to discuss in the following section.

As a final remark, another advantage of the numerical treatment compared to analytical models is the possibility of using arbitrary spectra. Even though the GRB calculations in Refs. [107, 136] only use power-laws as input, it is in principle possible for the NeuCosmA code to calculate interactions with any kind of spectrum.

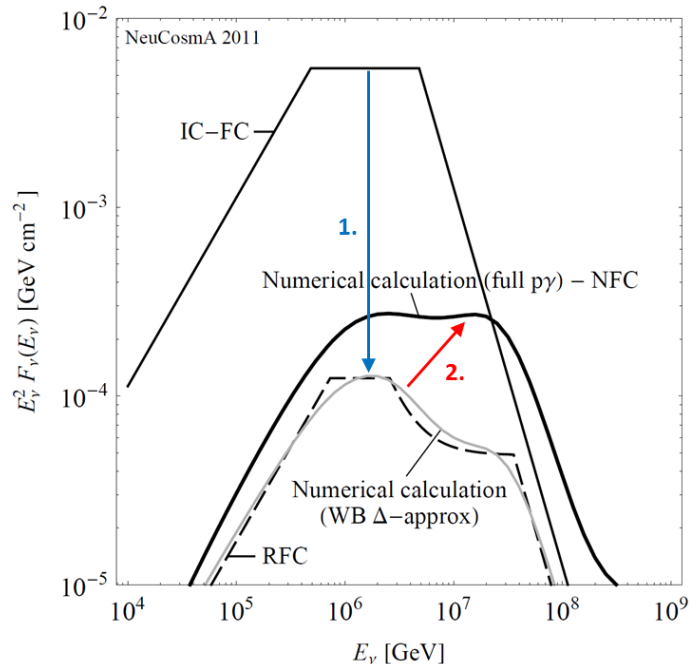


Figure 2.4.: Here we show how the analytical flux prediction, based on Refs. [70, 133], is first reduced due to corrections to the analytical model (blue arrow), and then again enhanced due to the detailed particle physics treatment (red arrow), as detailed in Sec. 2.3. The depicted figure is based on Ref. [136], where also more details on the analytical corrections can be found.

As has been shown in Ref. [154], it is feasible to use observed photon spectra as input for calculations. The neutrino flux can be calculated for any kind of target (photon) spectrum, as we can see later in chapter 6 when discussing neutrinos from microquasars.

2.4. Statistical effects affecting neutrino flux predictions

Even though we have now discussed the calculation of a single burst spectrum in detail in the previous sections, there are still several issues we need to discuss when we really want to understand diffuse flux bounds, such as the ones given in the experimental analyses in Refs. [133, 135, 153]. Apart from the open question what the actually correct model for GRBs is, there are even additional uncertainties inside the internal shock model. Moreover, it is common practice in astrophysics to perform stacking analyses, when single sources are not sufficient. This stacking is also used to obtain an estimate for the diffuse flux of a whole class of sources. Instead of the flux from very large number of unresolved sources (“diffuse flux”), a finite set of resolved sources is used to estimate the flux from all, resolved and unresolved, sources. The result of this estimate is a “quasi-diffuse flux” prediction. In this section, we want to take a brief look at the different kinds of effects, which complicate the process of predicting neutrino fluxes. First, we will discuss how the standard

parameters affect the prediction and how changing them alters the result. Then, we will extend the thought of the parameter values and discuss how distributions change the predictions. Especially, how the combined variation of redshift z and luminosity $L_{\gamma,\text{iso}}$ alters the shape and the normalization of the prediction. And finally, we will review the process of going from a limited set of bursts to a quasi-diffuse flux limit, which additionally introduces an uncertainty based on the choice of the sample.

As we discussed in the previous sections, the prediction of the neutrino flux depends on the parameters we can obtain from the measurements in gamma-rays and other wavelengths. From these we can obtain the observed duration T_{90} , the recorded variability timescale t_v , several types of the flux F_γ (or the fluence \mathcal{F}_γ , when we integrate over the burst) as well as the spectral parameters of the observed photon spectrum. Using various methods, it is possible to even derive the redshift z of the burst (or of its host galaxy). Afterwards, we can calculate derived quantities such as the luminosity $L_{\gamma,\text{iso}}$, as in Eq. (B.12), or the Lorentz factor Γ , see, *e.g.*, Ref. [70]. But at the latest, with the derived parameters the problems start. Even when all the properties of the light curve can be obtained from the recorded light curves, it is not possible to give an exact value for Γ . Other than for AGN jets, where the relativistic motion of blobs can be tracked, GRBs are only point-like events. For GRBs, all the limits on Γ are based on basic considerations on the geometry, the pair creation cutoff, or other connections to the relativistic beaming. In any case, all the calculations of bounds on Γ of a burst depend on several other parameters, which all are only known with a certain error. These errors are inherited by the Lorentz factor, and, finally, the neutrino flux prediction. As we showed in the previous section, especially the volume of the burst depends on Γ , see Eq. (2.23). As a consequence, the neutrino flux prediction goes with Γ^{-4} when the calculation is done for observed parameters, as we discuss in Ref. [107]. Hence, even small variations of Γ lead to a big difference in the neutrino flux prediction. The choice to use standard values for missing parameters is therefore a source of large uncertainties on flux predictions, be it the Lorentz factor Γ , the redshift z , or any of the other parameters of a GRB, see discussion in Refs. [107, 136]. In Fig. 2.5, taken from Ref. [136], the large band around the nominal flux prediction (black solid curve) depicts the uncertainty of the prediction when the GRB standard values were changed when using the 117 bursts of the IceCube 40-string configuration (IC40) sample [134]. For the band shown here, the Lorentz factor Γ was varied between 200 and 500, the variability time t_v between 10^{-3} s and 10^{-1} s, the proton spectral index α_p between 1.8 and 2.2, and the energy in electrons versus the magnetic field energy ϵ_e/ϵ_B from 0.1 to 10. As can be seen from the extrapolated sensitivity of IC86 (long dashed blue curve), it will take 10 years (or more) of measurements with the full IceCube telescope to rule out all the considered choices of the parameters in the internal shock model. Others, such as low factors of Γ , are already excluded by current bounds (solid blue curve for IC40 [134], dashed blue curve for IC40+59 [135]). This band would be reduced, if the uncertainties on the burst parameters were smaller or if only bursts with measured parameters were used.

Moreover, not all of the detected bursts are well enough documented/recorded in different wavelengths to obtain a value for z . As discussed by the authors of

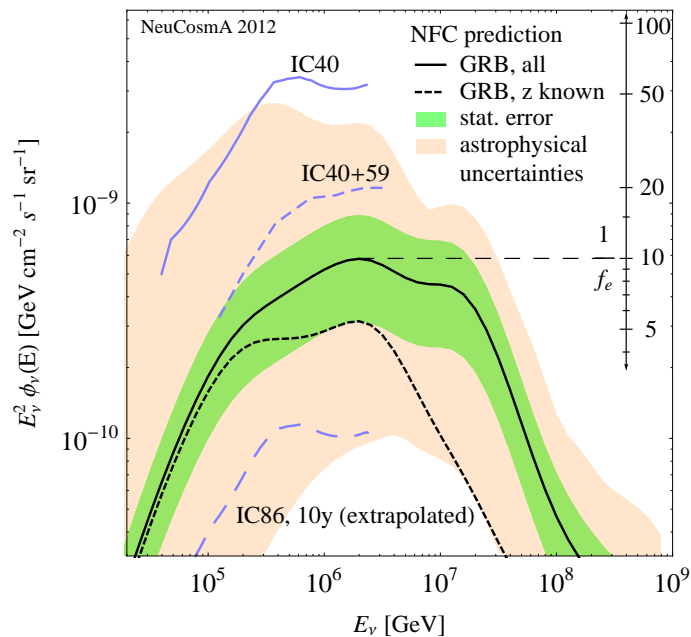


Figure 2.5.: The uncertainties on the updated quasi-diffuse neutrino flux prediction based on the 117 bursts of the IC40 GRB sample, taken from Ref. [136]. The nominal prediction is depicted as a solid black curve. The parameter uncertainty is from varying some of the standard parameters of the GRB (pink band), *i.e.* Γ , t_v , α_p , and ϵ_e/ϵ_B (see text for details). This band could be reduced by a conservative flux prediction based only on bursts with measured parameters. Following the idea of only using burst with measured parameters, we have depicted the flux prediction based on all bursts with measured redshift of the IC40 sample (dashed black curve). Additionally, the plot includes the statistical uncertainty as a green band, which arises from the extrapolation from the discrete sample of 117 bursts to a (quasi-)diffuse flux. As can be seen from the depicted IceCube bounds, some ranges of the parameter space are already excluded, while others need 10 more years (or more) of measurements until they are ruled out.

Ref. [155], only about 50% of the bursts in the *Swift* sample actually have a detected afterglow and only 30% of the sample have actually measured redshifts. And even in this comparably large sample — *Swift* has till now detected nearly 900 GRBs in total [156] — there are still too many open questions about the distribution in z for any clear conclusion. As detailed in Ref. [155], there seems to be a bias towards high redshifts, and general selection effects seem to have an effect on the results. Also, even though the theoretical connection of SFR and GRB rate seems reasonable, we cannot neglect the fact that there is still lots of discussion about what the actual GRB rate is. The approach we are using, see Eq. (1.7), is based on an approach to minimize the detector bias by using a certain minimal luminosity, see Ref. [87]. However, the authors of Ref. [157] obtain a different result by already taking into account that $L_{\gamma, \text{iso}}$ as well as z need to be varied simultaneously. This has two consequences: First of all, the assumed standard value of z may be wrong. This, of course, affects the flux predictions as they use standard values when a parameter is not measured. Therefore, conservative predictions can only be obtained with measured parameters, such as a prediction based on all bursts with measured z , depicted as a black dashed curve in Fig. 2.5. Secondly, when one actually wants to obtain the most probable value of z for a burst, not only the source distribution in

z is needed, but also the distribution in $L_{\gamma,\text{iso}}$. Considering this the total differential in z should be a combination of a redshift part and a luminosity part, which are connected through the measured F_γ , see Eq. (B.12). The simplest approach is to assume that these two parts factorize and the probability distribution is given by

$$\frac{\partial^2 P(z, L_{\gamma,\text{iso}})}{\partial z \partial L_{\gamma,\text{iso}}} = \frac{\partial P_1(z)}{\partial z} \cdot \frac{\partial P_2(L_{\gamma,\text{iso}})}{\partial L_{\gamma,\text{iso}}} \quad (2.33)$$

We can now use theoretical considerations to obtain models for the individual parts $\partial P_1(z)/\partial z$ and $\partial P_2(L_{\gamma,\text{iso}})/\partial L_{\gamma,\text{iso}}$. These parts should be connected to the derived redshift and luminosity distributions of GRBs. As before, we will use the approach proposed by Kistler et al. [87] of connecting the long GRB rate to the SFR together with a redshift dependent correction to match the GRB evolution to the star formation rate for $\partial P_1(z)/\partial z$, see Eq. (1.7). Be aware that it is not important that some normalization factors are not explicitly known, since most factors cancel in the end when the whole distribution is normalized to 1. Still, in principle any distribution in redshift can be used as $\partial P_1(z)/\partial z$. The only constraint is that the function needs to be normalized to run from 0 to 1 for redshift values from z_{min} to z_{max} .

Similar to this, we also need a distribution of bursts in luminosity. We here use the luminosity distribution obtained by Wanderman and Piran [157], even though other distributions such as the one from Ref. [158] can also be used. The authors of Ref. [157] assumed that the distribution in luminosity is a broken power law on a logarithmic scale of the form

$$\frac{\partial P_2}{\partial \log_{10}(L_{\gamma,\text{iso}})} \propto \begin{cases} \left(\frac{L}{L_*}\right)^{-\alpha} & L < L_* , \\ \left(\frac{L}{L_*}\right)^{-\beta} & L \geq L_* , \end{cases} \quad (2.34)$$

with the parameters $L_* = 10^{52.5} \text{ erg s}^{-1}$, $\alpha = 0.2$, and $\beta = 1.4$ being proposed in Ref. [157], see Eq. (17) of said reference. Depending on the actual sample, the numbers may vary, but the principle concept may be applied to any distribution, just as for the redshift distribution.

Using the connection given by Eq. (B.12), we can combine the two parts of the probability distribution to one total differential in z for known F_γ . As long as the individual parts are correctly normalized, the total differential can be obtained from

$$\begin{aligned} \left. \frac{dP}{dz} \right|_{F_\gamma} &= \frac{dP(z, L_{\gamma,\text{iso}}(z, F_\gamma))}{dz} = \frac{\partial P}{\partial z} + \frac{\partial P}{\partial \log_{10}(L_{\gamma,\text{iso}})} \frac{\partial \log_{10}(L_{\gamma,\text{iso}})}{\partial z} \Bigg|_{F_\gamma} \\ &= \frac{\partial P_1(z)}{\partial z} P_2(L_{\gamma,\text{iso}}) + P_1(z) \frac{\partial P_2(L_{\gamma,\text{iso}})}{\partial \log_{10}(L_{\gamma,\text{iso}})} \frac{2}{\ln(10) d_L(z)} \frac{\partial d_L(z)}{\partial z} \quad (2.35) \end{aligned}$$

When the partial functions $\partial P_1(z)/\partial z$ and $\partial P_2(L_{\gamma,\text{iso}})/\partial \log_{10}(L_{\gamma,\text{iso}})$ are already normalized, it is relatively easy to obtain the according functions $P_1(z)$ and $P_2(L_{\text{iso}})$ by integration. There is, unfortunately, one subtlety to this integration, which we cannot quite explain mathematically. The integration needs to be from the current value to infinity to conserve the normalization, and not from zero to the current value as one might expect.

$$P_1(z) = \int_z^\infty \frac{\partial P_1(\tilde{z})}{\partial \tilde{z}} d\tilde{z} \quad (2.36)$$

$$P_2(L_{\gamma,\text{iso}}) = \int_{\log_{10}(L_{\gamma,\text{iso}})}^\infty \frac{\partial P_2(\tilde{L}_{\text{iso}})}{\partial \log_{10}(\tilde{L}_{\gamma,\text{iso}})} d \log_{10}(\tilde{L}_{\gamma,\text{iso}}) \quad (2.37)$$

The integrated functions control the weighting of the two distributions in Eq. (2.35). Remember that we have chosen two independent distributions in z and $L_{\gamma,\text{iso}}$. For instance, $P_2(L_{\gamma,\text{iso}})$ parameterizes for which fraction of the parameter space (in $L_{\gamma,\text{iso}}$) the redshift distribution can be applied. In a way, it represents how many bursts are luminous enough to be detected from a certain redshift z . If the needed $L_{\gamma,\text{iso}}$ for that specific value of z is small, the redshift distribution can be applied over a wide range of z values, whereas for $L_{\gamma,\text{iso}} \gg L_\star$ in Eq. (2.34), it is unlikely that a burst is luminous enough to be detected from said z or beyond. Therefore, it is the integral from $L_{\gamma,\text{iso}}$ to ∞ which needs to be used, as it vanishes above the cutoff. In practice, the luminosity cutoff translates then in a z cutoff z_\star by Eq. (B.12) for large F_γ .

It can also be easily checked that Eq. (2.35) is normalized to one if integrated over z , *i.e.*,

$$\int_0^\infty \left. \frac{dP}{dz} \right|_{F_\gamma} dz = 1, \quad (2.38)$$

which is a consequence and a self-consistency check. Note that for calculation purposes a cutoff at a maximal redshift z_{max} is introduced, even though the GRB rate is actually non-vanishing. However, with the correct choice of the two weighting functions P_1 and P_2 in Eq. (2.35) it is possible to satisfy Eq. (2.38) for z_{max} . Examples for how the flux affects the total differential can be seen in Fig. 2.6, where we have depicted the total differentials dP/dz from Eq. (2.35) as a function of z for different values of F_γ in the range from $10^{-5.5}$ to $10^{-8} \text{ erg s}^{-1} \text{ cm}^{-2}$, see legend in plot. The shown functions are calculated from the redshift distribution given in Eq. (1.7) with an assumed $z_{\text{max}} = 6$ and the luminosity distribution given in Eq. (2.34). As can be seen from the plot, the most probable redshift, obtained from the total differential, can vary strongly depending on the observed flux. The result, that the total differential looks quite different than the pure distribution in redshift, is quite remarkable, but not very surprising. Especially bursts with high measured flux F_γ are now way more likely to originate from lower values of z . This is reasonable since the much larger distances for higher redshifts would need to be countered by higher luminosities $L_{\gamma,\text{iso}}$. These values of $L_{\gamma,\text{iso}}$ quickly reach unreasonably high values as z grows. Therefore, it should be more likely that a burst originates at lower z . As always, these result depend on the choice of the parameters, or in this case, on the choice of the parameterization of $\partial P_1(z)/\partial z$ and $\partial P_2(L_{\gamma,\text{iso}})/\partial \log_{10}(L_{\gamma,\text{iso}})$. One caveat of this approach is, however, that the distributions we used strictly only apply to long GRBs and not short GRBs. This can lead to a significant error in actual samples of bursts. Short GRBs have their own luminosity and redshift distributions which should be used to obtain the correct values.

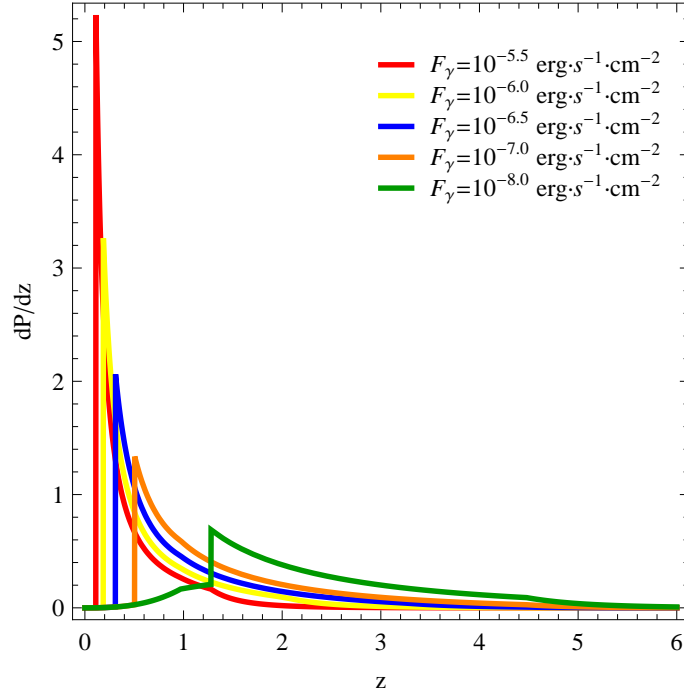


Figure 2.6.: The different functions are the probabilities dP/dz to detect a burst from certain redshift z , based on the flux F_γ . The total differential is calculated as detailed in Eq. (2.35), with the redshift distribution from Eq. (1.7) and the luminosity distribution from Eq. (2.34). Depending on the flux with which a burst is detected, the most probable value for z can be constrained to a very narrow range. Especially high observed values of F_γ lead to a high probability at low z .

A further effect is the statistical uncertainty when extrapolating from a small number of bursts to a quasi-diffuse limit, as discussed in Ref. [107]. Given that the parameters follow certain probability distributions, it is possible to do Monte-Carlo-sampling to generate a theoretical sample. If we now try to recreate the analytical input distribution based on the sampled values, we get different results depending on the sample size n as well as statistical fluctuations. This kind of extrapolation is however needed for all types of stacking analyses. Hence, the systematical error coming from the summation over a small number of bursts n due to statistical fluctuations is present in all estimates of quasi-diffuse fluxes. It is therefore not possible to neglect this when discussing bounds for neutrino telescopes, such as the Waxman-Bahcall bound [123]. In the following, we want to quantify this effect by varying the bursts in redshift z , assuming that the bursts are all alike and only at a different distance to the observer, as in Ref. [107].¹⁴ We will use the result obtained by sampling 100 000 bursts using the GRB rate from Eq. (1.7) as the diffuse reference limit, while using smaller samples of n bursts to quantify the effect of the extrapolation. Even though we will only discuss the effect of the variation of z , this applies to all kinds of parameters.

¹⁴For theoretical purposes, it is better to assume that the bursts are alike in the source frame and NOT the observer's frame. This allows for a discussion to be reduced to the effect of the different distance, leading to a different flux. Otherwise each flux value would lead to different parameters values such as for the luminosity depending on the choice of z . The deconvolution of the different effects due to the change of nearly all parameter is expectedly more complicated.

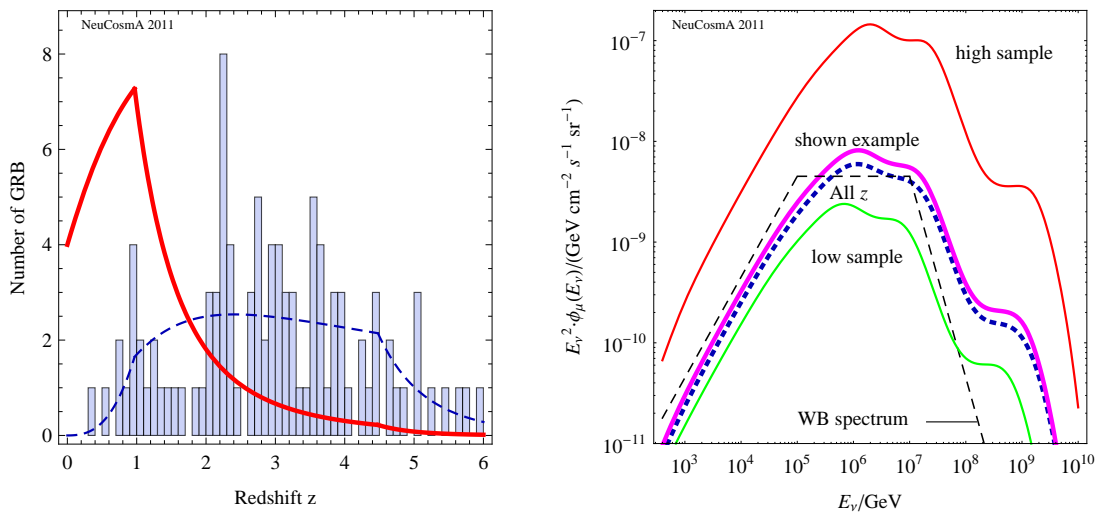


Figure 2.7.: This figure shows how a low number ($n = 100$) sample affects the result of the extrapolation to a quasi-diffuse flux. In the left plot, the histogram represents the number of GRBs in each redshift bin, while the dashed curve is the (normalized) probability function for a burst to be originating from a certain redshift, based on Eq. (1.7). The solid curve is the (theoretical) contribution of bursts from a redshift z to the total neutrino flux. This contribution from each z is calculated by folding the burst probability with the distance scaling d_L^{-2} . The right plot shows the resulting quasi-diffuse flux prediction based on the depicted sample as a solid thick curve. Even though the depicted sample gives a prediction close to the nominal one (thick dashed curve), there are still possibilities to obtain significantly different results. There are still extreme samples possible, such as the “high sample” and the “low sample”, represented by thin solid curves. These kinds of samples can still occur with a 0.1% probability. For comparison reasons, the classic WB flux shape is also included as a thin black dashed curve. Plots taken from Ref. [107].

A small sample of 100 randomly picked bursts, as depicted as a histogram in Fig. 2.7 (left panel), does not reproduce the initial function well (dashed curve). As can be seen from the comparison between the histogram and the dashed curve representing the distribution of bursts in z , there is quite some discrepancy. Moreover, when we consider that the flux of a burst of fixed luminosity from a certain redshift z is additionally suppressed by $d_L^{-2}(z)$, we can obtain the contribution of a certain redshift to the total flux by folding the GRB rate with the aforementioned suppression factor (solid curve). By comparing the peak of this curve to the histogram, it is obvious that only a small number of bursts will be responsible for the major part of the total flux. Hence, the fluctuations induced by some variation of the number of bursts at low z is quite strong. In the right panel of Fig. 2.7, we depict the resulting quasi-diffuse flux for the sample from the left panel (thick solid curve). This, however, deviates somewhat from the diffuse high statistics limit (dashed curve) due to the statistical fluctuations mentioned before. The fluctuations on the quasi-diffuse prediction can, nonetheless, be even higher, with the curves for two extreme examples of 100 burst samples depicted as thin solid curves. The probability for such extreme cases is, however, quite low with about 0.1%. Also, one has to remember that this result is for the variation of one parameter only. For more parameters, the errors should add up, in possibly Gaussian manner.

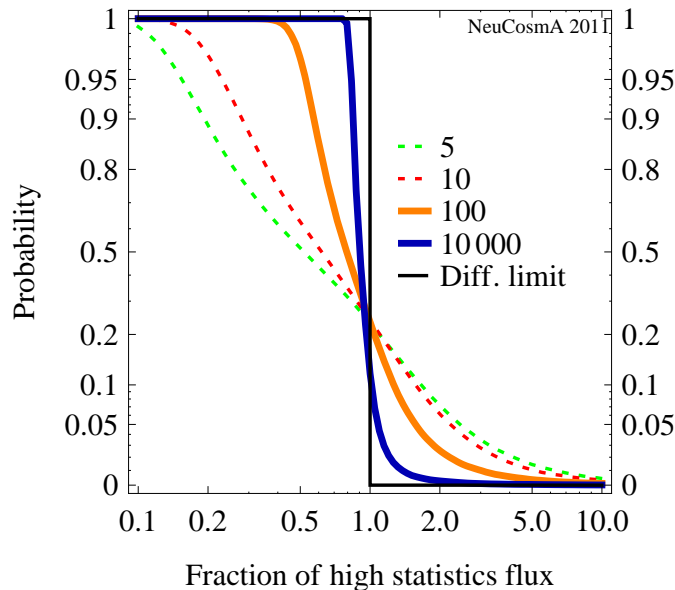
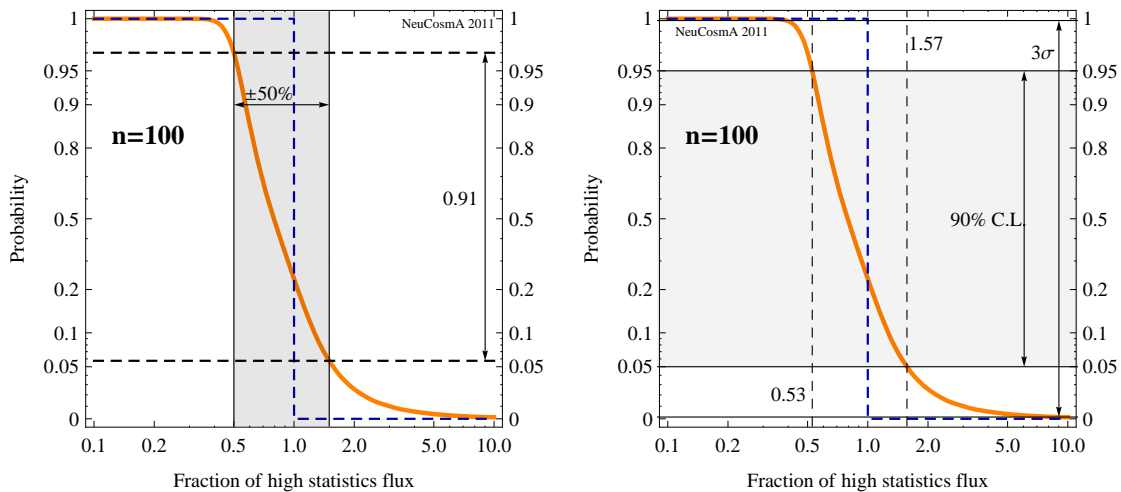


Figure 2.8.: Probability that the quasi-diffuse flux result from a small sample of n bursts is equal or larger than the fraction f of the diffuse limit. The different values of n can be taken from the legend inside the plot. The depicted function is equivalent to (one minus) the cumulative probability density function. The shown curves are calculated using the distribution in redshift based on Eq. (1.7). Taken from Ref. [107].

As we detailed in Ref. [107], it is not sufficient to show that such an effect depending on the sample size n exists, as done in Fig. 2.7, we also need to quantify the problem. For this, the following approach was used: We pick a large number of samples of size n and check what fraction f of the diffuse flux is obtained when extrapolating to the quasi-diffuse limit. Then we plot the probability to obtain a certain fraction f . By definition, the diffuse flux limit is a step function in this probability plot, see Fig. 2.8. For details on the approach, please refer to Ref. [107]. As can be expected, the smaller the size of the sample, the larger are the fluctuations. To give some numbers, assuming $n = 5$, the probability to obtain $f \leq 0.2$, which is equivalent with 20% of the nominal diffuse flux, is about $1 - 0.89 = 0.11$, while the probability of obtaining a result giving $f \geq 5.0$ (five times the diffuse flux) is less than 0.01. Even though Fig. 2.8 might be a bit complicated to read, it already contains all the information for the following discussions, and we will try to explain how to extract various forms of information from this figure.

For example, it is possible to determine how high the probability is that the quasi-diffuse flux prediction based on n bursts is within a certain range of the diffuse limit. This information is given in the left table of Table 2.1, with the upper left plot detailing how this information can be derived from Fig. 2.8. By defining a certain interval around the diffuse flux, it is possible to read of the probability as the range on the vertical axis. The table shows the results for several sizes, with $n = 10\,000$ giving the results closest to the diffuse limit. This number of 10 000 bursts is relevant for long-term GRB limits, *e.g.* assuming 1000 bursts per year over ten



n	$\pm 10\%$	$\pm 20\%$	$\pm 50\%$	n	Rel. error 90% CL	Rel. error 3σ
5	0.07	0.14	0.40	5	0.15 – 2.45	0.09 – 20.89
10	0.09	0.18	0.52	10	0.23 – 2.22	0.13 – 19.05
50	0.14	0.30	0.82	50	0.44 – 1.72	0.30 – 10.28
100	0.17	0.37	0.91	100	0.53 – 1.57	0.39 – 8.78
300	0.23	0.50	0.96	300	0.64 – 1.38	0.53 – 6.53
1000	0.30	0.69	0.98	1000	0.72 – 1.25	0.64 – 5.15
10000	0.48	0.97	0.99	10000	0.83 – 1.08	0.78 – 2.62

Table 2.1.: The left column shows how to obtain the probability that the quasi-diffuse flux limit based on a sample of size n is within a certain range of the nominal diffuse limit. The actual probabilities for a set of values of n can be found in the lower left table. The right column represents the possibility how to obtain the systematical error on the extrapolation of the quasi-diffuse flux based on the sample size n for different confidence levels. Again, the lower right table contains actual values for different n . The depicted examples in the upper row are for the $n = 100$ result from Fig. 2.8. As for said figure, all the results are based on a variation in z following Eq. (1.7). Taken from Ref. [107].

years of operation of IceCube. From a purely statistical point of view, the probability for a prediction based on 10 000 bursts to be within $\pm 20\%$ of the actual diffuse limit is 97%. Hence, even after such a long time still some fluctuations are to be expected. For current analyses with $n = \mathcal{O}(100)$ bursts, the probability is still quite low to be within $\pm 20\%$. For the IC40 analysis [134] with its 117 bursts, the probability is only about 0.37, while newer analysis, such as the current ANTARES analysis [153] based on 296 burst, should already have a 50% chance. Yet, for stacking analyses to be reliable, samples with $n = \mathcal{O}(1000)$ bursts are needed.

Another possibility to look at the probability plot is to ask what the variation in a certain probability window is. This is shown in the right column of Table 2.1. By fixing the probability to 90% ($99.73\% \equiv 3\sigma$) of all cases, we can use the curve to determine the range of f on the horizontal axis, see upper right plot in Table 2.1. The numbers derived with this method can therefore be used to estimate the systematical

error of the quasi-diffuse flux predictions on the according level of confidence. As can be seen from the results in the lower right table of Table 2.1, the systematical error for a quasi-diffuse flux based on 100 bursts is about 50%, 35% for 300 bursts, and still 25% for 1000 bursts at 90% CL. For comparison reasons, one needs to consider that the naive statistical estimate for the 1σ (90%) relative error from an extrapolation based on 100 bursts is only $1/\sqrt{100} \simeq 0.1$ (0.16), assuming that all bursts are at the same z . To correctly represent this systematical error in our prediction, we have included the green band in Fig. 2.5, based on our result for $n = 100$ bursts from Ref. [107]. Moreover, one needs to consider that the errors quoted here are for the variation of one parameter only. As soon as more parameters are varied, the error grows as well.

To conclude this section, we now want to use the statistical considerations we discussed so far to conduct a gedankenexperiment. Namely, how probable is it to actually detect a single burst based on a (detectable) diffuse flux in ten years of IceCube operation? Again, this is solely based on the strong evolution case of the redshift distribution, given in Eq. (1.7). Assuming that the diffuse GRB neutrino flux leads to $\mathcal{O}(100)$ events in the full IC86 detector during 10 years of operation, it may be possible to associate a certain number of neutrino events with a single burst. If, say, at least three events can be associated with a burst, a detection in gamma-rays would no longer be necessary to claim a detection. The probability for this to happen is dependent on the actual level of the diffuse flux. If the diffuse flux actually saturates the original WB flux bound [123], the burst only needs to contribute about $1/30$ to the total diffuse flux. Correspondingly, when the diffuse flux is one order of magnitude below the WB flux bound, the burst already needs to contribute $1/3$ of the total flux. As detailed in Ref. [107], we can use this to derive that the maximal redshift for the bright bursts, *i.e.* obtaining $z_{\max,1} \simeq 0.14$ for the first and $z_{\max,2} \simeq 0.05$ for the second case. Based on Eq. (2.36), we can now obtain that the integrated probability in the two cases is $P(z \leq 0.14) = 5 \cdot 10^{-5}$ and $P(z \leq 0.05) = 2 \cdot 10^{-6}$, respectively. Now, considering that we expect $\mathcal{O}(10\,000)$ bursts during the ten years of IceCube operation, we can calculate the probability that a burst is close enough to be detected in neutrinos without needing the gamma-ray counterpart. The probability for at least one burst being close enough is given by $1 - [1 - P(z \leq z_{\max})]^n$ with $n = 10\,000$, leading to a 40% chance in the case the WB bound is saturated, while it drops to 2% when the diffuse neutrino flux is one order of magnitude smaller. Hence, depending on the actual value of the neutrino flux from GRBs, there might still be the possibility of detecting a single burst in neutrinos.

2.5. The current ANTARES GRB neutrino analysis

After having discussed how the neutrino fluxes from individual bursts are actually calculated based on the gamma-ray observations, we now want to come to one recent example of the application of our NeuCosmA-model. As mentioned before, the current ANTARES GRB neutrino analysis [153] is the first experimental search

for GRB neutrinos which utilizes an updated model for the prompt neutrino flux prediction. While the current results by IceCube [133, 135] still use the analytical Guetta et al.-model and its extensions, which we discussed in Sec. 2.2, and have been rightfully criticized for this aspect [136, 137, 138], the ANTARES collaboration has already decided to adapt their search strategy based on our revised theoretical calculations. In the following, we want to detail how the theoretical flux prediction from 296 GRBs is obtained for said search.

ANTARES [14] is an underwater neutrino telescope in the Mediterranean Sea, which gives it a complementary field of view to IceCube at the South Pole. However, due to the smaller instrumented volume ($\sim 0.01 \text{ km}^3$ with the 12 current strings) and different backgrounds, *e.g.* bioluminescence inside the sea water, it does not reach the sensitivity of IceCube yet. For the current GRB analysis, neutrino data from the end of 2007 to 2011 has been used, spanning the end of the commissioning phase (December 6, 2007 till May 28, 2008) as well as time with the full detector until (and including) 2011. The amount of data from those nearly four years is then reduced based on timing and other cuts, to only contain data which coincides with an appropriate GRB. This reduces the data applicable for the search to a total of 6.6 hours of integrated live-time, which is already a significant cut on the amount of data. While details on the process of the data reduction can be taken from Ref. [153], we want to focus on the other selection process: the one for the GRBs. In the period from the end of 2007 to 2011, the different satellite experiments detected a total of 1110 GRBs of which only 942 are actually long GRBs. As discussed in Sec. 1.1.1, the internal shock fireball model only applies to long GRBs, and not to short ones. Hence, all short GRBs need to be excluded. For 930 of the 942 long GRBs, the observed photon data is sufficient to derive a spectrum and its parameters. Since atmospheric background events limit the detection of cosmic neutrinos in ANTARES to up-going events, only about 50% of the bursts are actually in the field of view of ANTARES, further reducing the number of bursts to 508. Finally, due to the detector only running a limited period of time and also needing stable data-taking conditions, the GRB sample is reduced to 296 bursts, see Fig. 2.9 for a distribution of the bursts in equatorial coordinates.

The data for these 296 bursts is taken from different catalogs, which need to be carefully combined. Since the instruments on *Swift*¹⁵, *Fermi*¹⁶, and the satellites of the Galactic Coordinates Network (GCN)¹⁷ all have different energy ranges, resolutions, and sensitivities, the data processing before the actual calculation of the neutrino flux prediction is vital. In case one of the burst parameters cannot be obtained from the observed data, we again use standard values, as done in the IceCube analyses [133, 135]. The used standard values can be found in Table 2.2. They are essentially the same as the ones used in the IceCube analysis, to ensure that the results are comparable. As we already discussed in Sec. 2.4, using standard values

¹⁵*Swift* catalog: [HTTP://SWIFT.GSFC.NASA.GOV/DOCS/SWIFT/ARCHIVE/GRB_TABLE.HTML](http://SWIFT.GSFC.NASA.GOV/DOCS/SWIFT/ARCHIVE/GRB_TABLE.HTML),
 BAT2 catalog: [HTTP://VIZIER.U-STRASBG.FR/VIZ-BIN/VIZIER?-SOURCE=J/APJS/195/2](http://VIZIER.U-STRASBG.FR/VIZ-BIN/VIZIER?-SOURCE=J/APJS/195/2),
 see also Ref. [61]

¹⁶*Fermi* GBM catalog: [HTTP://HEASARC.GSFC.NASA.GOV/W3BROWSE/FERMI/FERMIGBRST.HTML](http://HEASARC.GSFC.NASA.GOV/W3BROWSE/FERMI/FERMIGBRST.HTML)

¹⁷GCN: [HTTP://GCN.GSFC.NASA.GOV/GCN3_ARCHIVE.HTML](http://GCN.GSFC.NASA.GOV/GCN3_ARCHIVE.HTML)

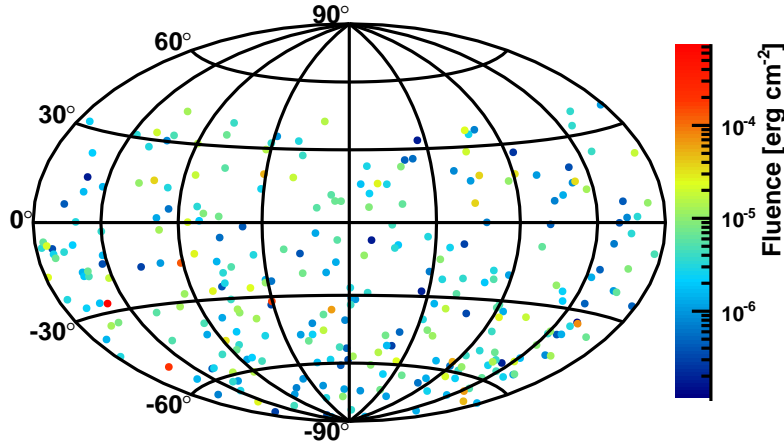


Figure 2.9.: Distribution of the 296 GRBs of the ANTARES GRB analysis in equatorial coordinates, taken from Ref. [153].

$\alpha_\gamma = 1$	$\beta_\gamma = \alpha_\gamma + 1$	$\varepsilon_{\gamma,peak} = 200 \text{ keV}$
$z = 2.15$	$L_{\gamma,iso} = 10^{52} \text{ erg s}^{-1}$	
$\Gamma = 316$	$\epsilon_e = 0.1$	$\epsilon_B = 0.1$
$f_e = 0.1$	$\langle x_{p \rightarrow \pi} \rangle = 0.2$	$t_v = 0.01 \text{ s}$

Table 2.2.: The standard values for possibly unknown parameters, which are used in the ANTARES analysis. These are essentially the same values as used in the IceCube analyses [133, 135], based on comparability reasons. Other than in most of the previous discussions, the values here are fixed in the observer’s frame, since we use real observed bursts as basis for the calculations. The burst duration is not listed, because it is always measured.

introduces an uncertainty on the flux prediction as well as the extrapolation to the quasi-diffuse limit. Therefore, all the limits shown in the analysis are also subject to these uncertainties, as depicted in Fig. 2.5. Especially, all bursts are assumed to have the same Lorentz factor, as none of the used catalogs contained information on this quantity. As we already detailed, the neutrino flux predictions are very sensitive to the chosen value of this parameter. Moreover, since not all redshifts are known, we cannot always calculate the actual burst luminosity from the observed flux. However, instead of calculating the luminosity from the standard value for z and the observed flux, a standard value for $L_{\gamma,iso}$ is used. While neither of the approaches gives the most probable result, as discussed in Sec. 2.4, the first approach would be preferable, as it is at least self-consistent. Since the approach with fixed luminosity has so far been used in neutrino flux predictions, see Refs. [133, 135] as well as the re-analysis with NeuCosmA from Ref. [136], we choose to keep this for now. The only parameter, which is always measured, is the duration of the burst. Either by the difference of the start and stop time of the gamma-ray observations, or a value for T_{90} was directly given in one of the catalogs.

For the calculation of the neutrino spectra of the different bursts, we use an adapted version of the code used in Ref. [136]. Said code allows for an automatic calculation of the individual neutrino spectra as well as the summed spectra over all bursts. Based on the parameters of the 296 bursts, we calculate the neutrino

spectra at the observer, including all the effects mentioned in Sec. 2.3. The resulting $\nu_\mu + \bar{\nu}_\mu$ fluence can be seen in Fig. 2.10. The summed fluence prediction (thick curve in lower plot of Fig. 2.10) is dominated by a few very energetic bursts. In the interesting range above 10^6 GeV, it is GRB110918 [159] which is predicted to dominate the neutrino fluence (highest one of the thin curves in the lower plot, also depicted individually in upper plot). This again stresses that we can have high fluctuations, based on the actual sample, as previously discussed in Fig. 2.7. Without the exceptional burst GRB110918, the result would be very different. The reason for this dominance can be found in the relatively low redshift $z = 0.982$ as well as the high-energy output of $E_{\gamma,\text{iso}} = 1.9 \cdot 10^{54}$ erg. This energy leads to an average luminosity of $L_{\gamma,\text{iso}} = 5.5 \cdot 10^{52}$ ergs $^{-1}$, assuming an observed duration of $T_{100} = 69.4$ s. Hence, the luminosity is only higher by a factor of five than assumed for a standard burst, however, the combination of the higher luminosity and the longer duration (usually assumed duration is $T = 10$ s) leads to the high neutrino fluence. It is not due to the Lorentz factor, which normally is expected to have the biggest effect on the neutrino flux prediction, since $\Gamma = 316$ is fixed for all bursts of the sample. Moreover, at the example of GRB110918, we can again see the differences between the analytical prediction based on Guetta et al. (blue curve) and the numerical NeuCosmA prediction (red curve), see upper plot of Fig. 2.10. The NeuCosmA prediction is about one order of magnitude lower than the analytical one at the lower break of the analytical model. However, due to the added effects through the more detailed particle physics treatment, the difference gets smaller at higher energies. Even with the extended model with two breaks (blue dashed curve), the qualitative difference does not change. The NeuCosmA prediction only exceeds the analytical prediction above 10^7 GeV (above $\sim 10^8$ GeV for the extended model), due to the kaon contribution. As stated several times before, it is not possible to make a general statement such as “the revised models reduce the flux prediction by one order of magnitude”.

Since the unblinding of the data after background subtraction and similar tests did not bring any associated neutrino events, see Ref. [153] for details, again only flux limits can be set. The summed neutrino spectra are transformed to a quasi-diffuse neutrino flux prediction using the assumption of 667 long GRBs per year:

$$E^2\phi_\nu = \sum_{i=1}^{296} E_i^2 F_{\nu,i} \cdot \frac{1}{4\pi} \cdot \frac{1}{N_{\text{GRB}}} \cdot 667 \text{ yr}^{-1} \quad , \quad (2.39)$$

where ν stands for $\nu_\mu + \bar{\nu}_\mu$, and the input fluence $E_i^2 F_{\nu,i}$ is in [GeV cm $^{-2}$] and the output flux $E^2\phi_\nu$ in [GeV cm $^{-2}$ s $^{-1}$ sr $^{-1}$]. In principle, the calculation does the following: First, the average fluence per burst is obtained. Then, it is scaled with the assumed burst rate to obtain a flux. Finally, the division with 4π gives the average flux per solid angle, assuming an isotropic flux. As shown in the discussion around Table 2.1, this approach still has a relative error of $\pm 35\%$ at 90% C.L. (solely based on the variation of z). Therefore, as can be seen from Fig. 2.11, the current flux limits only start to cut into the possible range of the diffuse GRB neutrino flux. Moreover, it again shows that the flux limits themselves are not so much affected by the change from analytical to numerical calculations, see lower plot in Fig. 2.11. Here, the ANTARES limit for NeuCosmA (red dashed curve) and the ANTARES

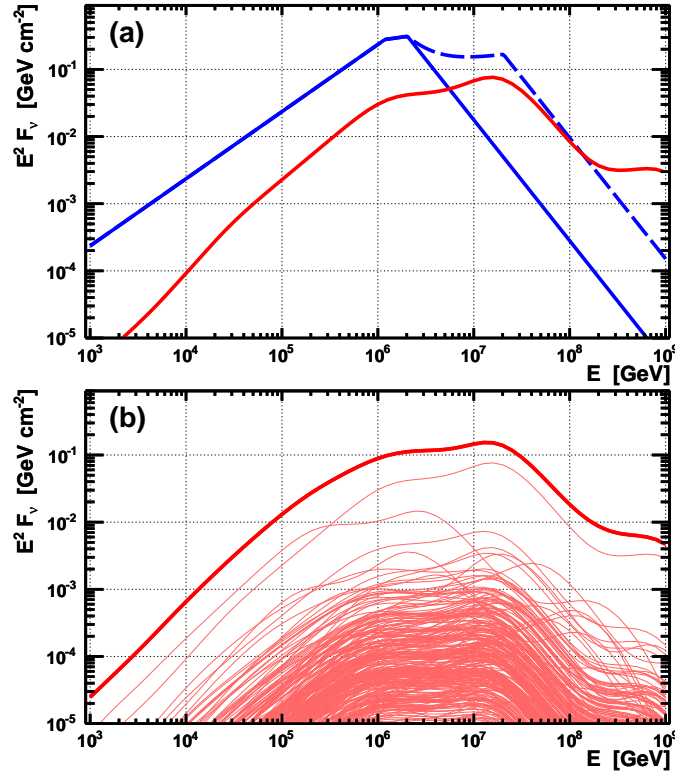


Figure 2.10.: (a): The expected muon neutrino ($\nu_\mu + \bar{\nu}_\mu$) spectra for the dominating GRB110918. The solid blue curve represents the analytical calculation based on Guetta et al., with the break based on the critical energy for muons. The extended model (dashed blue curve) also includes the second break based on the critical energy of pions. The red curve represents the NeuCosmA prediction for GRB110918. As discussed before, the NeuCosmA prediction is lower than the analytical prediction, and also changes the predicted shape of the neutrino spectrum. (b): The summed muon neutrino spectra of the 296 bursts of the full sample (thick red curve). Additionally, the predictions for the individual bursts have been included as thin red curves. The highest of the thin curves corresponds to GRB110918 from the upper panel. Plots taken from Ref. [153].

limit for Guetta et al (blue dashed curve) differ only by a small margin. What changes is the interpretation of these limits. While the current IceCube (IC40+59) bounds (black dashed curve) already rule out the analytical neutrino flux prediction, the NeuCosmA prediction is still not touched. The ANTARES bounds are so far not as strict as the ones from IceCube. Still, considering that the instrumented volume of ANTARES is smaller by about a factor of 100, it is remarkable that the sensitivity of the current ANTARES GRB search is only one order of magnitude worse than the one of IceCube. Additionally, when using the flux bounds on GRB110918 (upper plot in Fig. 2.11), it shows that ANTARES GRB searches are still two orders of magnitude away from detecting a single bright burst. Accordingly, the sensitivity of IceCube would currently still need to improve by one order of magnitude for a single burst detection. Nonetheless, with IceCube now running with 86 strings and the prospect of KM3NeT taking over for ANTARES, it should only be a matter of time until the sensitivity of the neutrino telescopes is high enough to really start to rule out models. Not only on the basis of the quasi-diffuse flux (which should take the full IceCube detector about 10 years of operation, see Fig. 2.5), but also on the possible observations of single bursts.

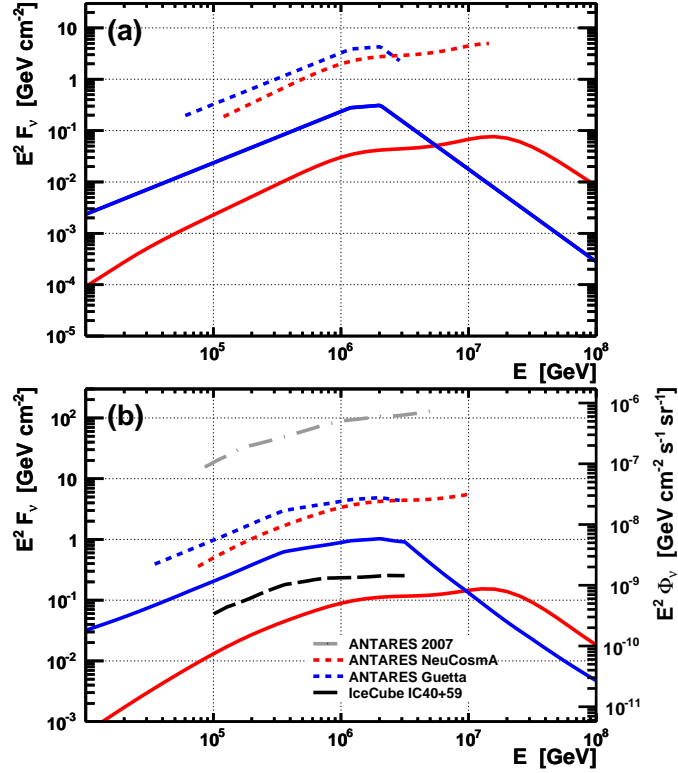


Figure 2.11.: (a): Predicted muon neutrino spectra for GRB110918 (solid curves) together with the 90% C.L. flux limits (dashed curves) based on the ANTARES sensitivity. The result for the analytical prediction based on Guetta et al. (blue curves) as well as for the NeuCosmA prediction (red curves) are shown.

(b): Quasi-diffuse neutrino flux prediction using Eq. (2.39) for the analytical (solid blue curve) and the NeuCosmA prediction (solid red curve). The according ANTARES diffuse flux limits are included as color-coded dashed curves. Moreover, the current IceCube IC40+59 limit (black dashed curve) from Ref. [135] and the limit of the first ANTARES GRB analysis [160] (gray dash-dotted curve) are shown.

3. Models for UHECR escape from GRBs

The ultimate goal of multi-messenger physics is to obtain as much information as possible about a source from all the different particles (messengers) which can originate from said source. With a knowledge of all possible messengers, it is feasible to gain an even greater amount of information from observed data. By combining the datasets of different messengers, such as gamma-rays, neutrinos, and cosmic rays, a more detailed picture of a source can be obtained. In the case of GRBs, this multi-messenger aspect can be used in various ways. One of the basic aspects quoted for the sake of neutrino searches is the possibility of GRBs accelerating protons to the highest energies. If this assumption is true, then a prompt neutrino flux is a direct consequence of the simultaneous presence of protons and photons in the source. As has been discussed in chapter 2, we can estimate the neutrino flux based on the observed gamma-ray (photon) spectrum. By using timing information and measurements in different wavebands, we can obtain the parameters of a burst needed for the calculation of the prompt neutrino flux. However, we can also get a neutron flux in the same calculation leading to the neutrinos, see Eq. (1.2). If we now consider that these neutrons, as opposed to protons, are not magnetically confined inside the shell (or the jet in general), we can deduce that there must be a cosmic ray component due to the escaping neutrons, which decay outside the source via Eq. (2.12). This is the standard (optically thin) neutron escape model, as discussed in, *e.g.*, Refs. [135, 161]. In the following section, we will review this model based on parameters normally assumed for the internal shock GRB fireball model. We will discuss how the neutron flux may be limited depending on the assumed particle densities inside the shells, and how this affects the neutrino flux in relation. We will compare to current neutrino bounds based on CR calculations and will discuss their applicability. In a second section, we will look into the expansion of the shell and how it affects the particle spectra. Based on these considerations, we will introduce an additional component of escaping cosmic ray protons, which may help to circumvent current observational bounds. We will dedicate one section on the discussion how the GRB parameters determine the dominating CR escape mechanism. In a final section, we will test our theoretical CR escape model on actually measured bursts.

3.1. The classic neutron escape model for CR escape

In the current IceCube GRB neutrino analysis, see Ref. [135], GRB models are constrained using two different approaches. The first one is based on the neutrino flux prediction based on the observed gamma-ray data, based on Refs. [70, 133]. As mentioned before, the results of this analysis are shown to be flawed based on

the theoretical model used for the calculation, see Refs. [136, 137, 138]. However, the second approach utilizes the connection of the neutrinos and the cosmic rays. Here, the argumentation is based on the one-to-one correlation of escaping neutrons to neutrinos from π^+ -decays. In the Δ -resonance approximation, a π^+ is always accompanied by a n , see Eq. (1.2). While the decay of the π^+ leads to one ν_μ (see Eq. (2.9) and after flavor mixing), the one of the neutron leads to the production of a proton (see Eq. (2.12)), which can contribute to the CRs. As has been done in various publications, this correlation can be used to calculate upper bounds for the neutrinos, which additionally constrain the GRB models. Or, as it is claimed in Refs. [135, 161], it is already doubtful that GRBs can actually be the main source of the extra-galactic cosmic rays.

As stated before, the principle idea for comparing the neutrino and the cosmic ray data is due to the connection of these two messengers, established by the Δ -resonance decaying into a neutron and a charged pion. An important aspect of this approach is that the particles can escape from the source. In general, it is assumed that the neutrons can escape from the source and decay afterwards while the pions decay inside the source and only the neutrinos escape. Then, after applying the appropriate losses and scaling, it is possible to calculate the amount of neutrinos and cosmic rays reaching Earth. With the results, a normalized neutrino flux prediction can be directly obtained by rescaling the CR prediction to the measured CR flux. Using this approach, the authors of Refs. [161, 162] as well as others already obtained results which question the possibility of GRBs being the source of the UHECR. These results consistently show that the expected neutrino flux would have to be so high, that neutrinos from GRB would have already been detected [135]. Unfortunately, there is one aspect which actually limits the applicability of these results, namely it is only applicable to sources which are optically thin to neutron escape. Since photohadronic interactions also apply to neutrons due to isospin symmetry, it needs to be considered that the interaction length for neutrons changes depending on the burst parameters. For our purposes, we define the optical thickness to neutron escape as done in Ref. [152] as

$$\tau_n \equiv \left. \frac{t'_{p\gamma}{}^{-1}}{t'_{\text{dyn}}{}^{-1}} \right|_{E'_{p,\text{max}}} \quad (3.1)$$

directly at the maximal proton energy $E'_{p,\text{max}}$, using the timescales from Eqs. (2.14) and (2.30). With this definition it is possible to calculate the ratio of escaping to photohadronically interacting particles. Hence, in a simplistic approach, $\tau_n \geq 1$ defines if a source can be considered to be optically thick. More detailed calculations of the electromagnetic cascades and related processes actually show that a value of $\tau_n \geq 2/3$ might already be sufficient that particles do not escape, see Ref. [163]. However, for the calculations in this work, as in Ref. [152], we will use the value 1 as the border between optically thin and thick. As soon as the photohadronic interaction length is shorter than the dynamical escape length, it is more probable for a particle to interact than to escape from the burst. Hence, the neutrino production will be enhanced compared to the neutron escape. Therefore, the one-to-one correspondence of neutrinos to cosmic rays does not hold for optically thick

sources. Still, the obtained neutrino bounds in the optically thick case should actually be stronger. We will discuss this in detail in Sec. 3.3 when we also include the additional component introduced in the next section.

3.2. Possible leakage of CR protons from GRBs

Another aspect of the approach used to relate CR to ν is that the protons are assumed to be trapped inside the source. When the target protons now were able to escape after acceleration without interacting photohadronically, then the resulting CR flux would no longer be accompanied by a neutrino signal. If such a CR component existed, then the neutrino bounds derived in Refs. [135, 161] would no longer be in contradiction to the UHECR data. As was discussed in the previous section, it is normally assumed that neutrons as well as neutrinos can escape from the shell unhindered. This whole approach can however be generalized to be applicable to all kinds of particles. On a microphysics level, all particles can travel a certain distance without interacting. The distance a particle can travel on average is given by the mean free path λ'_{mfp} , which depends on various limiting factors. The particle properties as well as the density of background fields of photons or other particles lead to different possibilities of interactions.

For protons, we can assume that the following three length scales can limit λ'_{mfp} : the size of the shell $\Delta r'$ given by Eq. (1.4), the photohadronic interaction length $ct'_{p\gamma}$, and the Larmor radius R'_L . The size of the shell is needed to normalize λ'_{mfp} , since we are only interested in particles which can travel from one side of the shell to the other without interacting, which is equivalent to always escaping. As we have discussed for the neutrons in the previous section, the photohadronic interactions can also be very high for the protons, hence the second factor. Additionally, as protons carry a net charge, they are subject to deflections in magnetic fields. Using the Larmor radius to estimate λ'_{mfp} is a rough approximation, which is valid in lowest order. This of course neglects all forms of turbulence and assumes that the magnetic field is homogeneous. Detailed modeling of the plasma physics involved should give shorter length scales, but for our purposes R'_L is sufficient and directly obtainable from the burst parameters. The general equation for the Larmor radius is given by

$$R'_L = \frac{E'}{q c B'} \quad (3.2)$$

where E' is the charged particles energy in the SRF, q is the particle charge, *e.g.* $q = e$ for protons or electrons, and B' is the magnetic field. With this formula it is possible to calculate the mean free path of the protons as well as the neutrons based on their energy, as

$$\lambda'_{\text{mfp}}(E') = \min [\Delta r', R'_L(E'), ct'_{p\gamma}(E')] \quad (3.3)$$

When we now want to know what fraction of particles f_{esc} can actually escape, we need to compare the “edge” region, from which particles can escape without

interacting, to the size of the whole shell. Therefore, the fraction of escaping particles f_{esc} can be estimated as

$$f_{\text{esc}} \equiv \frac{V'_{\text{direct}}}{V'_{\text{iso}}} \simeq \frac{\lambda'_{\text{mfp}}}{\Delta r'} \quad , \quad (3.4)$$

as we discuss in detail in Ref. [152]. Even though the final fraction contains several approximations, it is a good estimate for the amount of escaping particles. What we, however, so far have neglected is the evolution of the source.

Since not all collisions occur at the same fixed radius, and not all shells are expected to have the same width, it should be considered where the particles actually escape. Or, if the particles might escape at some later point after the acceleration. For this, we have to consider how the quantities scale as the burst expands. To quantify these effects, we will use the scaling given in Ref. [69]. The key aspect of this approach is that the shell width $\Delta R'$ can no longer be assumed to be fixed beyond a certain point, which roughly coincides with the collision radius. Beyond this point, $\Delta R' \propto r$ with r being the radius from the central engine, or, in other words, grows linearly with time ($\Delta R' \propto t$). Since the photospheric radius is considered to be smaller than the collision radius, it normally is assumed that the electrons and protons inside the plasma have already decoupled from the photons. Due to this decoupling and the expansion, it is assumed that the particles are subject to adiabatic losses. Based on the assumed densities and neglecting coupled plasma effects, the particle density can be considered to be a relativistic gas, with the relation of energy and volume given by

$$E' \propto V'^{-\hat{\gamma}-1} \propto r^{-1} \quad . \quad (3.5)$$

In this formula, $\hat{\gamma}$ is the adiabatic index, which we assume to be $\hat{\gamma} = 4/3$ (relativistic gas). Moreover, we can use this formula to derive the scaling of the magnetic field B' , since we know that it is related to the total energy and the volume as in Eq. (1.5), giving

$$B' \propto \sqrt{\frac{E'}{V'}} \propto r^{-2} \quad . \quad (3.6)$$

As we discussed in Ref. [152], it is possible to also obtain conclusions for individual particles. The main assumption is that the energy of a single particle scales in the same way as the energy of the whole gas/plasma. Since the Larmor radius R'_L scales with the particle energy and the magnetic field, see Eq. (3.2), we can now derive how said radius evolves with distance from the central engine. By plugging Eqs. (3.5) and (3.6) into Eq. (3.2), we obtain

$$R'_L \propto \frac{E'}{B'} \propto r \quad . \quad (3.7)$$

Hence, if our scaling applies, then R'_L grows with the radius, just as the width of the shell.¹ When we now assume that λ'_{mfp} of the protons is limited by said Larmor

¹We have here only discussed the case of a relativistic gas. For a discussion of different types of adiabatic scaling, *e.g.* for a mono-atomic gas, please refer to the more detailed discussion in Ref. [152].

radius, *e.g.* as in the optically thin neutron escape case, then the escaping fraction of particles f_{esc} is independent of the radius. Nonetheless, one should be aware that all these considerations are only true if the assumed scaling assumptions hold. For example, in plasma physics there is a significant difference between the magnetic field perpendicular and parallel to the shock. While the magnetic fields parallel to the relativistic shock decrease as $B'_{\parallel} \propto r^{-2}$, as we obtain from Eq. (3.6), the ones perpendicular to the relativistic shock front are assumed to change with $B'_{\perp} \propto r^{-1}$, see Ref. [164]. However, we are not discussing the plasma physics effects at this stage, but should be incorporated in the future similar to the expansion approach presented in Ref. [165]. We are, however, assuming that the adiabatic index is $\hat{\gamma} = 4/3$, and that the result calculated at R_c is valid even when considering expansion.

When we now want to calculate the amount of escaping particles from a GRB based on different parameter sets, we need to define the direct component in a way that matches the quantities used in the NeuCosmA code. Therefore, we need to define a proton “injection” spectrum $Q'_{p,\text{direct}}$ for the direct escaping protons. Using an effective approach, we can use the steady state spectrum N'_p together with the dynamical time-scale of particle escape t'_{dyn} and the fraction of escaping particles, see Eq. (3.4), giving

$$Q'_{p,\text{direct}} = \frac{N'_p}{t'_{\text{dyn}}} \cdot f_{\text{esc}} = \frac{N'_p}{t'_{\text{eff,dir}}} \quad , \quad (3.8)$$

with the effective direct escape rate $t'_{\text{eff,dir}} \equiv t'_{\text{dyn}}^{-1} \cdot f_{\text{esc}}$. This new CR component can be added to our standard GRB neutrino code to directly calculate all the different contributions to CR escape in one run.

We compute the spectra for four example bursts with a set of “standard” parameter values from Table 1.1, with only the luminosity being changed among the four examples. We assume that all stable particles including the CR protons are only subject to the losses due to the cosmic expansion. The losses due to interactions with the photons of the CMB or CIB will only be discussed in chapter 4. We also set the acceleration efficiency to $\eta = 1$. As we will see later, a high acceleration efficiency η is needed for acceleration to high enough energies. The luminosity range we are interested in is $L_{\gamma,\text{iso}} = 10^{50}\text{--}10^{53} \text{ erg s}^{-1}$. These values are in the range of the luminosities observed for real bursts. Based on these parameters, we individually calculate the proton as well as photon density at our collision site, and then the cosmic ray and neutrino spectra with the help of our interaction code.

In the upper row of Fig. 3.1, we depict the resulting spectra as expected to escape from a single shell. The shown spectra are in the observer’s frame, when assuming only the adiabatic losses due to the cosmic expansion apply, see Appendix B. The input proton density (thin dashed curve), the escaping neutrons (solid blue curve), the (new) direct escape component (solid green curve, defined in Eq. (3.8)), and the muon neutrino (and antineutrino) spectrum (thin orange curve) are shown. The left column represents the results for $L_{\gamma,\text{iso}} = 10^{50} \text{ erg s}^{-1}$, while the right one is for $10^{51} \text{ erg s}^{-1}$. As can be seen from the denoted values of the optical depth to neutron escape τ_n , see Eq. (3.1), both of these examples are optically thin ($\tau_n < 1$). Moreover, the direct escape component dominates at the highest energies in both

of the depicted cases. In regard of the highest energies, the energy $E_{p,\max}$ (in the observer's frame), depicted through the vertical black line, is of special interest. This maximal proton energy is derived by comparing the different proton loss rates t'_{loss}^{-1} (in SRF) to the acceleration rate, see lower row of Fig. 3.1. Here, the dynamical escape rate t'_{dyn}^{-1} is the dominating loss rate, and as a consequence the direct escaping protons dominate at the highest energies. However, an important change from $L_{\gamma,\text{iso}} = 10^{50} \text{ erg s}^{-1}$ to $10^{51} \text{ erg s}^{-1}$ is that the photohadronic interaction rate increases compared to the other loss rates. Therefore, the neutron component is enhanced due to the higher amount of photohadronic interactions.

When we increase the luminosity even further, this leads to an even stronger photohadronic interaction rate. For $L_{\gamma,\text{iso}} = 10^{52} \text{ erg s}^{-1}$, the direct escape component no longer surpasses the neutron component, even at $E_{p,\max}$, see left column of Fig. 3.2. The photohadronic interaction rate in this example is already so high that it limits $E_{p,\max}$. Even though the synchrotron loss rate dominates at energies much larger than $E_{p,\max}$, the photohadronic interaction rate is still the loss rate which initially counters the acceleration. As a consequence, we already obtain values for τ_n which are larger than one, *i.e.* $\tau_n = 3.37$. Moreover, even though we increase the luminosity of the burst, the value of $E_{p,\max}$ no longer grows at this point. While it grows (with some power of) the luminosity in the optically thin range, it actually starts to shrink again in the optically thick regime. Compared to the value of $E_{p,\max}(L_{\gamma,\text{iso}} = 10^{51} \text{ erg s}^{-1})$, the one for $L_{\gamma,\text{iso}} = 10^{52} \text{ erg s}^{-1}$ is slightly lower. And finally, for the highest assumed value $L_{\gamma,\text{iso}} = 10^{53} \text{ erg s}^{-1}$, the direct component is only subdominant over the whole energy range. The dynamical loss rate is always lower than the other loss rates, and, consequently, direct escape does not play an important role. Also, the optical thickness $\tau_n = 35.6$ is now much larger than one, which also leads to an increase of the neutrino emission (thin solid orange curve) compared to the cosmic ray emission (here: thick solid blue curve). The maximal achievable energy $E_{p,\max}$ is further decreased, since the photohadronic interaction rate increases faster than the growth of the acceleration rate. In summary, it can clearly be seen that the results for CR and neutrino escape from a GRB depend strongly on the parameters. It is possible to either enhance the amount of CR compared to the amount of prompt neutrinos (direct escape dominated scenario, see left column of Fig. 3.1), or to have significantly more prompt neutrinos from a burst compared to the CR (optically thick neutron escape scenario, see Fig. 3.2). The standard case of optically thin neutron escape is limited to a range between the two aforementioned cases. However, these results discussed in the previous paragraphs are all for an acceleration efficiency $\eta = 1.0$. As soon as η is assumed to be lower, *e.g.* $\eta = 0.1$, the amount of direct escaping particles is significantly reduced. Moreover, the values for $E_{p,\max}$ are also lower. This is mainly due to the effect η has on t'_{acc}^{-1} , see Eq. (2.29). Instead of obtaining the maximal energy in one cycle, the particles now need to run through η^{-1} cycles to gain the maximal energy. The acceleration length is therefore larger by about the same factor of η^{-1} . Since the size of the region is not changed, and we have assumed that particles can escape after one cycle, only a fraction of about η of all particles are able to directly escape from the source. Put simply, the mean free path for direct escape is smaller than the acceleration scale, and only a fraction of the accelerated particles can escape.

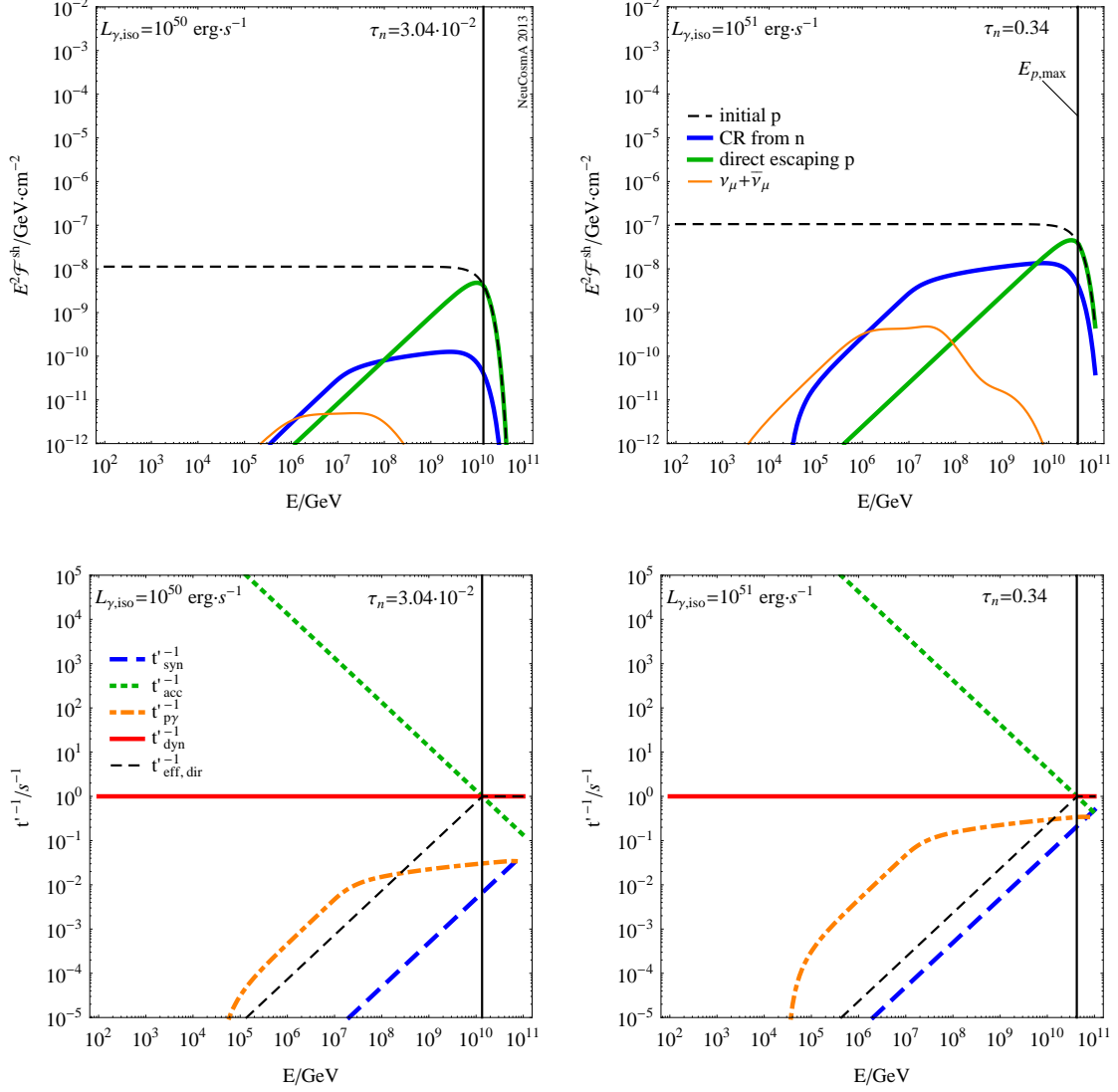


Figure 3.1.: These plots show the results of the calculations for the emission from a single shell, taken from Ref. [152]. The upper row shows the predicted particle spectra in the observer's frame. The thin dashed curve represents the initial proton spectrum, if all protons could escape. The actually escaping components are depicted by the blue curve in case of CR escape via neutrons and by the green curve for direct escaping protons. Additionally, the muon neutrinos are depicted as a thin orange curve. The lower row depicts the different rates associated with the sets of parameters. The acceleration rate (green dotted curve) needs to be compared to the different loss rates (see legend inside lower left plot). In case of $t'_{p\gamma}^{-1}$, the interaction rate is shown, not the somewhat lower photohadronic loss rate. Each column is one set of parameters with only the luminosity $L_{\gamma, \text{iso}}$ changed.

Nonetheless, to fully understand the effect of the different parameters on the results, parameter scans are needed. For this reason, we will do these scans to identify the regions in which the CR escape is dominated by which escape mechanism.

3.3. Identifying different CR escape regimes

As we have stated earlier, the dominating contribution to the cosmic rays at the highest energies is a result of the burst parameters. In the internal shock model that we are using, parameters such as the Lorentz factor Γ or the variability time scale t_v have a significant effect on the result of the simulations. Additionally, the assumed redshift z also changes the result, when the parameters are assumed to be fixed in observer's frame. In Ref. [152], we only discussed these three parameters apart from the luminosity $L_{\gamma,\text{iso}}$. In the work presented here, we will additionally show the effect of the photon break energy $\varepsilon'_{\gamma,b}$. As we have detailed in the previous section, there are three possibilities of how the UHECR could escape from the source in our discussed model, with the descriptions taken from our Ref. [152]:

Optically thin to neutron escape regime This is the usual scenario discussed in the literature: the cosmic rays are produced as neutrons and can escape the source (“neutron model”). Additional escape components are negligible, and the “one (muon) neutrino per cosmic ray” paradigm applies. Note that the optical thickness in our calculations includes the high-energy processes leading to multiple pions instead of just the Δ -resonance.

Optically thick to neutron escape regime Here the protons and neutrons interact multiple times, and only protons and neutrons on the outer edges of the shell can (directly) escape. The neutrinos, however, can escape from everywhere within the shell, which leads to more neutrinos per cosmic ray than in the optically thin case. See Sec. 3.1.

Direct escape regime Here, the cosmic rays from direct escape dominate at least at the highest energy. Since the neutron production by photohadronic processes is sub-dominant, the one neutrino per cosmic ray relationship does not hold, and more cosmic rays than neutrinos will be produced. See Sec. 3.2.

When we now want to quantify a point in the parameter space, and characterize it based on the associated emission, we need a point-of-reference. We do this by comparing if the maximal fluence in $E^2\mathcal{F}$ comes from direct escape or from neutron escape. When this test shows that the maximal fluence does come from direct escape, we assign this point to the direct escape regime. In case the neutron escape dominates, we need the additional test of the optical thickness, as defined in Eq. (3.1). We will use the $\tau_n = 1$ to discriminate between optically thin and thick, even though smaller values might already be sufficient to hinder the escape, as discussed in Ref. [163]. This discrimination is already sufficient to ensure a unique classification of each point in the parameter space (neglecting minor overlaps), see Figs. 3.3 and 3.4.

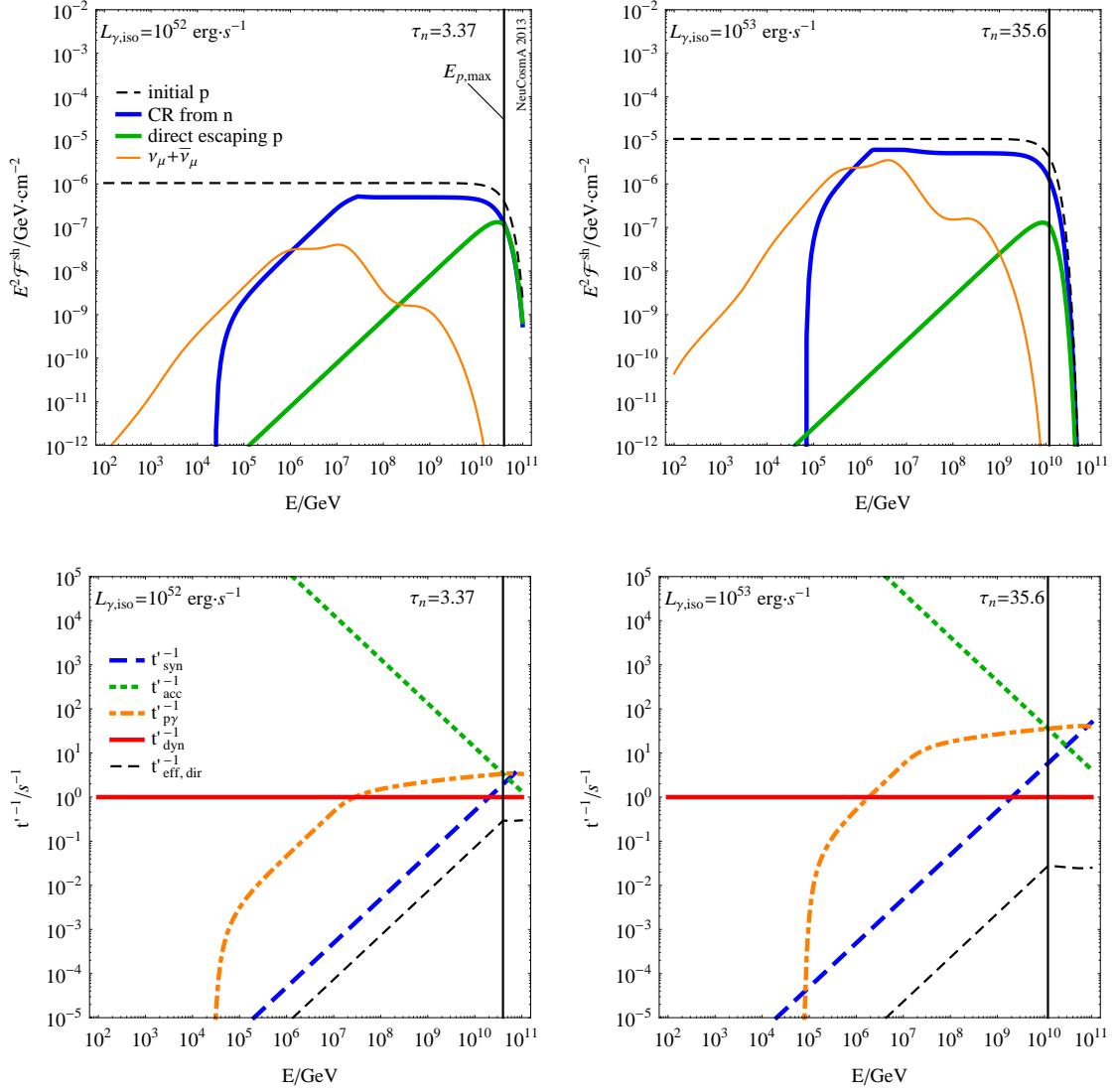


Figure 3.2.: The particle spectra as function of particle energy (upper row) and the relevant rates (lower row) for $L_{\gamma,\text{iso}} = 10^{52} \text{ erg s}^{-1}$ (left column) and $10^{53} \text{ erg s}^{-1}$ (right column), similar to Fig. 3.1, also taken from Ref. [152]. The assumed values of $L_{\gamma,\text{iso}}$ are now so high that the neutrons (blue curves in upper plots) at $E_{p,\text{max}}$ (thin vertical line) are more likely to interact with the photon field than escape from the shell. As can be seen from the lower plots, the photohadronic interaction rate (orange dash-dotted curve) is above the dynamical escape rate (solid red curve) at $E_{p,\text{max}}$. Hence, these examples are considered to be optically thick; $\tau_n > 1$. Moreover, the direct proton escape component (green curves in upper plots) is only subdominant while the neutrinos (thin orange curves in upper plots) are enhanced compared to the CR components.

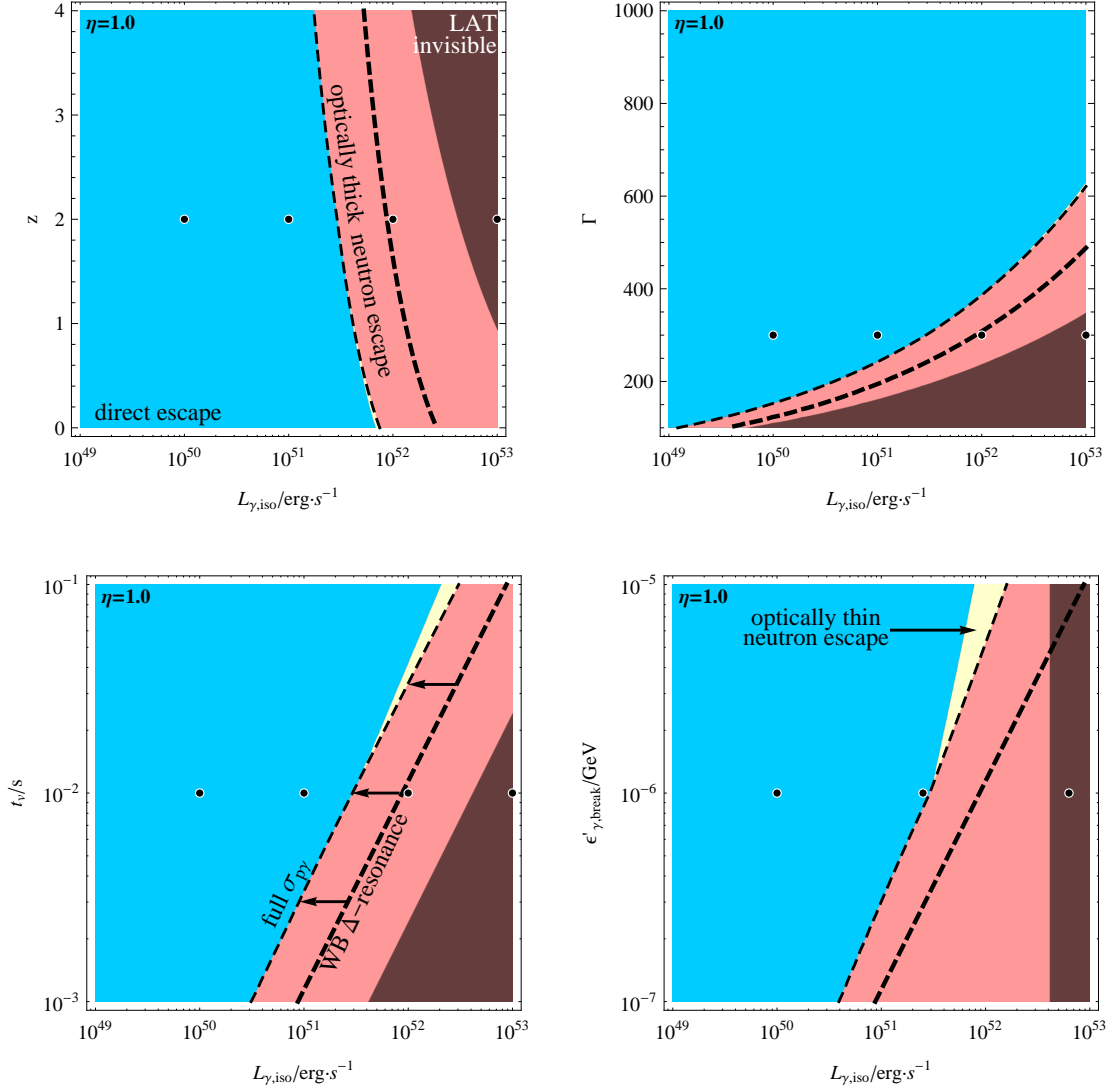


Figure 3.3.: Parameter scans over 2D planes of the parameter space. Here, the different regimes of CR escape (for definitions see text) are color-coded as follows: the direct escape regime is depicted blue, the standard optically thin neutron escape is depicted as yellow, while the optically thick neutron escape is depicted as red. The dashed curves represent the borders between the optically thin and thick regimes, with the thin curve representing the numerical result for the full photohadronic interaction cross section, and the thick curve being the analytical estimation when using the WB approximation of the interaction rate [122]. The black points represent the four example bursts from the previous section. Moreover, the dark-shaded region is the “LAT invisible” range, in which gamma-rays of 30 MeV or more can no longer escape from the source, based on the pair-creation cutoff. The plots are an extended version of the ones from Ref. [152].

In the parameter scans depicted in Figs. 3.3 and 3.4, we always vary two of the different principal parameters of a burst, with the luminosity $L_{\gamma,\text{iso}}$ always being on the horizontal axis. When we now take a closer look at the scans with $\eta = 1.0$ (efficient acceleration), which are depicted in Fig. 3.3, there is the surprising observation that the optically thin neutron escape regime (yellow shaded region) is only applicable to a very limited range in the parameter space. As in the example plots in Figs. 3.1 and 3.2, we either have the case that the direct escape component dominates at $E_{p,\text{max}}$ (direct escape regime, blue shaded region), or the photon density is so high that the optical thickness for neutron escape is already $\tau_n > 1$ (optically thick neutron escape, red shaded region). This vanishing of the standard optically thin neutron escape is a consequence of the high acceleration efficiency. As mentioned before, for this value of η all protons can either escape at the highest energy, or the photon density is already so high that the source is optically thick. Only when we lower η , it is possible to have a larger region in which not all protons directly escape and, also, the photohadronic interaction does not limit the escape of neutrons significantly. This can be seen in our scans with moderate acceleration efficiency ($\eta = 0.1$), see Fig. 3.4. Here, the standard optically thin neutron escape regime is a clearly visible region around the aforementioned standard parameters of GRBs, such as $L_{\gamma,\text{iso}} = 10^{51} \text{ erg s}^{-1}$ and $\Gamma = 300$. As can be expected by the lower amount of direct escaping protons at the highest energies, this growth of the optically thin neutron escape regime comes mainly at the cost of the direct escape regime, compare scans in Fig. 3.4 to those in Figs. 3.3. Still, it can clearly be seen that the standard assumption of one neutrino per cosmic ray only applies to a limited range of the parameter space. Depending on the acceleration efficiency η , this region can actually grow for smaller values of η , however, this comes at the cost of lower maximal proton energies $E_{p,\text{max}}$.

To better understand how the different regimes depend on the used parameters, we now want to give a sketch how to derive the contours using analytical estimates. This also allows us to better compare our current work to earlier works in the literature. Especially, for the calculation of the border between the optically thin and optically thick regime, we can use the Δ -resonance approximation from Ref. [122] to estimate the photohadronic interaction rate, see Eq. (3) of said reference.² By plugging this into Eq. (3.1) (and setting $\tau_n \equiv 1$), we can obtain an estimate for the transition. The analytical term of the border to the optically thick regime is

$$L_{\gamma,\text{iso}}^{\text{opt. thick}} \lesssim 1.1 \cdot 10^{52} \text{ erg s}^{-1} \cdot \left(\frac{\Gamma}{10^{2.5}} \right)^5 \cdot \left(\frac{t_v}{0.01 \text{ s}} \right) \cdot \left(\frac{1+z}{3} \right)^{-1} \cdot \left(\frac{\varepsilon'_{\gamma,\text{break}}}{1 \text{ keV}} \right) . \quad (3.9)$$

For comparison reasons, this formula above is depicted as the thick dashed curve in the scans of Figs. 3.3 and 3.4. As always with approximations, these formulas only have a limited applicability. The visible difference between the numerical result (thin dashed curve) and the analytical estimate is due to the additional contributions to the interaction cross section, that are used in the numerical calculation. Still, the principle strong dependence of the border on Γ can be mainly traced back

²Note, however, that the rate from said reference needs to be increased by a factor of two, since we need to use the full interaction rate and not just the pion production rate.

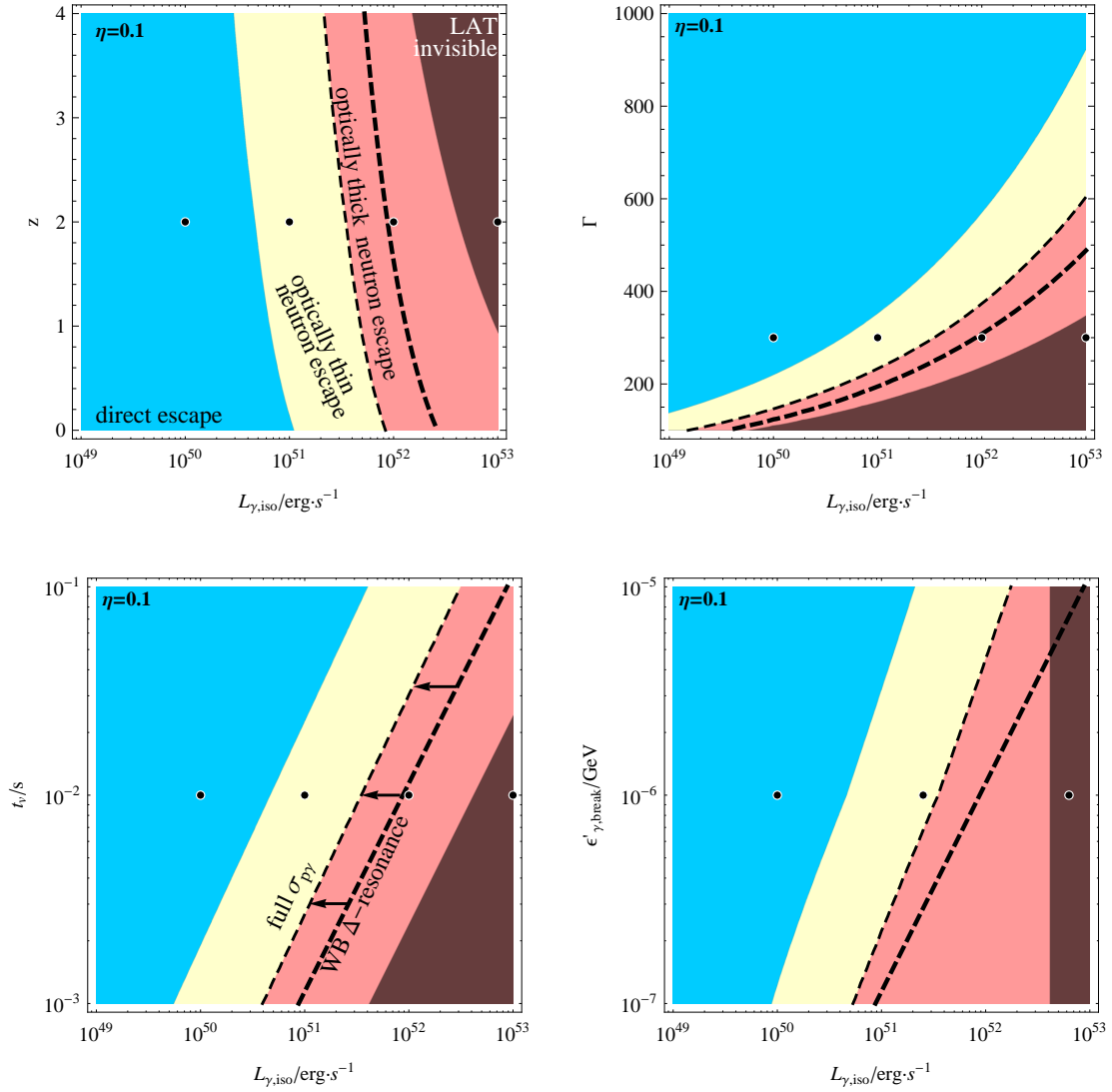


Figure 3.4.: These scans are the same as in Fig. 3.3, however with a moderate acceleration efficiency of $\eta = 0.1$. The most striking difference to the result with $\eta = 1.0$ is the clearly visible region of optically thin neutron escape (yellow shaded region). This region is now found around the standard values for GRBs, such as $L_{\gamma, \text{iso}} = 10^{51} \text{ erg s}^{-1}$ and $\Gamma = 300$. While the optically thick neutron escape region (red shaded region) is nearly unchanged by the lower acceleration efficiency, the direct escape regime (blue shaded region) is significantly reduced compared to the scans in Fig. 3.3. The scans shown here are an extended version of the ones from Ref. [152].

to the Γ -dependence of the volume, see Eq. (2.23). Since the volume affects the photon density which in turn specifies the photohadronic interaction rate, the strong Γ -dependence is inherited by each subsequent calculation. The reasoning for the dependence on z is essentially the same as most observed quantities always need to be corrected for the cosmic expansion, even though the resulting dependence is a bit weaker than for Γ (as in the definition of the volume). The proportionality to $\varepsilon'_{\gamma,\text{break}}$ is also inherited from the photon density. On the other hand, the dependence from the variability time t_v is due to the combination of the total volume (from $t'_{p\gamma}{}^{-1}$) being divided by the size of the shell (from $t'_{\text{dyn}}{}^{-1}$).

Moreover, we can obtain the interface between the direct escape and the (optically thin) neutron escape regime by comparing the maximal proton energy for the two different limiting scenarios. When the dynamical timescale is dominant, then all protons can escape at the highest energies (for $\eta = 1$) and we are in the direct escape regime. If the escape is limited by the synchrotron losses, then neutron escape will be the dominant escape mechanism. By considering these two types of losses for the calculation of the maximal proton energy, and correctly including η , one obtains

$$L_{\gamma,\text{iso}}^{\text{direct}} \lesssim 3.6 \cdot 10^{51} \text{ erg s}^{-1} \cdot \eta^{\frac{2}{3}} \cdot \left(\frac{\Gamma}{10^{2.5}} \right)^{\frac{14}{3}} \cdot \left(\frac{t_v}{0.01 \text{ s}} \right)^{\frac{2}{3}} \cdot \left(\frac{1+z}{3} \right)^{-\frac{2}{3}} \cdot \left(\frac{\epsilon_B}{\epsilon_e} \right)^{-1} \quad (3.10)$$

as the border of the direct escape regime. As can be seen from the deviation inside the $L_{\gamma,\text{iso}}\text{-}\varepsilon'_{\gamma,\text{break}}$ -scan from the (in-)dependence from $\varepsilon'_{\gamma,\text{break}}$ suggested by the above formula, this simple approach leading to Eq. (3.10) is not sufficient to describe all parameter dependencies of the border. However, it is a good “zeroth order” estimate for the parameter dependencies in a multi-dimensional parameter space, despite its obvious shortcomings. The parameter dependencies for this border are a bit less intuitive as they are obtained from the analytical formulas for synchrotron loss limited and for adiabatic loss limited maximal proton energy. Those energies mainly depend on the magnetic field B' which in turn also depends on the energy density, see Eq. (2.25). Hence, one again has the strong dependence on Γ and a somewhat weaker dependence on z . The other proportionalities are as well mainly derived from the calculation of the energy densities. Moreover, the acceleration efficiency η affects the time needed to reach the maximal energy. Hence, a lower value of η makes it more likely that the protons are limited by synchrotron losses, as can be seen by the shift of the border of the direct escape region to lower luminosities when comparing Fig. 3.3 to Fig. 3.4.

A further plausibility check for our scans is to make sure that the bursts are actually visible in a certain photon energy for the parameters we choose. One example would be to check if a burst is visible in the *Fermi*-LAT energy range. As described in Appendix C, it is possible to calculate the region in which photons of 30 MeV or more can no longer escape the source due to the pair creation threshold. These regions are the dark-shaded “LAT invisible” areas in Figs. 3.3 and 3.4. As the name states, there should not be any detectable emission in the LAT energy range from bursts within the dark-shaded region, while outside of it a detection in the whole GBM range as well as even some events in LAT may be possible. Therefore,

the fourth example burst (the one with the highest optical thickness) should not be visible in the LAT, as the dot representing this burst is already in the shaded region (dot on the furthest right in Figs. 3.3 and 3.4). As we discussed in Ref. [152], τ_n (for neutrons) and $\tau_{\gamma\gamma}$ (for photons) do not follow the exact same parameter scaling. Note, however, that the actual photon emission at the LAT energies may come from a different radius than the lower emission components, see, *e.g.*, Ref. [166]. As we mentioned earlier, this may be due to the evolution of the optical thickness of the burst plasma. As a result, a burst would have a certain trajectory through the parameter space instead of just one point. This issue can be addressed in the future by the assumption of different shells and modeling the collisions of these shells individually to obtain the real burst spectrum.

An additional aspect of the scan we have so far not discussed is the possibility to also obtain the maximal proton energy $\tilde{E}_{p,\max}$ in the source frame (cosmologically comoving frame). Before we discuss the CR propagation with all its losses in chapter 4, we first need to know if it is even possible to obtain the needed energies with our GRB model. For this, we need the aforementioned maximal proton energy, however boosted to the source frame after calculating it in the SRF. This can easily be done during our scans and we show $\log_{10}(\tilde{E}_{p,\max}/\text{GeV})$ as an additional set of contours on top of the regimes we previously discussed in Fig. 3.5. As can be seen from said figure, the regimes discussed in Fig. 3.3 also affect the maximal proton energy. Especially, the transition from the optically thin to the optically thick regime, depicted as a solid red curve in Fig. 3.5, functions as a kind of symmetry axis for the behavior of $\tilde{E}_{p,\max}$ in the parameter space. This is due to the change of the maximal proton energy being limited by the photohadronic losses or one of the other mechanisms (dynamical losses or synchrotron losses). The highest energies can actually be obtained along this curve. The actual values of $\tilde{E}_{p,\max}$ which can be obtained highly depend on η . While for $\eta = 1$, as depicted in Fig. 3.5, energies above 10^{11} GeV are possible, a change to $\eta = 0.1$ also reduces the maximal energies by about one order of magnitude, see Fig. 3.6. Another aspect, which needs to be considered, is the mean free path of a CR proton while traveling through space. The interactions with the cosmic microwave background (CMB) as well as the cosmic infrared background (CIB) limit the distance a UHECR can travel, see Sec. 4.1. Due to these, a UHECR with $\tilde{E} \simeq 10^{10}$ GeV can only travel about 1 Gpc ($z \simeq 0.25$) without interacting, while at $\tilde{E} \simeq 10^{11}$ GeV this range is reduced to 100 Mpc ($z \simeq 0.024$). This clearly limits the range in redshift from where the GRBs can originate to give rise to the observed UHECR. Moreover, this limits the parameter space region which can produce UHECR to a certain range. For $\eta = 1$, as can be seen in the upper left plot of Fig. 3.5, all bursts within the depicted range of $L_{\gamma,\text{iso}}$ can lead to values of $\tilde{E}_{p,\max} \geq 10^{10}$ GeV. However, bursts with the potential to accelerate to $\tilde{E}_{p,\max} \geq 10^{11}$ GeV can only be found in the range $6 \cdot 10^{50} \text{ erg s}^{-1} \lesssim L_{\gamma,\text{iso}} \lesssim 10^{53} \text{ erg s}^{-1}$. In case of a more moderate acceleration efficiency, such as $\eta = 0.1$ depicted in Fig. 3.6, these high energies are difficult to reach (or in the shown case, not possible at all). Even energies of $\tilde{E}_{p,\max} \geq 10^{10}$ GeV can only be found between $L_{\gamma,\text{iso}} \simeq 6 \cdot 10^{50} \text{ erg s}^{-1}$ and $10^{53} \text{ erg s}^{-1}$. Hence, as we also discuss in Ref. [152], it is unlikely that GRB are the sources of UHECR when assum-

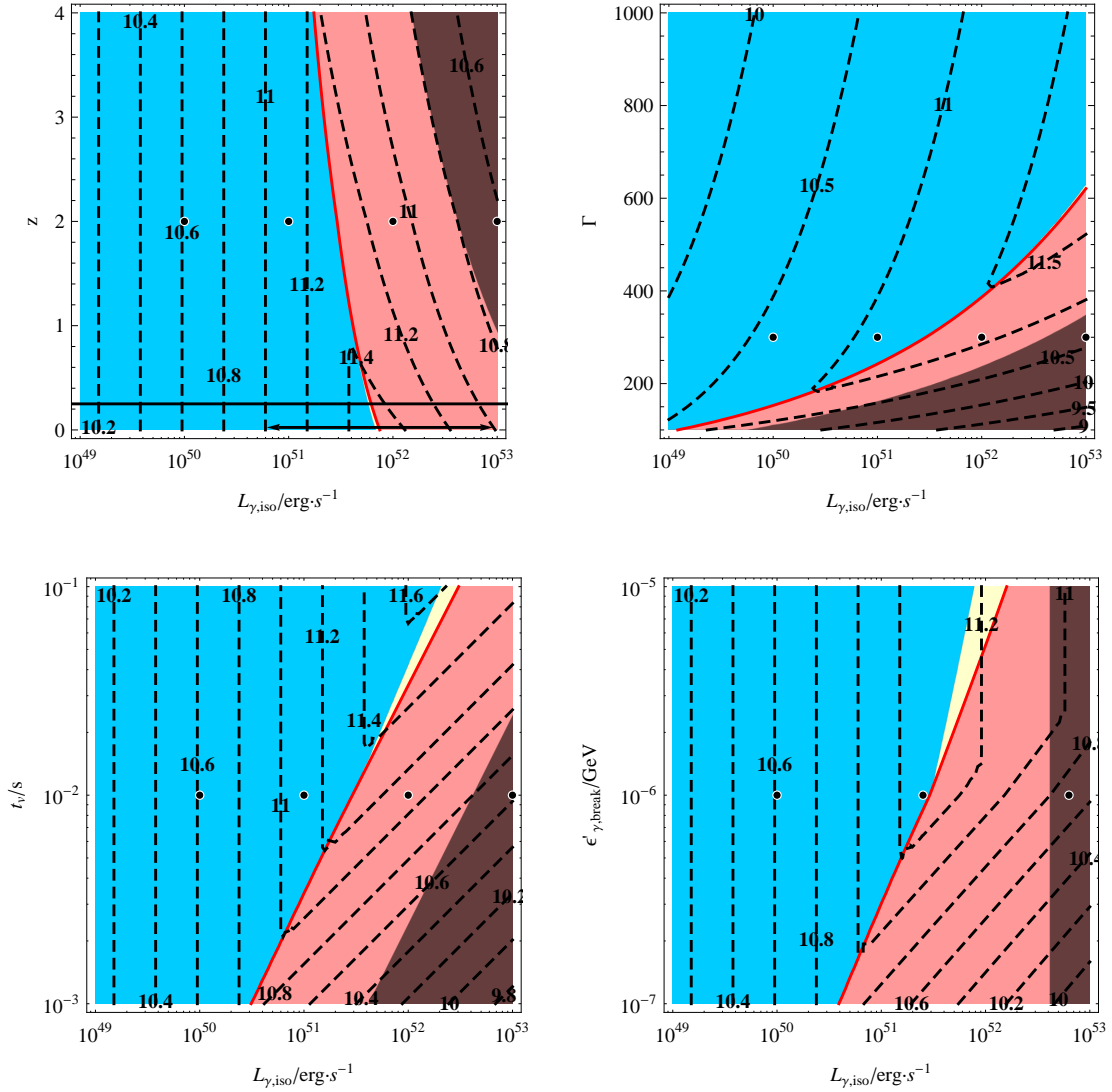


Figure 3.5.: Depicted here are the same scans as in Fig. 3.3 ($\eta = 1$), however now with the additional contours for the maximal proton energy in the source frame (cosmologically comoving frame), given as $\log_{10}(\tilde{E}_{p,max}/\text{GeV})$. As can be seen from the labels of the black dashed contours, the maximal energy for this η reaches more than 10^{11} GeV, which is near the maximal observed energy in cosmic rays. Moreover, the maximal possible energies seem to be symmetric towards the border of optically thin and thick regimes (red solid curve). As an additional feature, we have included the mean free path of protons with certain energies into the scan over z . For $\tilde{E} \simeq 10^{10}$ GeV, it is of the order of 1 Gpc ($z \simeq 0.25$), while for $\tilde{E} \simeq 10^{11}$ GeV it is about 100 Mpc ($z \simeq 0.024$). Based on plots from Ref. [152].

ing standard parameters. The acceleration efficiency must either be high, or only very few bursts contribute significantly at the highest energies. Moreover, this whole discussion is based on assuming that all but two parameters are fixed to standard values in the observer’s frame. This too affects the results. As real bursts might not be located on the exact planes shown in the scans so far, we will now turn to actually observed bursts to test our model.

3.4. Application to specific GRBs

After having discussed how the cosmic rays escape from a single GRB would look like in the parameter space when assuming fixed parameters in the observer’s frame, we now want to test how the model applies to real bursts. For this, we need the actually observed parameters, such as the fluence/flux, the redshift, the variability timescale, and the duration, of specific bursts to correctly calculate the neutrino flux prediction. While we used the luminosity $L_{\gamma,\text{iso}}$ in the previous section as one of the basic parameters, we will now have to derive it using the parameters and Eq. (B.12). The parameters for the four bursts, we want to discuss in the light of cosmic ray escape from a single source, can be found in Table 3.1. Note that we again use the simplification that even these observed bursts consist of $N = T_{90}/t_v$ identical shells/collisions, as has been used in Refs. [134, 135, 136].

The four bursts we picked for this small sample have been chosen for various reasons. The (standard) burst “SB” has the specific parameters to numerically reproduce the WB GRB neutrino flux shape and normalization from Refs. [122, 123]. This is actually only a theoretical burst, while the other three burst have been observed by various satellites. GRB080916C is one of the most luminous bursts ever recorded. Its high redshift as well as its detection well into the *Fermi*-LAT range make it one of the best studied and most energetic events known; especially, note the recent result of data re-analysis in Ref. [55]. GRB090902B has a peculiarly steep drop in the photon spectrum, while still having a quite high Lorentz factor Γ (from a single zone model). Due to these features, this *Fermi*-LAT burst is actually considered a prime candidate for photospheric emission, see Refs. [167, 168]. We will nonetheless use the internal shock model for the calculations. The last burst, GRB091024, can be regarded a typical example of a *Fermi*-GBM burst, based on the catalog compiled in Ref. [169]. The discussion of these bursts is based on Ref. [152].

The resulting cosmic ray and neutrino spectra can be seen in Fig. 3.7, which are calculated based on the parameters given in Table 3.1. As for previous figures, blue curves represent the CR component from neutron escape, green curves the component from direct escaping protons while the thin orange curves depict the muon neutrinos. Also, the initial proton component is once again depicted as a thin dashed curve. Note that we use the more realistic mild acceleration efficiency $\eta = 0.1$ for these calculations. As discussed before, this leads to lower maximal proton energies as well as less efficient direct proton escape. Hence, with a higher acceleration efficiency the direct escape component would be even more pronounced. Apart from the different particle spectra we also include the optical thickness for

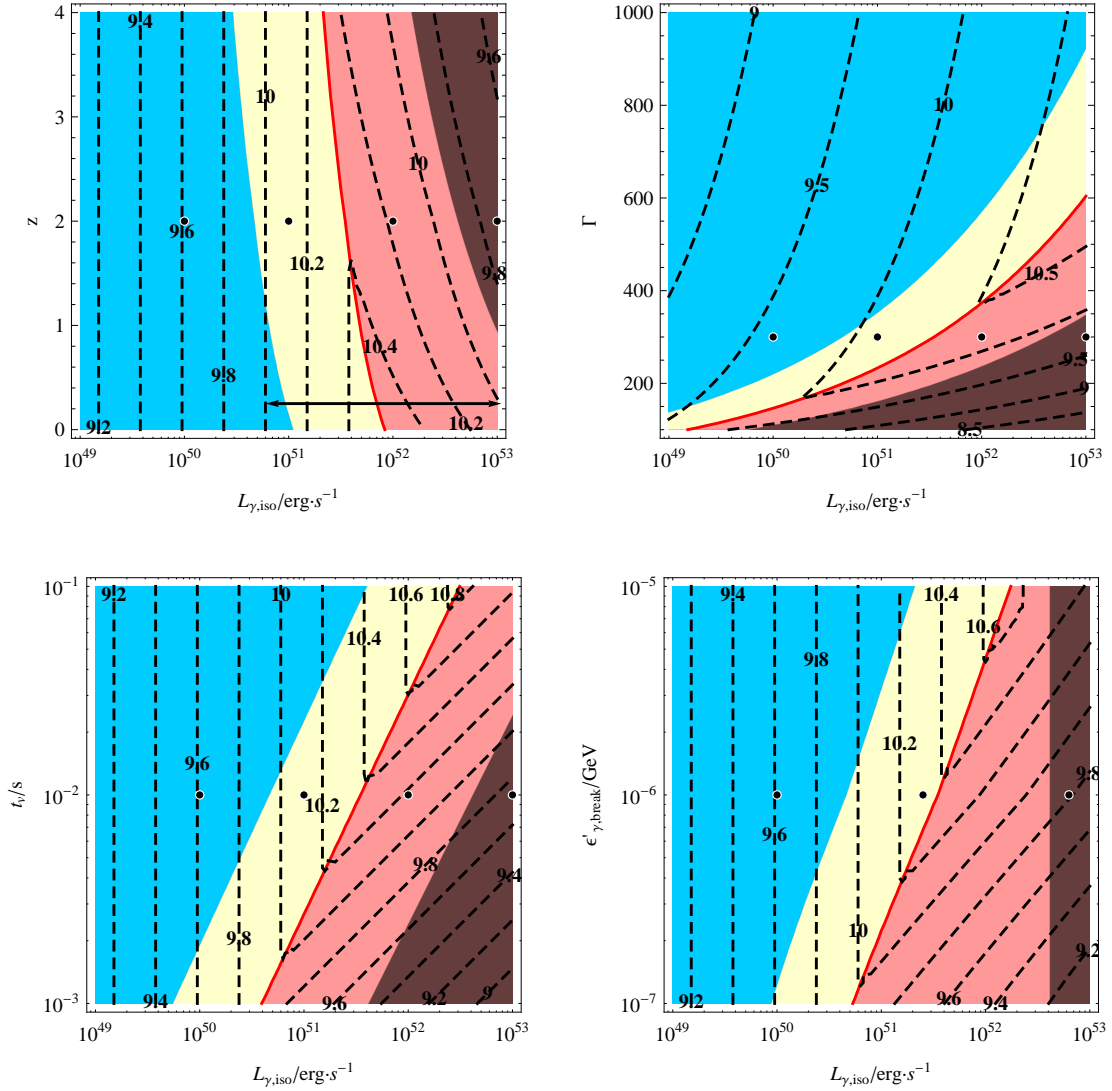


Figure 3.6.: The scans show the maximal proton energy $\log_{10}(\tilde{E}_{p,\max}/\text{GeV})$ (in the source frame) as contours overlaid on to of the regimes from Fig. 3.4. Here, the assumed acceleration efficiency only has a moderate value, $\eta = 0.1$. Due to this, the resulting values for the maximal energy are somewhat smaller than for the efficient acceleration case from Fig. 3.5. Still, even when changing η , the border between the optically thin and the optically thick regime (solid red curve) functions as a divider between different parameter dependencies of $\tilde{E}_{p,\max}$. Based on plots from Ref. [152].

	SB	GRB080916C	GRB090902B	GRB091024
α_γ	1	0.91	0.61	1.01
β_γ	2	2.08	3.80	2.17
$\epsilon_{\gamma,\text{break}}$ [MeV]	1.556	0.167	0.613	0.081
Γ	$10^{2.5}$	1090	1000	195
t_v [s]	0.0045	0.1	0.053	0.032
T_{90} [s]	30	66	22	196
z	2	4.35	1.822	1.09
$\mathcal{F}_{\gamma,\text{bol}}$ [erg cm $^{-2}$]	$1 \cdot 10^{-5}$	$1.6 \cdot 10^{-4}$	$3.3 \cdot 10^{-4}$	$5.1 \cdot 10^{-5}$
$L_{\gamma,\text{iso}}$ [erg s $^{-1}$]	10^{52}	$4.9 \cdot 10^{53}$	$3.6 \cdot 10^{53}$	$1.7 \cdot 10^{51}$

Table 3.1.: The properties of the four real GRB which we will use for our discussion. The “Standard Burst” (SB) is taken from Ref. [82] (similar to analytical prediction from Refs. [122, 123]). Parameters for the very energetic GRB080916C are taken from Refs. [169, 170], the ones for the candidate for photospheric emission, GRB090902B, are from Refs. [169, 171], and the typical *Fermi*-GBM burst GRB091024 is based on Refs. [169, 172]. The luminosity is calculated with $L_{\gamma,\text{iso}} = 4\pi d_L^2 \cdot \mathcal{F}_{\gamma,\text{bol}}/T_{90}$, with $\mathcal{F}_{\gamma,\text{bol}}$ the fluence in the (bolometrically adjusted) energy range 1 keV–10 MeV. Adopted from Ref. [173].

neutron escape τ_n as well as the optical thickness for photon escape $\tau_{\gamma\gamma}$ with an observed energy of 30 MeV. The burst SB, which was chosen to reproduce the standard WB GRB neutrino flux, is a typical example for a burst with optically thin neutron escape. The basic relationship of one neutrino per cosmic ray holds for this burst, and we also have a significant amount of prompt neutrinos. The direct escape component is suppressed, due to the value of the acceleration efficiency. The two *Fermi*-LAT bursts GRB080916C and GRB090902B, however, show a distinct direct escape component which dominates at the highest energies. Based on the parameter scans we did in Sec. 3.3, it is clear that this is a consequence of the high values of Γ (both $\Gamma \geq 1000$), compare to Fig. 3.4. It is obvious that these LAT bursts need to be left of the dark-shaded (LAT invisible) region. A higher choice for the detected photon energy ($\epsilon_\gamma > 30$ MeV) will move the exclusion region further to the left, till only the direct escape regime is still viable. Hence, bursts which emit in the LAT range favor the direct emission of UHECR — at least during the phase during which they emit the high-energy gamma-rays. Our typical *Fermi*-GBM is, however, again more like the SB, as can be seen be the lower right panel of Fig. 3.7. Even though it is already on the edge to the optically thick regime, it still is dominated by neutron escape and the neutrino production is given by the standard assumption.

As an additional feature of the photon spectrum from Eq. (2.2), which we so far have not discussed, we also include the effect of the minimal and the maximal photon energy, $\epsilon'_{\gamma,\text{min}}$ and $\epsilon'_{\gamma,\text{max}}$, respectively, to these plots. Since the values for the observed fluence $\mathcal{F}_{\gamma,\text{bol}}$ is only detected in (or in some cases adjusted to) the range from 1 keV to 10 MeV, we cannot exclude that the photon spectrum actually extends to higher or lower energies. These missing photons could either not have been detected, or could have not left the source at all. If we now assume that the observed spectrum can actually be extended by linear extrapolation, we obtain a “bolometric correction” to the previously calculated spectra, which we depict as (color-coded) shaded regions in Fig. 3.7. For the calculation of this bolometric correction, we first

normalize the photon spectra in the observed energy range based on the observed fluence. We then extend the spectrum by shifting the minimal and maximal photon energy to $\varepsilon'_{\gamma,\min} = 0.2 \text{ eV}$ (in SRF) and $\varepsilon_{\gamma,\max} = 100 \text{ MeV}$ (in the observer's frame). The former value is chosen to ensure that the high-energy protons have enough low energy photons to interact with, while the latter value is phenomenologically motivated to be a typical *Fermi*-LAT energy. In case of the correction, the normalization of the proton spectrum is then calculated on the extended photon spectrum (instead of only the observed range), using Eq. (2.28). As can be seen from Fig. 3.7, the bolometric correction always increases the normalization due to the additional photons now being taken into account, which can best be seen in the “initial protons”. Yet, the actual size of the increase depends on the burst parameters, with the upper spectral index β_γ being the most important one in this respect. In case of SB with $\beta_\gamma = 2$, the energy in photons is logarithmically dependent on the maximal photon energy. For values of $\beta_\gamma > 2$, the dependence is weaker and the effect of the bolometric correction is smaller. From the three other bursts GRB080916C gets the biggest correction due to $\beta_\gamma = 2.08 \approx 2$. Accordingly, if a burst had an upper index $\beta_\gamma < 2$, then the correction would gain even more importance. Moreover, extending the photon spectra to higher energies leads to a decrease of the threshold for photohadronic interactions, which can be seen as an extension of the neutron spectra to lower energies. This increase of the photohadronic interactions can, of course, also affect the maximal proton energy, as can be seen in the lower right panel of Fig. 3.7. This is the same effect as we have discussed for the optically thick examples in Fig. 3.2. As an additional test, we checked if the gamma-rays from π^0 -decays are consistent with current *Fermi*-LAT bounds and/or observations of this burst.

To summarize, the examples we discussed indicate that *Fermi*-LAT bursts should have a strong direct escape component. This component may not be dominant during the whole duration of the emission, however, while the highest energy gamma-rays escape from the source the direct component should be present as well. For a typical GBM burst, it is less likely that a direct escape component dominates, but this depends on the parameters, especially the acceleration efficiency η . Hence, conclusions on the claim that GRB are the sources of the UHECR can only be drawn from samples, and not from individual bursts. The evolution of a burst in time should also affect this, even though results on this are not part of this work. Moreover, detected bursts might be subject to a bolometric correction, since the energy range in which they are detected is only limited. Still, the effect of this correction is expected to be small as long as $\beta_\gamma \gtrsim 2$. In the following chapter, we now want to take a look at what is needed to really obtain the cosmic ray spectra at Earth based on a distribution of GRBs.

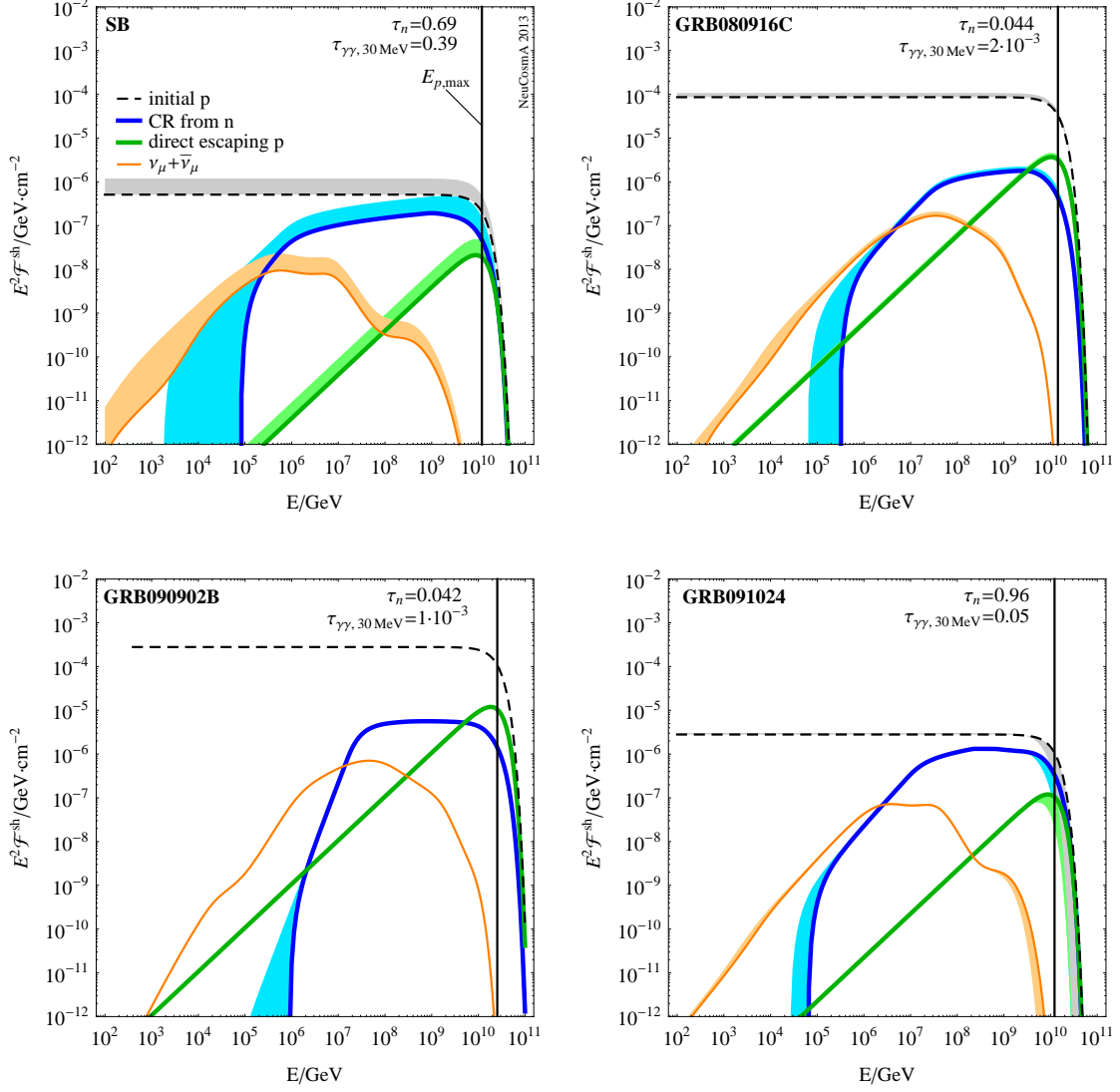


Figure 3.7.: The neutrino (solid orange curves) and cosmic ray spectra as a function of energy for the four bursts from Table 3.1. We again show the contributions to the cosmic rays via neutron escape (solid blue curves) as well as the direct escape components (solid green curves). As can be seen from the plots, the direct component actually dominates at $E_{p, \text{max}}$ (vertical line) for two of the four bursts, namely GRB080916C and GRB090902B. Also, the initial proton spectra are depicted as a thin dashed curves. The shaded areas depict the effect of extending the observed photon spectrum from the initial range of 1 keV – 10 MeV to $\varepsilon'_{\gamma, \text{min}} = 0.2$ eV (in SRF) and $\varepsilon_{\gamma, \text{max}} = 100$ MeV (in the observer’s frame). This can change the normalization of the initial protons (through the energy density), the threshold energy for photohadronic interactions (lower energy protons can interact), as well as also lower the maximal proton energy due to the increased photohadronic interactions.

4. Probing GRBs as the sources of UHECR

When comparing the predictions for UHECR from GRBs to current observational data, we need to take into account that CRs still interact during propagation. As discussed in the “GZK” papers, the cosmic ray protons can only travel a certain distance before interacting with cosmic background fields such as the cosmic microwave background (CMB), see Refs. [3, 4]. We will first discuss what types of interactions are considered to dominate during the propagation of CRs over large distances. We will compare these losses to the gains through injection of CRs from GRBs. Based on the GRB source model from the previous chapter, we will identify the different factors going into the calculation of the injection of CRs from GRBs. Using a simple CR propagation code, we will obtain a realistic UHECR prediction from a distribution of GRBs, which we normalize to current UHECR data, together with two neutrino flux components, the prompt GRB neutrinos and the cosmogenic neutrinos (from interactions during propagation). We will show how these three types of messengers — UHECR, prompt GRB neutrinos, and cosmogenic neutrinos — can be used to constrain models of GRBs as sources of UHECR.

4.1. A simple framework for CR injection and propagation

On cosmological scales, there are always losses due to the expansion of the universe, see Appendix B. Hence, these losses do also affect CRs on their journey from source to observer. Additionally, as was already discussed by Greisen [3], Zatsepin and Kuzmin [4], interactions with cosmic background photon fields, *i.e.* the CMB and, also, the cosmic infrared background (CIB), are an important source of losses during propagation for CRs. The CMB is considered to be totally isotropic and, in a way, defining the universe’s rest frame. In this frame, also the CIB is assumed to be isotropic. For the CMB photon spectrum, being a near perfect black-body spectrum (observed deviations are only $\mathcal{O}(10^{-5})$), the photon number density n_γ^{CMB} in $[\text{GeV}^{-1} \text{cm}^{-3}]$ is given by

$$n_\gamma^{\text{CMB}}(\epsilon, z = 0) = \frac{1}{\pi^2} \frac{1}{(\hbar c)^3} \frac{\epsilon^2}{\exp(\epsilon/(k_B T)) - 1} \quad . \quad (4.1)$$

Here ϵ is the photon energy, T the present-day CMB temperature ($T = 2.725 \text{ K}$; $k_B T \approx 0.23 \text{ meV}$), and the rest of the variables are natural constants, as found in Ref. [101]. From the scaling in z for energy and distances, see Appendix B, it is possible to derive that for the definition given in Eq. (4.1) the density needs to scale in z as

$$n_\gamma^{\text{CMB}}(\epsilon, z) = (1 + z)^2 n_\gamma^{\text{CMB}}(\epsilon/(1 + z), 0) \quad . \quad (4.2)$$

The second component for the background photon fields, the CIB, is modeled using the approach from Ref. [174]. While we can use simple scaling for the CMB, we assume that the CIB follows the SFR, hence needing an additional factor. The scaling of the CIB photon density is implemented as described in Appendix C of Ref. [162].

The presence of these background photon fields leads to photohadronic interactions, which have already been discussed in detail in Sec. 2.3. To obtain the photohadronic interaction rates, we will need the photon densities we previously defined. However, instead of using the usual interaction rates, such as $t_{p\gamma}^{-1}$ from Eq. (2.14), we will need energy loss rates $b = dE/dt$ in this chapter. In general, the energy loss rate due to some interactions b is given by

$$b(E, z) = -Et_{\text{loss}}^{-1}(E, z) \quad , \quad (4.3)$$

which is in the units $[\text{GeV s}^{-1}]$. The loss rate t_{loss}^{-1} is the product of the interaction rate and the fraction of energy lost per interaction, *e.g.* $t_{p\gamma}^{-1} \cdot \langle x_{p \rightarrow \pi} \rangle$. As a note on the notation: be aware that in case of the photon spectra discussed during CR propagation, the unprimed cosmologically comoving frame (what we called source frame for an individual GRB) is the frame in which the photon spectra are isotropic. Hence, here the calculations need to be done in this frame, as opposed to the calculations for individual GRBs, which are done in the primed rest frame of the shocks. Apart from the photohadronic interactions, also e^+e^- -pair creation processes can occur due to interactions with the two background photon fields. We will treat the processes of pair creation on nuclei, $A + \gamma \rightarrow A + e^+ + e^-$, as discussed in Refs. [175, 176].¹

Apart from these three types of losses, adiabatic losses, photohadronic losses, and losses due to e^+e^- -pair creation processes, we will not consider any other types of losses for our propagation approach. In case of synchrotron losses, this assumption is justified since synchrotron losses are only subleading compared to pair production and photohadronic losses, even in the UHECR range. This is a result of the current data on the intergalactic magnetic field, which indicates values below 10 nG, see, *e.g.*, Ref. [177]. For comparison reasons, we have plotted the pair production and the photohadronic loss times in the UHECR range due to the CMB (at $z = 0$) together with the synchrotron loss times for two different values for the intergalactic magnetic field, see Fig. 4.1. In the energy range from 10^8 to more than 10^{12} GeV, the loss times due to pair production (blue dashed curve) as well as photohadronic interactions (orange dashed curve) are always shorter than the synchrotron loss times for a 1 nG (10 nG) intergalactic magnetic field, depicted as a thin solid red curve (thin dashed red curve). The total loss time (thick solid curve) is dominated by the pair production below about $7 \cdot 10^{10}$ GeV, and above said energy by photohadronic interactions. However, at energies below 10^8 GeV the synchrotron losses gain importance with respect to the total loss rate. We also apply an additional simplification by neglecting the creation and/or decay of neutrons during propagation. Again, due to the large scales being considered, it is most of the time sufficient to assume that the neutrons decay before they interact again. As can be seen from Fig. 4.1, the neutron lifetime (thin solid green curve) is always shorter than the loss timescales.

¹Protons are assumed to be nuclei with $Z = 1$.

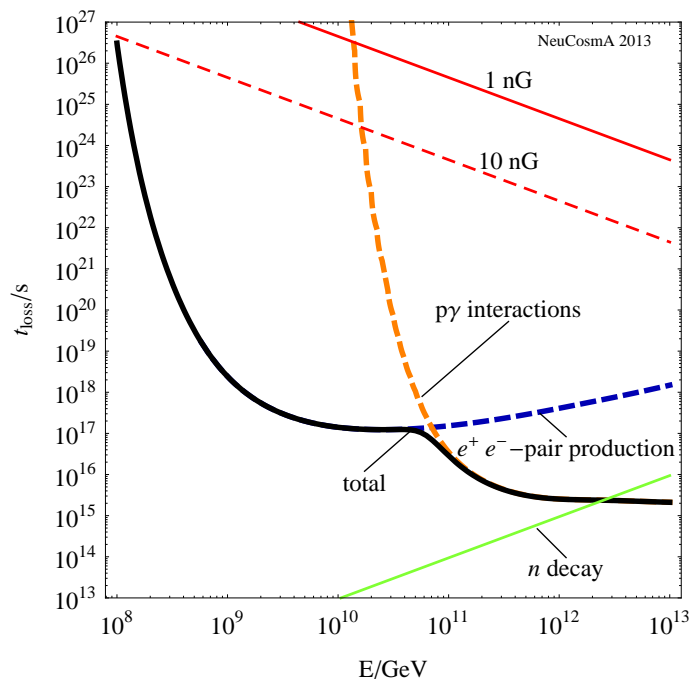


Figure 4.1.: The plot is a reproduction of the loss times due to interactions with the CMB photons (for $z = 0$). The total loss time (thick solid curve) consists of the losses due to pair creation (dashed blue curve) and the photohadronic losses (dashed orange curve), which are derived from Eq. (2.14) and the energy loss per interaction $\langle x_{p \rightarrow \pi} \rangle$, based on the spectrum from Eq. (4.1). For comparison reasons, we have also included the synchrotron loss time from Eq. (2.15) for an assumed intergalactic magnetic field of 1 nG (10 nG) as a thin red solid curve (thin red dashed curve). As can be seen from this plot, the loss time due to synchrotron losses on the intergalactic magnetic field are much longer than any of the other losses, even at $z = 0$. At higher redshifts, the losses due to the CMB are even higher due to the scaling of the photon density. Moreover, we have included the decay rate of neutrons (solid green curve) to show that the treatment of a coupled proton-neutron system is valid. As can be seen from the plot, the lifetime of neutrons is always shorter than the loss timescales, apart from energies beyond 10^{12} GeV.

Only at energies beyond 10^{12} GeV do the neutrons live long enough to interact before decaying. In those energy ranges, a mixed proton-neutron system is to be expected. However, due to isospin symmetry, it is possible to treat the protons and neutrons effectively as one species of particles, which simplifies the calculations.

For the actual calculation of the CR propagation, we are more interested in the development of the CR density as a whole and not in the propagation of individual particles. Hence, instead of using a stochastic treatment to model the propagation of individual particles, as done by several other CR propagation codes such as GalProp [178] or CRPropa [179], we will apply a propagation approach using a Boltzmann transport equation together with the continuous loss approximation, suggested by Ahlers et al. [161, 162]. Since the extra-galactic CR component is considered to be isotropic, we can assume that anisotropies are smeared out during the propagation of the CR and can be neglected. Moreover, we assume that the cosmic ray spectrum is stationary. Thanks to these assumptions a propagation approach using a single Boltzmann equation is viable. The according equation for the

(comoving) number density Y_p , as given in Ref. [162], is

$$\dot{Y}_p = \partial_E (H E Y_p) + \partial_E (b_{e^+e^-} Y_p) + \partial_E (b_{p\gamma} Y_p) + \mathcal{L}_{\text{CR}} \quad , \quad (4.4)$$

with E being the energy at the according point in time/redshift, what we call the source frame. The comoving number density Y_p (in $[\text{GeV}^{-1} \text{Mpc}^{-3}]$) is related to the “real” number density n_p as

$$Y_p(E, z) = a^3(z) n_p(E, z) = \frac{n_p(E, z)}{(1+z)^3} \quad (4.5)$$

with the relation of scale factor a and redshift z as in Eq. (B.7). Note that we here use a slightly different scaling than in case of Eq. (4.2) as we treat the energy losses due to the cosmic expansion in the Boltzmann equation itself. Specifically, the first term on the r.h.s. of Eq. (4.4) accounts for the (continuous) energy losses due to the adiabatic cosmological expansion, with H being the Hubble parameter for the according time-step. The second and the third term account for the e^+e^- -pair production and photohadronic losses, respectively. Moreover, since we are more interested in the evolution in redshift than actually in time, we can use the relation $dz = -dt(1+z)H(z)$ to change the Boltzmann equation from Eq. (4.4) to one in z . The resulting differential equation in z is given by

$$-\partial_z Y_p(E, z) = \frac{1}{(1+z)H(z)} \{ \partial_E [H(z) E Y_p(E, z)] + \partial_E [b_{e^+e^-}(E, z) Y_p(E, z)] + \partial_E [b_{p\gamma}(E, z) Y_p(E, z)] + \mathcal{L}_{\text{CR}} \} \quad , \quad (4.6)$$

with the redshift dependent Hubble parameter as in Eq. (B.9). The redshift and energy dependent energy loss rates $b_{e^+e^-}$ and $b_{p\gamma}$ are calculated based on the photon densities, with the definition of the energy loss rates as described in Eq. (4.3). For both types of processes, the contributions from the CMB and the CIB are combined to give a total rate.

The last term of Eq. (4.4), \mathcal{L}_{CR} , represents the cosmic ray injection rate. This quantity quantifies how much cosmic rays of a certain energy are injected at a certain redshift. In principle, this term needs to include the injections from all (relevant) sources or source classes, which can evolve in z . The aforementioned evolution in z can include the evolution of the number of sources in z as well as the model of the sources in z , similar to the different populations of stars. In this work we will, however, use the simplest possible model of only one source class, namely GRBs, which does not evolve in z . The only distribution in z will be due to the different number of source at a certain redshift. Hence, the cosmic ray injection rate factorizes as

$$\mathcal{L}_{\text{CR}}(E, z) = \mathcal{H}_{\text{CR}}(z) \cdot \mathcal{Q}_{\text{CR}}(E) \quad (4.7)$$

with the distribution of the sources in redshift $\mathcal{H}_{\text{CR}}(z)$, as defined in Eq. (1.9), and the cosmic ray injection spectrum of a single source $\mathcal{Q}_{\text{CR}}(E)$. For the sake of simplicity, we will assume that the sources are only GRBs and that all bursts are identical. Both \mathcal{L}_{CR} and \mathcal{Q}_{CR} are in $[\text{GeV}^{-1} \text{Mpc}^{-3} \text{s}^{-1}]$. In principle, \mathcal{Q}_{CR}

is a combination of the CR injection spectrum $Q'_{\text{CR}}(E)$ from the photohadronic interaction calculation and the local GRB rate density $\dot{\rho}_{\text{GRB}}(z=0)$, namely

$$\mathcal{Q}_{\text{CR}} = \frac{Q'_{\text{CR}}(E) \cdot V'_{\text{iso}} \cdot T'_{90}}{\Gamma} \cdot \dot{\rho}_{\text{GRB}}(z=0) \quad . \quad (4.8)$$

The first factor is the energy spectrum in the source frame of a burst (in $[\text{GeV}^{-1}]$), while the second term is here in $[\text{Mpc}^{-3} \text{s}^{-1}]$. Again, we will not specify the exact value of $\dot{\rho}_{\text{GRB}}(z=0)$ here, but use it as a free parameter to normalize the final result. However, it should be possible to obtain the local GRB rate from this type of calculation. More precisely, we can relate it to another commonly used quantity: the number of (long) bursts per year.

The observed number of bursts per year is normally given to be about $\dot{N} = 1000$, with 2/3 of these bursts being assumed to be long. This number can be related to the distribution in redshift from Eq. (1.7) by defining that

$$\dot{N} = \int_0^{\infty} \frac{d\dot{N}}{dz} dz \quad . \quad (4.9)$$

In Eq. (1.7), there are now several factors which need to be discussed in the context of the emission from the whole sample of GRBs. First of all, there is the beaming correction $\langle f_{\text{beam}} \rangle$, which incorporates the limited possibility to actually see a burst depending in which direction the jet, or the emission from the jet, is beamed. If we include this factor, which increases the total number of bursts compared to the observed one ($0 < \langle f_{\text{beam}} \rangle^{-1} < 1$), we also need to reduce the emission from a single source to actually include the emission from a jet (instead of isotropic emission). Hence, in our CR calculation the beaming factor cancels out. The second factor is the function $\mathcal{E}(z)$ which connects the GRB rate with the SFR; $\dot{\rho}_{\text{GRB}}(z) = \mathcal{E}(z) \dot{\rho}_*(z)$. The third factor is the function $F(z)$, which essentially accounts for bursts which are too faint to be observed. Only a fraction $0 < F(z) < 1$ of all bursts is bright enough to be detected on Earth. Therefore, it is possible to define a total number of bursts as

$$\dot{N}_{\text{tot}} = \int_0^{\infty} \frac{1}{F(z)} \frac{d\dot{N}}{dz} dz \quad . \quad (4.10)$$

By comparing \dot{N} and \dot{N}_{tot} , we can define a redshift independent ratio

$$f_{\text{thresh}} \equiv \frac{\dot{N}}{\dot{N}_{\text{tot}}} \quad (4.11)$$

due to detector threshold. Assuming the luminosity distribution from Wanderman and Piran, see Eq. (2.37), and the redshift distribution from Kistler et al., see Eq. (2.36), we obtain $f_{\text{thresh}} \simeq 0.51$ for a detector threshold of $1.75 \cdot 10^{-8} \text{ erg s}^{-1} \text{ cm}^{-2}$ and luminosities ranging from 10^{50} to $10^{54} \text{ erg s}^{-1}$. As always, this depends on the chosen parameters and distributions, *e.g.* changing the minimal assumed luminosity to $10^{49} \text{ erg s}^{-1}$ leads to a ratio of 0.29.

When we now rewrite \dot{N}_{tot} from Eq. (4.10) with the help of Eq. (1.7) and use $\dot{\rho}_{\text{GRB}}(z) = \mathcal{H}(z) \cdot \dot{\rho}_{\text{GRB}}(z=0)$, we obtain

$$\dot{N}_{\text{tot}} = \dot{\rho}_{\text{GRB}}(z=0) \cdot \int_0^{\infty} \mathcal{H}(z) \frac{dV/dz}{1+z} dz \equiv \dot{\rho}_{\text{GRB}}(z=0) \cdot 4\pi d_H^3 \cdot f_z \quad , \quad (4.12)$$

with f_z being the result of the integral divided by $4\pi d_H^3$, and d_H being the Hubble length, see Eq. (B.10). In principle, f_z quantifies how well the “local GRB rate” $\dot{\rho}_{\text{GRB}}(z=0)$, which is often referred to in the literature, describes the whole redshift range for a given distribution in z . To give some numbers for f_z : For the strong evolution as proposed by Kistler et al. [87], we obtain $f_z = 25.15$, which signifies a high contribution from larger redshifts. Finally, we can solve Eq. (4.12) together with $\dot{N} = 1000$ and $f_{\text{thresh}} = 0.5$ (and the aforementioned f_z) to obtain a value for the local GRB rate of $\dot{\rho}_{\text{GRB}}(z=0) = 0.08 \text{ Gpc}^{-3} \text{ s}^{-1}$. This is comparable with the results obtained in previous analyses, such as in Ref. [157], but also see the works by Schmidt on how the result can vary [180, 181]. Moreover, choked or “dark” GRBs could also contribute to the CR and neutrino fluxes without emitting any gamma-rays, which could be accounted for by a further correction factor.

Now, after having discussed the different loss mechanisms and possible corrections to the distribution in z , we can apply these local ($z=0$) loss timescales for some general considerations. As done by Waxman in Ref. [182], we can utilize these timescales to estimate what the actually needed local cosmic ray energy injection rate is. However, since the result from Ref. [182] is nearly 20 years old, we will incorporate current cosmic ray data from Ref. [5]. We will only use the data in the range from 10^{10} to 10^{12} GeV, which is the UHECR energy range as defined by Waxman. With this approach and the new data, we obtain a local cosmic ray injection rate $\dot{\epsilon}_{\text{CR}}^{[10^{10}, 10^{12}]} = 1.5 \cdot 10^{44} \text{ erg Mpc}^{-3} \text{ yr}^{-1}$, which is compatible with the original result of $(4.5 \pm 1.5) \cdot 10^{44} \text{ erg Mpc}^{-3} \text{ yr}^{-1}$. Hence, for GRBs to be the sources of UHECR, we need at least this energy injection in said energy range.

When we now compare this needed injection rate to the energy released by a single GRB, we (again) need to consider a few aspects beforehand. For one, the luminosity of the prompt emission is normally calculated from the observed emission in gamma-rays. As we detailed in chapter 2, this luminosity is then related to the energy in protons with help of the “baryonic loading” f_e^{-1} , with the usually assumed value $f_e^{-1} = 10$. Additionally, the energy release is only needed in the energy range of the UHECR, and not over the whole energy range, as done in Eq. (2.28). This can be corrected using a bolometric correction f_{bol} , which compares the energy in the range from 10^{10} to 10^{12} GeV to the one in the whole energy range. For $\alpha_p = 2.0$, the UHECR only have about a fifth of the total energy, or $f_{\text{bol}} \simeq 0.2$. Moreover, not all protons can escape as cosmic rays, as we discussed in chapter 3. Even in the simplest case of neutron escape, only the fraction $f_{\text{CR}} \simeq 0.4$ of the proton energy inside the burst is released as cosmic rays. This follows the logic that about half the photohadronic interactions produce neutrons and the neutrons obtain all the parent proton energy apart from the amount lost to pions; $f_{\text{CR}} \simeq 0.5 \cdot (1 - f_{\pi})$ with

$f_\pi \approx 0.2$. Hence, the energy ejected by a burst as UHECR can be calculated as

$$E_{\text{CR}}^{[10^{10}, 10^{12}]} = f_{\text{CR}} \frac{f_{\text{bol}}}{f_e} E_{\gamma, \text{iso}} \quad . \quad (4.13)$$

As can be seen from the previous discussion, there are a lot of factors which are not yet experimentally determined and we need to make some assumptions concerning them, when we want to interpret the results in the following section. For comparability reasons, we will assume that the number of observed bursts is $\dot{N} = 1000$, $f_{\text{thresh}} = 0.5$, and no contribution from dark bursts. We will continue to use the strong evolution case by Kistler et al., as in Eq. (1.7), hence $f_z = 25.15$. The fractions f_{CR} and f_{bol} are automatically fixed by our code and our choice of α_p , respectively.² As a consequence, we will use the baryonic loading as the free parameter for the normalization of the CR prediction.

4.2. The combined results for UHECR, prompt GRB neutrinos, and cosmogenic neutrinos

For the following analysis, we will use a two step calculation. The first step is to calculate the neutrino and cosmic ray spectra, as described in chapter 3. In the second step, we will use the propagation code described in the previous section to “transport” the particles from a certain redshift down to Earth ($z = 0$). As stated before, we will assume that all bursts are identical in the source frame, as we want our result for a single GRB to be independent of z . We will, again, assume standard parameters for the burst, as given in Table 1.1. For the Lorentz factor, we will use two values: $\Gamma = 300$ for a classical neutron escape burst (with no direct component), and $\Gamma = 800$ for a burst which is direct escape dominated, compare to upper right plot in Fig. 3.3. Moreover, since we want to have a chance of actually reaching the highest CR energies, we will assume efficient acceleration ($\eta = 1$); compare to values in upper right scan of Fig. 3.5. The resulting particle spectra for these two source models can be seen in Fig. 4.2. The left plot shows the spectra for the classical neutron escape source, from which only the neutron component (solid blue curve) is considered for CR injection. For the direct escape dominated source, both the neutron component as well as the direct escape component (solid green curve) are used, see right plot of Fig. 4.2. For the source distribution, we will again assume the strong evolution approach suggested by Kistler et al. [87]. Hence, \mathcal{H}_{CR} is given by Eq. (1.9).

The advantage of our simple CR propagation code is that we can now directly calculate the cosmogenic neutrinos (also called GZK neutrinos). Based on the initial prediction of the suppression of the cosmic rays at high energies, see Refs. [3, 4], there have been several predictions on the level of this neutrino flux, see, *e.g.*, Ref. [183]. Hence, when we normalize our spectra after propagation with help of the cosmic

²Technically, the other burst parameters apart from α_p indirectly affect f_{bol} as well, since we calculate $E_{p, \text{max}}$ self-consistently.

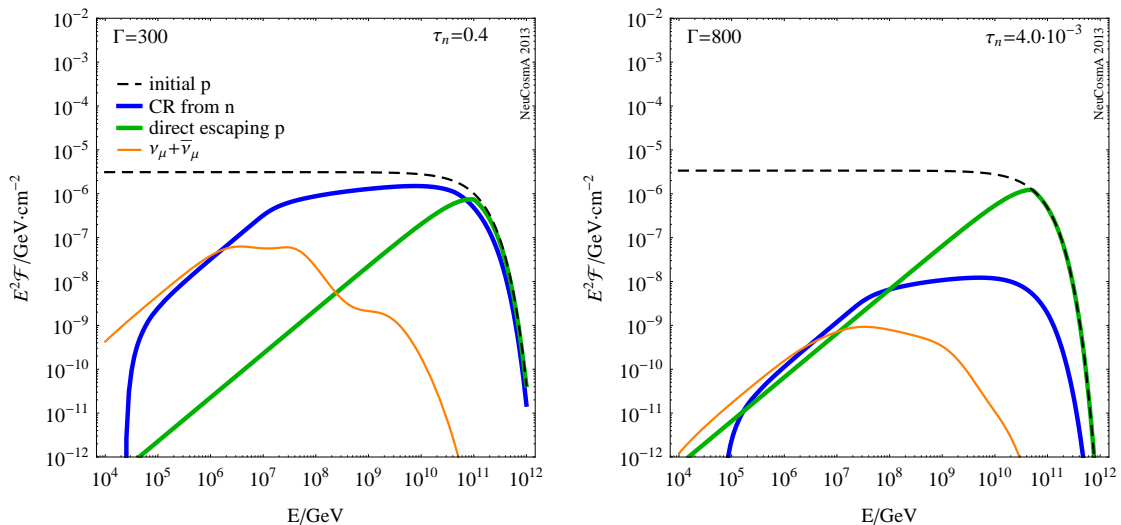


Figure 4.2.: The predicted particle spectra for the two source models used for the CR propagation simulation. The left plot shows the spectra used for the neutron escape model ($\Gamma = 300$), while the right plot depicts the direct escape dominated one ($\Gamma = 800$). For the neutron model, only the neutrons (blue solid curve) are considered for the CR injection. In the direct escape dominated model, the neutrons as well as the direct component (solid green curve) are considered.

ray data, we can use the level of the cosmogenic neutrino flux as a cross-check. We used a χ^2 -fit to match our CR flux prediction to the UHECR data from the HiRes experiment [184], with the results depicted in the left plot of Fig. 4.3. As long as we consider only the UHECR energy range from 10^{10} to 10^{12} GeV (gray-shaded energy range), both models are viable, with the neutron escape model fitting the data a bit better, *i.e.* we obtain a $\chi^2/\text{d.o.f.}$ -value of 1.99 for the neutron escape model while for the direct escape dominated one it is 5.25. The cosmogenic neutrinos (blue curves in right plot of said figure) are also both consistent with older predictions, such as from Ref. [183]. As expected, as long as we fit the cosmic ray to the observed data, the cosmogenic neutrinos do not change drastically. The predictions shown in Fig. 4.3 are also consistent with current ultra-high-energy neutrino data. Based on the effective area from Ref. [12] (thin solid black curve), it is possible to estimate that about one neutrino event should have been detected so far, which is still consistent with current data; $N_\nu = 0.81$ for the neutron only model, and $N_\nu = 0.80$ for the direct escape model. The much stronger constraints are, however, obtained from the prompt neutrino emission, as discussed in Refs. [135, 161]. As can be seen from the right plot, the prompt GRB neutrino flux in the neutron escape model (orange solid curve) is already above current GRB neutrino sensitivity limits, based on the model-independent IC40+59 GRB neutrino effective area from Ref. [135] (thin dashed black curve). This confirms the results from Refs. [135, 161], which claim that GRB models are severely constrained. However, for the direct escape model, the prompt GRB neutrino flux (dashed orange curve) is about one order of magnitude below the prediction for the neutron escape model. This confirms our previous conclusions that prompt neutrinos are expected to be reduced compared to the cosmic rays in the direct escape case, see discussion in Sec. 3.2, while the

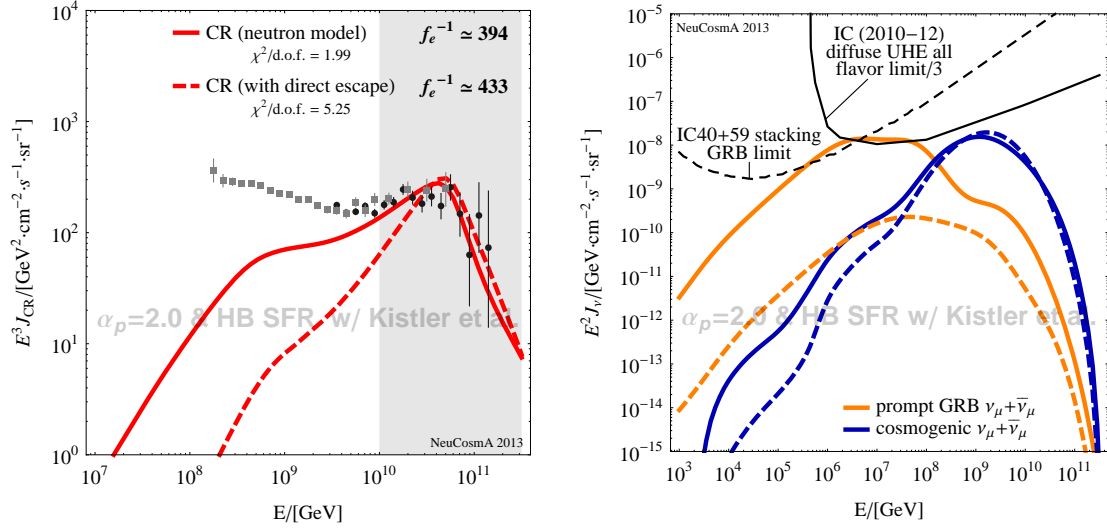


Figure 4.3.: The cosmic ray (left plot) and neutrino flux predictions (right plot) for GRBs following the redshift distribution from Eq. (1.9). The two results here are both for an assumed proton spectral index of $\alpha_p = 2$. The difference between the two results comes from the choice of Γ . For the “neutron only”-case, the standard value of $\Gamma = 300$ is assumed (solid curves), while for the direct escape dominated model a Lorentz factor $\Gamma = 800$ is assumed (dashed curves). Both results were normalized to UHECR data from the HiRes experiment, with only the data from 10^{10} to 10^{12} GeV being used (gray-shaded region in left plot). While the prompt neutrinos of the neutron escape model (solid orange curve) already violate current IceCube GRB neutrino bounds, shown as model-independent IC40+59 GRB sensitivity limit from Ref. [135] (thin dashed black curve), the prediction for the direct escape dominated model is still one order of magnitude below current sensitivity. The cosmogenic neutrinos, depicted as blue curves in the right plot, are nearly at the same level for both CR escape models. The high-energy neutrino sensitivity is based on the effective area shown in Fig. 3 of Ref. [12].

cosmogenic neutrinos are unaffected as they are related to the CR propagation. The direct escape model is therefore not ruled out yet based on the neutrino observations, as opposed to the neutron model.

Another aspect is, however, the normalization itself. As we discussed in the previous section, we have chosen the burst parameters as well as the observed number of bursts \dot{N} fixed, leaving only the baryonic loading f_e^{-1} as a free parameter. Recall that it was initially assumed that a value of $f_e = 0.1$ (or $f_e^{-1} = 10$) is a realistic fraction of energy in electrons compared to energy in protons. If we now deconvolve the normalization factor obtained by fitting the CR prediction to the HiRes data, we obtain quite different values. In case of the neutron prediction, a baryonic loading of $f_e^{-1} \simeq 394$ is needed, while for the direct escape model $f_e^{-1} \simeq 433$ is obtained. Hence, the needed baryonic loading is significantly higher than initially assumed. It needs to be determined, how realistic such high amounts of baryons actually are. Also, the importance of pp -interactions, which have so far been neglected, increases with the rise of the amount of baryons. A more realistic study of the acceleration inside GRBs is needed to clarify this aspect, but has to be done at some future point. In general, it is once again a question of the parameters as well as the actually used distribution functions, if GRBs can be ruled out as the sources of UHECR. To understand the effects of the different parameters on the neutrino and CR flux predictions, a more extended study of these parameters is needed and will be presented elsewhere [185].

5. Effect of neutrino lifetime

One further question in neutrino physics is the question of neutrino lifetime. While the mass of neutrinos can already be considered an effect beyond the current standard model, further “new physics effects” could still be a possibility in nature. The stability of the mass eigenstates is one of the issues which are discussed, while others are things such as additional “sterile” neutrino states. In this chapter, we will discuss the possibility of the neutrino mass states being unstable. The simple heuristic reason for the instability of the neutrino mass eigenstates is that only the lightest particles are considered stable by current standards, *e.g.* only electrons are considered stable charged leptons while muons and taus decay. Hence, there is no (theoretical) reason why all mass eigenstates should be stable, even though there are so far only observational bounds on neutrino decay. We will discuss the decays while obeying the lifetime bounds from SN1987A [8, 9] of $\tau/m \gtrsim 10^5 \text{ s eV}^{-1}$. These lifetime bounds are however connected to specific decay models, see, *e.g.*, Refs. [121, 186] for an overview. Radiative decays are strongly limited by solar neutrinos [187], while Majoron models [188, 189] can be limited by neutrino-less double-beta decay and supernovae [190]. Moreover, there are even models of decay into un-particles, see Refs. [191, 192, 193, 194]. Recently, there have been quite a number of publications discussing neutrino decay once again, see, *e.g.*, Refs. [195, 196], based on the current GRB neutrino data and the detection of the first UHE neutrino events. In the following chapter, we also want to test the effect of neutrino lifetime on the GRB neutrino flux prediction by assuming an effective decay of neutrinos into invisibles, without specifying the exact decay mechanism. Also, as discussed in Sec. 1.2.1 before, we will assume that neutrinos are Dirac particles.

5.1. The redshift-dependent decay framework

Mathematically, the decay of a mass eigenstate ν_i can be described by the usual differential equation for decay:

$$\frac{dN_i}{dt} = -\lambda_i N_i \quad , \quad (5.1)$$

with the decay rate (inverse lifetime) λ_i . This rate is given as

$$\lambda_i = \frac{m_i}{E} \frac{1}{\tau_{i,0}} \equiv \frac{\kappa_i}{E} \quad , \quad (5.2)$$

where we use the particle Lorentz factor $\gamma_i = E/m_i$ to boost the rest frame lifetime $\tau_{i,0}$ to the observer’s frame. Since the actual lifetime is hardly measurable, be it in

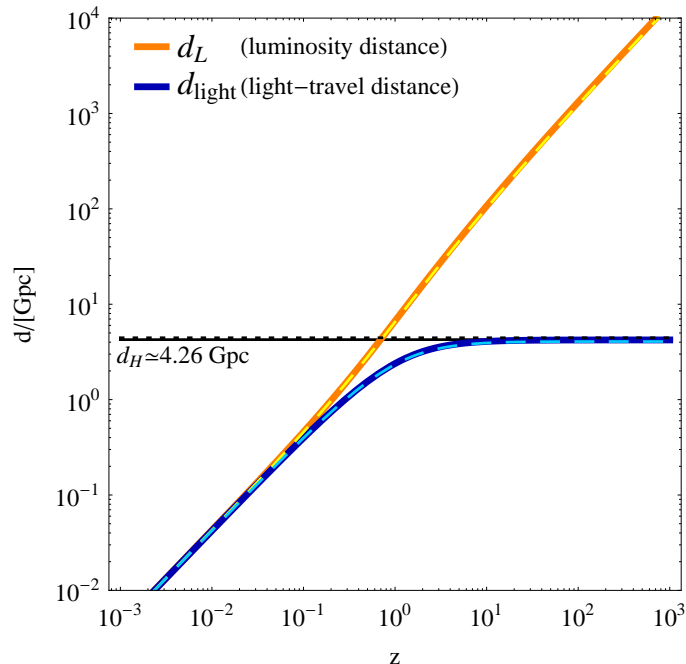


Figure 5.1.: The luminosity distance d_L and the light-travel distance d_{light} as a function of redshift, see legend inside plot. The solid curves represent the values used for the calculations in this work, while the dashed curves represent the updated values from *Planck*, see discussion around Table B.1. As can be seen from the plot, the light-travel distance is limited to the Hubble distance d_H , which is equivalent to requirement that the universe has a finite age, and, therefore, accessible size. As stated before, we are using the old WMAP results for our cosmological parameters. However, when comparing the WMAP (solid) to the *Planck* (dashed) curves, one can see that there are only very limited changes due to the update of the parameters.

the rest or observer's frame, the actual lifetime bounds of a neutrino mass eigenstate ν_i are typically given in $\kappa_i^{-1} = \tau_{i,0}/m_i$ [s eV $^{-1}$].

Since we want to discuss the decay on cosmological scales, we need to consider what the actual time t a particle has traveled is. More precisely, the distance d a particle needs to travel grows during propagation due to the expansion of the universe. Hence, the time traveled cannot be derived by simply dividing the distances defined in Appendix B with c , as they are fixed at a certain times during the expansion, compare Eqs. (B.8) and (B.13). For the decay, an integral definition over the whole propagation and expansion between production and detection is needed. This requirement is fulfilled by the light-travel or lookback distance. It is defined as

$$d_{\text{light}} = d_H \int_0^z \frac{dz'}{(1+z') \sqrt{\Omega_m(1+z')^3 + \Omega_\Lambda}} \quad (5.3)$$

with $d_H \approx 4.26$ Gpc being the Hubble length, see Eq. (B.10). As can be seen from Fig. 5.1, the light-travel distance is limited by the Hubble length d_H , which is the maximal distance an ultra-relativistic particle can travel in the whole age of the universe t_H . This has one significant, and for theorists unwanted, consequence, namely that the maximal distance is in fact not infinite and complete decay is

not always given even at highest redshifts, as we discuss in more detail in Ref. [197]. While a naive guess would be to just adapt the solution for Eq. (5.1) to accommodate redshift, it is actually needed to adapt the whole differential equation to redshift. For this, we again need to use $dz = -dt(1+z)H(z)$ as in Sec. 4.1 and change Eq. (5.1) to

$$\frac{dN_i}{dz} = \frac{\kappa_i}{E(1+z)H(z)} N_i \quad . \quad (5.4)$$

This equation can be solved by simple separation of variables, together with the definition that the current epoch of $z = 0$ is the point-of-reference for the calculation, *i.e.* by also inserting $E(z) = E_0(1+z)$. Using this, it is possible to obtain an suppression factor $D_i(E_0, z)$, which compares the initial number of neutrinos $N_i(E_0, z)$ to the final number of neutrinos $N_i(E_0, 0)$, giving

$$\begin{aligned} D_i(E_0, z) \equiv \frac{N_i(E_0, 0)}{N_i(E_0, z)} &= \exp \left(-\frac{\kappa_i d_H}{E_0} \int_0^z \frac{dz'}{(1+z')^2 \sqrt{\Omega_m(1+z')^3 + \Omega_\Lambda}} \right) \\ &= [\mathcal{Z}(z)]^{-\frac{\kappa_i d_H}{E_0}} \quad . \end{aligned} \quad (5.5)$$

Note that the $\mathcal{Z}(z)$ used here is the same as $\mathcal{Z}_2(z)$ from Ref. [197]. In said reference, there is also a more detailed discussion of the different functions as well as the possibly obtainable bounds from cosmic neutrino observations. Here, however, we want to focus on the effect of the decay on the GRB calculations. For this reason, we need an effective representation of the decay factor for our numerical calculations. For this reason, we will use the analytical approximation for $\mathcal{Z}(z)$ proposed in Ref. [197]. This is given to be

$$\mathcal{Z}(z) \simeq a + be^{-cz} \quad (5.6)$$

with the constants

$$\begin{aligned} a &\simeq 1.71 \quad , \\ b &= 1 - a \simeq -0.71 \quad , \\ c &\simeq 1.27 \quad . \end{aligned} \quad (5.7)$$

The damping factor D_i can now be used to extend the oscillation probability from Eq. (1.15) to also include the effect of decay, giving

$$P_{\alpha\beta}^{\text{decay}}(E_0, z) = \sum_{i=1}^3 |U_{\alpha j}|^2 |U_{\beta j}|^2 D_i(E_0, z) \quad . \quad (5.8)$$

This definition is similar to the one used in Ref. [198]. In the next section, we will discuss the impact of the decay first using the four standard bursts from Table 3.1, and then we will discuss how the decay would effect the prediction for actual GRB neutrino searches.

5.2. The effect of decay on GRB neutrino fluxes

When we discuss the effect on the actual flux prediction, we will first of all take a look at some example bursts with known redshift. For this purpose, we will use two of the four bursts, which we already discussed in Sec. 3.2. We will, for now, use a hypothetical model with all neutrino states having the same lifetime, with several different values for this lifetime. Even though some of the chosen values actually violate bounds set by the SN1987A observation, we will use this approach for the sole reason that it is the simplest version of decay and leads to extreme effects on the neutrino flux prediction. Shown in Fig. 5.2 are the results for two of the four bursts, namely the standard burst “SB” and the very energetic burst GRB080916C. The lifetimes used for the calculations are shown in the legend inside the plots.

As for all the neutrino flux predictions from individual bursts, the shape of the flux prediction depends on the burst parameters. The results for the stable case (“no decay”, solid red curves in Fig. 5.2) are the same as the flux predictions (orange curves) from Fig. 3.7. The decay itself leads to a suppression of the neutrino flux below a certain energy. This can be derived by some considerations about $D_i(E_0, z)$ and when this factor goes to zero (complete decay). For a large enough decay rate $\kappa_i \gg E_0/d_H$, the integral over z in Eq. (5.5) is no longer relevant. Moreover, since the maximal distance is limited to the Hubble distance, the function \mathcal{Z} has an asymptotic limit. Using these considerations for $D_i(E_0, z) \rightarrow 0$, we can obtain the condition for complete decays as $\kappa_i d_H/E_0 \gg 1$, or

$$E_0 [\text{TeV}] \ll \frac{4 \cdot 10^5}{\kappa_i^{-1} [\text{s eV}^{-1}]} \quad . \quad (5.9)$$

Due to the limit on the actually traveled distance, all decays over distances of $z \gtrsim 1$ can be considered “complete”, as can be seen from how the light-travel distance is limited to d_H in Fig. 5.1. At these redshifts, it only depends on the energy and not on the distance traveled, if a neutrino is expected to have decayed or not. Hence, as all the bursts from Table 3.1 have $z > 1$, they all should be affected by complete decays. Additionally, it is possible to estimate the value for E_0 at which the flux is suppressed based on the lifetime, *e.g.* for $\kappa^{-1} = 100 \text{ s eV}^{-1}$ the flux is suppressed below 4 PeV, see left panel of Fig. 5.2. For smaller redshifts, this suppression shifts to lower energies, as the function \mathcal{Z} has not fully reached its asymptotic limit yet and the damping is weaker.

Since we have obtained that decays from $z \simeq 1$ can be considered complete, it is interesting to test what the effect on the diffuse flux would be in this simple scenario. As discussed in Ref. [107], bursts from $z \simeq 1$ should dominate the diffuse flux prediction. If we now test an energy $E_0 \simeq 10^6 \text{ GeV}$, which is roughly the energy of peak sensitivity of most large neutrino telescopes, we obtain that we need a lifetime $\kappa^{-1} \lesssim 400 \text{ s eV}^{-1}$ for complete decays from Eq. (5.9). For these values, the convolution of GRB rate, flux scaling, and damping shifts the peak of the contribution to low $z \simeq 0$. From a conceptual point of view, this means that the neutrinos from closer bursts did not have the time to decay, while neutrinos from some distance are suppressed. On the other hand, for $\kappa^{-1} > 400 \text{ s eV}^{-1}$, the diffuse

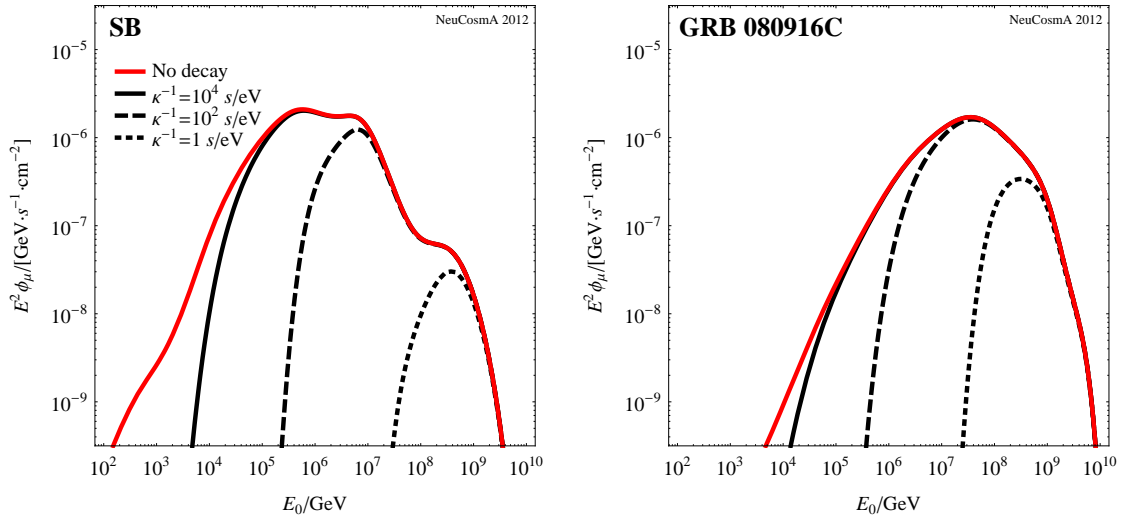


Figure 5.2.: These plots show the effect of decay on the neutrino flux from two of the four burst from Table 3.1. The stable curves (“no decay”, red solid curves) correspond to the neutrino curves from Fig. 3.7. We have assumed complete decay of all three mass eigenstates, when we assume the neutrinos to be unstable, with the different lifetimes stated in the legend. As discussed in the text, the decay is considered to be “complete”, which means that it only depends on the energy and not the distance traveled. The energy below which the neutrino flux is suppressed can be estimated with Eq. (5.9). Figure based on one from Ref. [197].

flux is still dominated by bursts from $z \simeq 1$. Finally, we can use the lifetime bound from SN1987A, which is even higher than the lifetimes shown in Fig. 5.2, to show that a phenomenologically viable model would not have these extreme effects. One way to accommodate the SN1987A bound would be to assume different lifetimes for the different mass eigenstates, with the key assumption being that ν_1 is stable. In the following, we will use a model with only ν_2 and ν_3 unstable.

Thanks to the observation of ν_e from SN1987A, we more or less know that at least ν_1 , which is the main contributing mass eigenstate of ν_e , should have a quite long lifetime, *i.e.* about $\kappa_1^{-1} \gtrsim 10^5 \text{ s eV}^{-1}$. The experimental bounds on the other two mass eigenstates are, however, much weaker. Since ν_2 also contributes to ν_e , choosing it unstable will also affect the ν_e flux to some extent. Yet, as long as ν_1 is stable, it is sufficient for the ν_e fluxes to fulfill the SN1987A bounds based on the uncertainties of the supernova neutrino models. The effect of an unstable ν_3 is hardly visible on the ν_e flux, even though there is a small contribution due to $\theta_{13} \neq 0$. Hence, when we assume that ν_2 and ν_3 are unstable, we will have effects on the flavor states based on the mixture of each mass eigenstate. ν_2 is roughly an equal mixture of ν_e , ν_μ , and ν_τ , while ν_3 consists mainly of ν_μ and ν_τ , with only a small contribution of ν_e . When we now apply this scenario to the standard burst SB, as discussed in Ref. [197], we see that the flavors are differently suppressed by the decay of ν_2 and ν_3 . We depict the decay results for this scenario as thick solid curves in Fig. 5.3, with each panel representing a different lifetime. The different neutrino flavors are color-coded with the blue curves representing $\nu_e + \bar{\nu}_e$, the orange curves $\nu_\mu + \bar{\nu}_\mu$, and the green curves $\nu_\tau + \bar{\nu}_\tau$. In the stable case (upper left plot), all flavors have roughly the same observed flux level at the first peak (between

10^5 and 10^6 GeV); the stable case is depicted as a thin dashed color-coded curve for each flavor in every other panel. However, as soon as we assume that only ν_1 remains stable, the neutrino fluxes get suppressed below a certain energy, just as discussed before. Again, the value below which the flux is suppressed is determined by the lifetime, as in Eq. (5.9). For example, an energy $E_0 \simeq 4 \cdot 10^8$ GeV is obtained for $\kappa^{-1} = 1 \text{ s eV}^{-1}$, below which ν_2 and ν_3 have completely decayed (lower left plot). This leads to an enhancement of the kaon peak, which coincides with the aforementioned energy, in the muon and tau neutrino spectra. The effect on the electron neutrinos is milder. As can be seen from the most extreme depicted case, in the the lower right panel of Fig. 5.3, the decay leads to the electron neutrino flux being enhanced compared to the muon and tau neutrino flux. The lifetime κ^{-1} used in said case corresponds to ν_2 and ν_3 decaying with the current κ_2^{-1} bound ($\gtrsim 10^{-4} \text{ s eV}^{-1}$), taken from Refs. [199, 200, 201]. Moreover, the asymmetry between ν_μ and ν_τ is due to the choice of θ_{13} , θ_{23} , and CP-violation phase δ_{CP} , see values given in Table 1.2. A consequence of this “enhancement” of ν_e is that the amount of electromagnetic cascades in large neutrino telescopes, such as IceCube, is expected to be increased compared to the muon tracks or hadronic showers. For a detailed discussion of the changes of the expected events in a neutrino telescope, please refer to Ref. [197]. Nonetheless, this scenario predicts more cascades than muon tracks, which incidentally fitted the detection of the first two events which passed all of the background cuts, see Ref. [12]. These two events were cascade events which indicated neutrino energies of about 1 PeV, with no muon tracks being detected/passing the cuts. More recent data, however, does not have this excess of cascades over muon tracks, but no additional events in the PeV-range have been detected so far, see Ref. [13].

Since we already discussed the different possibilities how to bound GRBs as sources of UHECR using the neutrino flux prediction in the previous chapters, we now want to discuss why decay can also be a possibility to circumvent current bounds. For this reason, we will apply the decay scenario from the previous paragraph — ν_1 assumed to be stable, only ν_2 and ν_3 can decay — to the recalculation of the IC40 prediction from Ref. [136]. Using the same parameters and calculation approach as in said reference, we only extend the flavor mixing to also include the redshift-dependent damping term, as in Eq. (5.8). The result for the muon neutrinos (left plot) as well as electron neutrinos (right plot), based on the stacking of the 117 bursts of the IC40 sample, can be seen in Fig. 5.4. For the muon neutrinos, the red solid curve (“no decay” case) corresponds to the prediction given in Fig. 3 of Ref. [136]. The blue solid curve in the right plot is the corresponding “no decay” prediction for ν_e . The normalization of all the predictions are based on the observed gamma-rays of each burst, as detailed in Ref. [136]. As discussed in Sec. 2.4, the quasi-diffuse flux is still subject to some statistical uncertainties as well as the impact of the choice of the standard parameters. Since the standard parameters include $z = 2$, all bursts without measured redshift will be subject to complete decay. As a consequence, when the assumed lifetime is low enough, $\kappa^{-1} \lesssim 1 \text{ s eV}^{-1}$, the muon neutrino flux prediction gets suppressed below the ten year IC86 sensitivity limit, see left plot in Fig. 5.4 (solid gray and dotted black curves). Compared to the original prediction, the decay decreases the muon neutrino flux by another order of magni-

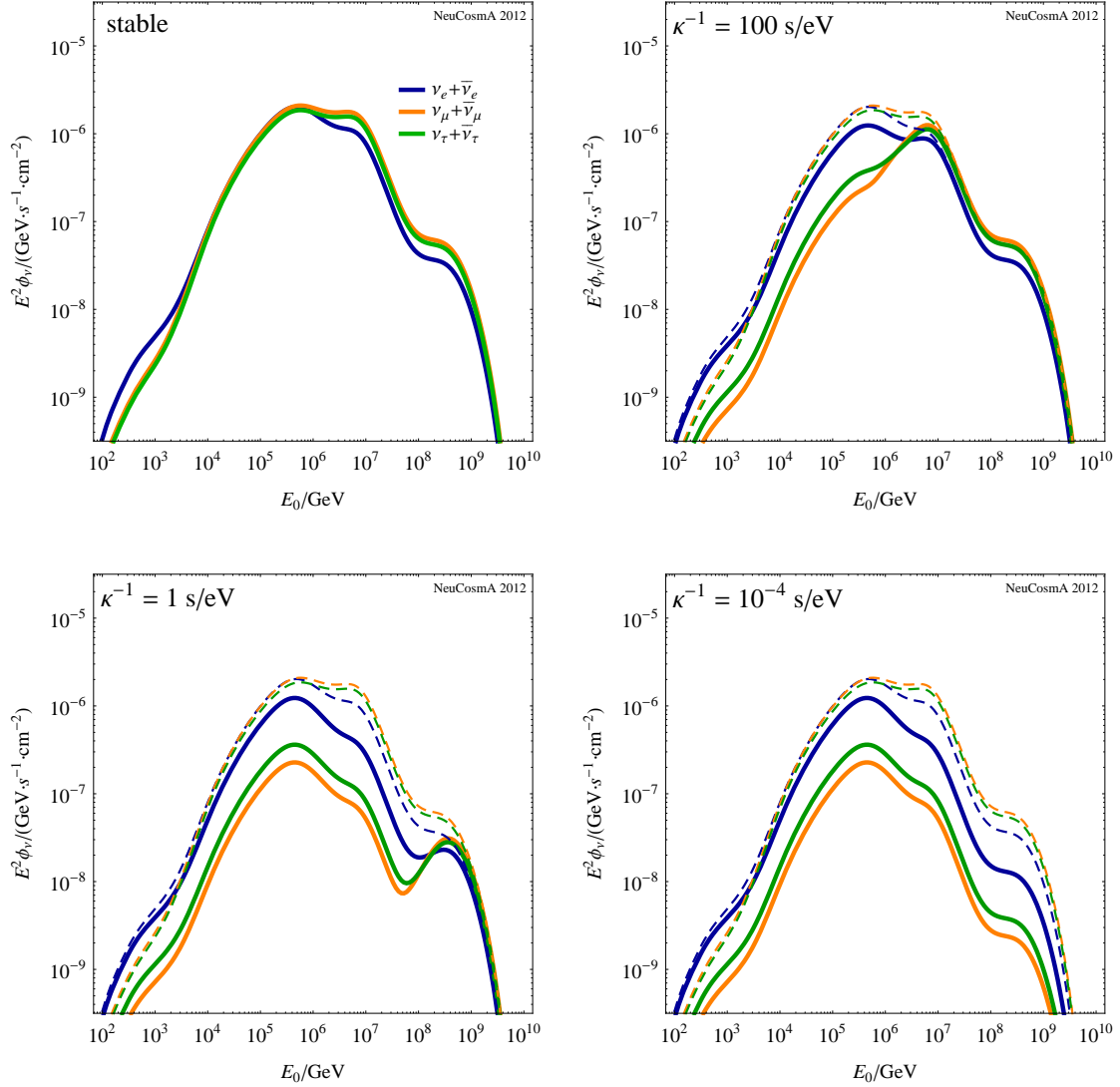


Figure 5.3.: Prediction for the neutrino spectra of the different flavors as a function of energy, based on the SB for the decay scenario with ν_1 assumed stable with neutrinos and antineutrinos summed over. The different panels represent different lifetimes κ , which is assumed to be associated with ν_2 and ν_3 . The lifetime values, given in each panel, are all consistent with the SN1987A decay bound. The color-coded thick curves (see legend in upper left plot) represent the results for the stated lifetime value, while the thin dashed curves represent the stable case from the top left panel. Depending on κ^{-1} , all ν_2 and ν_3 are considered to have decayed at energies below E_0 , see Eq. (5.9). For example, in case of $\kappa^{-1} = 1 \text{ s/eV}^{-1}$, this energy is $E_0 \simeq 4 \cdot 10^8 \text{ GeV}$, and effectively leads to an enhancement of the kaon peak. Figure taken from Ref. [197].

tude. On the other hand, the electron neutrino flux is only mildly affected. Here, the decrease is only by about a factor of two.¹ Hence, even if no muon tracks are expected, there still should be a contribution from electromagnetic cascades. The effective area for electron neutrinos is normally assumed to be slightly lower than the one for muon neutrinos, but has the advantage of an increased effective area at the Glashow-resonance, see, *e.g.*, Fig. 3 in Ref. [12]. Said increase of the effective area is the result of the resonant production (and subsequent decay) of a W^- -boson when $\bar{\nu}_e$ interact with e^- , as described by Glashow in Ref. [202]. When the electrons are at rest, the antineutrinos need an energy $E_{\nu,0} = m_W^2 / (2m_e) \simeq 6.3$ PeV for the resonant interaction. Moreover, in case of the aforementioned search for UHE neutrinos [12], the effective area for ν_e at about 1 PeV is actually higher by a factor of a few than the one for ν_μ (or ν_τ). This might also be the reason why the first detected events were actually cascades and not muon track events. However, since we do not have data on the actual ν_e effective area for the GRB searches, we cannot include a limit in the ν_e plot. Nonetheless, even though the current results on the astrophysical neutrinos do not indicate a suppression of muon tracks below a certain energy, neutrino decay would also affect the interpretation of the CR bounds we discussed in Sec. 4.2. With neutrino decay, the cosmic rays would stay at the same level while the neutrino fluxes, especially the prompt neutrinos, would be decreased. Therefore, it would even be possible to fulfill the cosmic ray bounds discussed in Refs. [135, 161], without changing the source distribution or the spectral index. Nonetheless, current data is in no way sufficient to claim or rule out neutrino decay. The first positive results presented in Ref. [12] as well as the information obtained with new search methods, as done by Whitehorn et al. [13], show that it should be possible to gain more insight soon. Surprisingly, the best data may actually come from cascade events, as the experimental cuts lead to higher effective areas for ν_e in the range around 1 PeV.

¹On a related note, the decay spectra for $\kappa^{-1} = 10^2 \text{ s eV}^{-1}$ are actually slightly higher than the original (“no decay”) prediction in both plots. This is due to an update of the mixing parameters, which are used for calculation. The original calculation uses the same mixing angles as we state in Ref. [107], the decay calculations are, however, done with the values stated in Table 1.2.

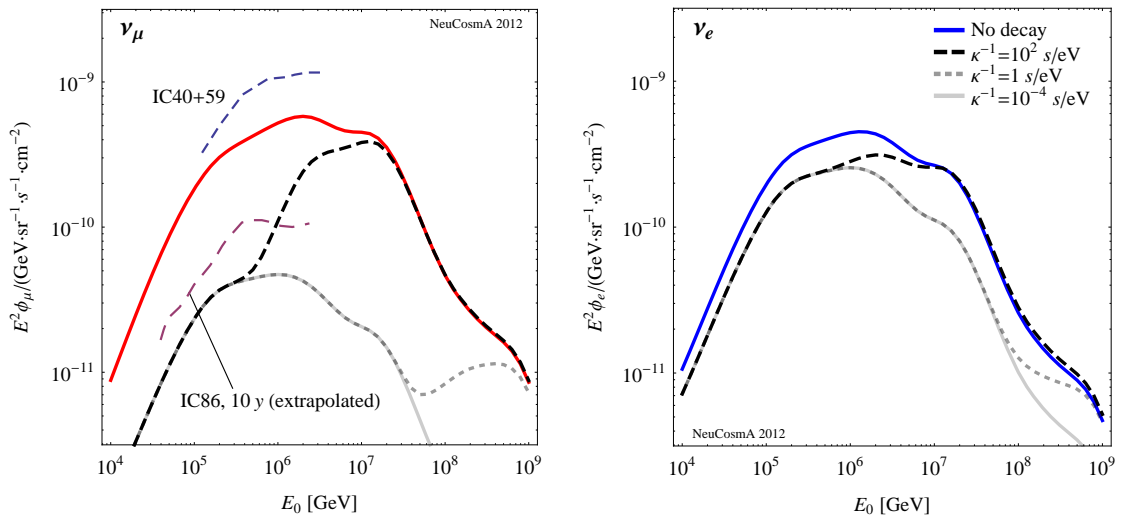


Figure 5.4.: Flux predictions for the muon neutrinos (left plot) and the electron neutrinos (right plot), based on the stacking of the 117 bursts of the IC40 flux sample. The calculation method is the same as in Ref. [136], however, extended to also include neutrino decay. Apart from the original (“no decay”) prediction (colorful solid curves; muon neutrinos are red, electron neutrinos are blue), each plot also includes the result for three different lifetimes (black dashed, black dotted, and gray solid curves). The used decay scenario for these predictions is, again, to assume that ν_1 is stable, while both ν_2 and ν_3 decay with κ (obeying the SN1987A bound). The depicted IC40+59 flux limit is taken from Ref. [135], while the extrapolation of the IC86 (after ten years of operation) is based on scaling up the IC40 effective area up by a factor of three, as suggested in, *e.g.*, Ref. [203]. Figure taken from Ref. [197].

6. An example for neutrinos from microquasars

As we have stressed in the initial discussion of neutrinos from GRBs, see chapter 2, the particle physics involved in the production of neutrinos are independent of the astrophysical source model. Hence, it is possible to apply similar photohadronic interaction calculations to other sources, as long as it is possible to derive the proton and photon densities. One possibility, which is very similar in its principle setup to the GRB internal shock fireball model, is the neutrino production in internal shocks of microquasars as suggested by Levinson and Waxman [204]. Opposed to GRBs, microquasars (MQs) are galactic binary sources, which have been detected in various wavelengths, including gamma-rays as well as radio. Especially, the detection in radio confirmed that MQs also exhibit relativistic radio jets, see Refs. [205, 206]. Hence, it is possible to obtain more information on the source itself than in the case of GRBs. The inferred boost factors are, however, much milder than in the case of GRBs. Nonetheless, there have already been studies on the possible neutrino emission from a number of MQs, with the one by Distefano et al. [207] based on the analytical model from Ref. [204] leading to the result that the largest number of neutrinos is to be expected from the MQs Cyg X-3 and XTE J1118+480. Analogous to how we extended the Waxman-Bahcall GRB neutrino model to a detailed numerical calculation, see Sec. 2.3, we now want to detail how to similarly extend the Levinson-Waxman model for neutrinos from MQs at the example of the bright MQ Cyg X-3, based on our Ref. [154].

Similar to the calculation on GRBs detailed in Sec. 2.3, we will normalize the different particle densities based on observed photon spectra. As suggested in Ref. [204], we will calculate the photon energy density inside the jet U'_γ (in the SRF) based on the luminosity L_γ passing through the surface of the jet, giving

$$U'_\gamma = \frac{L_\gamma}{4\pi (l^2 \sin^2(\theta_j)) c \mathcal{D}^2} \quad . \quad (6.1)$$

In this formula, l is the distance of the emission region from the central object, \mathcal{D} is the inferred Doppler factor of the jet, and θ_j is the jet's opening angle. This photon energy density can then be used to normalize the photon spectrum inside the jet, similar to Eq. (2.27):

$$\int \varepsilon' N'_\gamma(\varepsilon') d\varepsilon' = U'_\gamma \quad . \quad (6.2)$$

Moreover, the energy density can be used to calculate the value of the magnetic field B' , as described in Eqs. (1.5) and (2.25), as well as normalizing the proton energy density

$$U'_p = \frac{\epsilon_p}{\epsilon_e} U'_\gamma \quad . \quad (6.3)$$

Here, ϵ_p and ϵ_e are the fraction of the total jet energy carried by protons and electrons, respectively. These energy fractions as well as ϵ_B are considered to be of the order of 0.1, taken from Refs. [204, 207]. As for the proton spectrum in GRBs, we assume that protons have a spectrum of the form $\propto E^{-\alpha_p}$, extending up to a maximal energy, see Eq. (2.1). With the size of the jet known as well as the value of the magnetic field B' , we can self-consistently derive the maximal proton energy $E'_{p,\max}$, similar to Eq. (2.31).¹ With $E'_{p,\max}$ known, the normalization of the proton spectrum can be obtained as for the photon spectrum in Eq. (6.2).

As stated before, the parameters of Cyg X-3 are quite well documented, especially compared to those of a GRB. For our calculations, we adopt the following parameters of the source:

$$\begin{aligned} d_L &= 7.2 \text{ kpc} \quad , \\ \mathcal{D} &= 2.74 \quad , \\ \theta_j &= 12^\circ \quad , \\ l &= 10^8 \text{ cm} \quad . \end{aligned}$$

The value of the distance d_L is taken from Ref. [208]. The Doppler factor \mathcal{D} is calculated from the Lorentz factor $\Gamma = 1.70$ (from radio observations) and the viewing angle $\theta = 14^\circ$, as described in Refs. [207, 209]. The jet opening angle θ_j was also taken from Ref. [209]. In contrast to these previous parameters, the distance l from the central engine is not the result of an observation, but an assumption taken from Ref. [204]. This is due to the lack of spectroscopic measurements in wavelengths shorter than radio. Hence, l is the parameter which introduces the largest uncertainty on the neutrino flux prediction, as it could be significantly different from the assumed value of 10^8 cm. Nonetheless, with the parameters above, we can use Eq. (2.3) to estimate what the needed energy in photons is to interact with protons with an observed² energy $E_p = 10^8$ GeV. For said energy, we can derive that X-ray photons with several keV energy are needed. This is one important difference to GRBs, since for GRBs the gamma-rays are assumed to be the relevant target photons in internal shocks. However, due to the lower boost factors, the target photons needed in case of MQs are of considerably lower energy in the observer's frame. In the SRF, the needed photon energies are nonetheless comparable for MQs and GRBs, with values of $\mathcal{O}(\text{keV})$. For this reason, we use the different X-ray states of Cyg X-3 from Ref. [210], with special emphasis on the so-called hypersoft state, which is assumed to be associated with gamma-ray flares detected from Cyg X-3, see discussion in Refs. [211, 212, 213]. Based on the hypersoft state from Ref. [210],

¹In the example discussed here, we only consider synchrotron and adiabatic losses for the maximal energy. However, depending on the photon and the proton density, also $p\gamma$ - as well as pp -interactions could limit $E'_{p,\max}$.

²For galactic sources, we do not have the adiabatic energy loss due to the expansion of the universe and the distances are much shorter than the interaction length for interactions with cosmic background fields (for $E_p = 10^8$ GeV), compare to Fig. 4.1. The magnetic field inside our galaxy is significantly higher than the intergalactic magnetic field, but for the sake of simplicity we will neglect this, since we are only interested in the needed photons for photohadronic interactions.

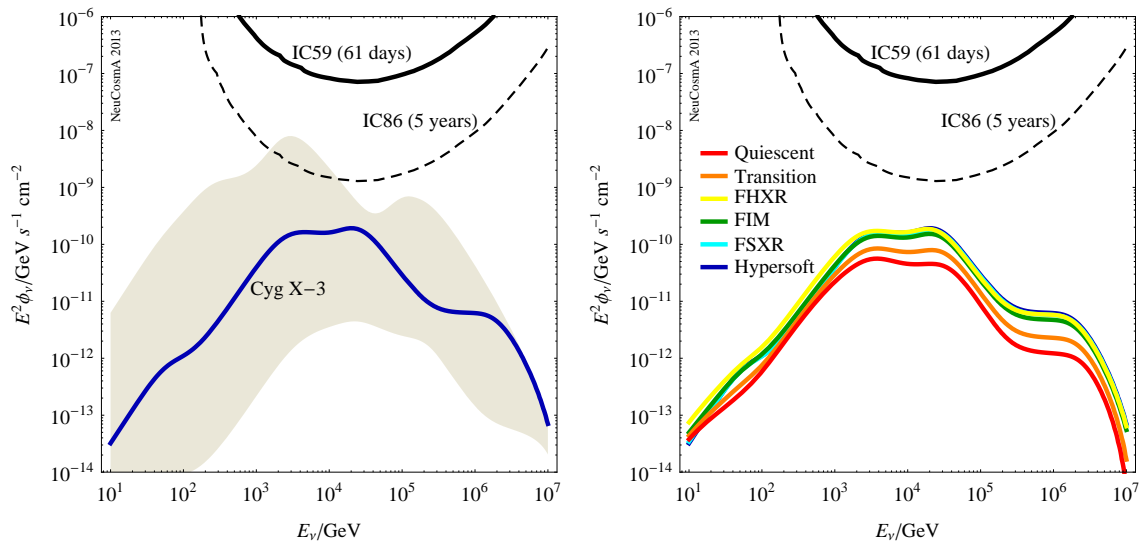


Figure 6.1.: In the left plot, we show the muon neutrino (and antineutrino) flux prediction for Cyg X-3 based on the hypersoft state from Ref. [210]. While the solid blue curve depicts the nominal prediction for an assumed distance from the central object $l = 10^8$ cm, the gray-shaded area represents the uncertainty induced by varying l by one order of magnitude up or down. The right plot depicts the neutrino flux predictions for the different flux states from Ref. [210] (see legend inside plot). The variation between the highest neutrino flux prediction (for hypersoft state) to the lowest prediction (for quiescent state) is only of the order of two, and much smaller than the variation due to the uncertainty on l . For comparison reasons, the (extrapolated) differential flux limits for two experimental setups are included in both plots (see labels in plots). The differential limits are based on the solid-angle-averaged effective areas at final cut level of the time-integrated point-like source search from Ref. [214]. Plots taken from Ref. [154].

we obtain $L_\gamma = 3.77 \cdot 10^{37}$ erg s $^{-1}$ (integrated over range from 3.5 up to 102 keV), $B' = 8.8 \cdot 10^5$ G, and $E'_{p,\max} = 5.5 \cdot 10^7$ GeV.

Using the aforementioned simplistic jet model for MQs together with our photo-hadronic interaction code, we can calculate the muon neutrino (and antineutrino) flux prediction for the hypersoft state of Cyg X-3. As can be seen from Fig. 6.1, the flux shape is similar to the one for GRBs, which is a consequence of the similar model and magnetic fields. An important difference compared to the prediction for GRBs is that the peak of the neutrino flux prediction is no longer between 10^5 and 10^7 GeV, but now between 10^3 and 10^5 GeV. In this energy range, the atmospheric neutrino background is higher, but still manageable. We can estimate that the IceCube point source neutrino flux limits of the full detector start to probe this type of neutrino flux after a few years, as detailed in Ref. [154] and can be seen from the estimated 5 yr IC86 limit (dashed black curve) in Fig. 6.1. The (extrapolated) neutrino flux limits depicted in Fig. 6.1 are based on the declination band for $\delta = (30^\circ, 60^\circ)$ of the solid-angle-averaged effective areas at final cut level of the time-integrated point-like source search from Ref. [214], since a declination of $\delta = 40^\circ 57'$ is given for Cyg X-3. The result shown in Fig. 6.1 is somewhat reassuring as the neutrino flux predictions are sufficiently below the IC59 flux limit (solid black curve) to be consistent with current point source searches by IceCube [215]. However, with the improved cuts based in flares, suggested in Ref. [215], it should be possible to actually probe this type of

emission model for MQs. It actually helps that the variation among different (X-ray) flux states, which is shown in the right plot of Fig. 6.1, is only of the order of two as long as the distance to the central engine l is fixed. When said distance, which is the equivalent to the collision radius R_c from the internal shock GRB fireball model, is varied, then the neutrino flux prediction is strongly affected, see shaded area in left plot of Fig. 6.1. An additional test which can be applied for photohadronic interactions is to compare the observed gamma-rays to the predicted amount of energy released by π^0 -decay, as in Eq. (2.13). As we have described in Ref. [154], it is possible to estimate that we would have already expected a neutrino signal in Ice-Cube, if gamma-ray flares detected by *AGILE* [213] were induced by π^0 -decays from photohadronic interactions. This conclusion is obtained from energy conservation arguments in the range of the gamma-rays. This (multi-messenger) result has two important consequences: The first consequence is that the simple jet model for MQs is not sufficient for a realistic description of all observations from Cyg X-3. This was to be expected as the used jet model does not include a self-consistent calculation of the photon spectrum. Other models to describe the gamma-ray emission are either Inverse Compton scattering, as suggested in Ref. [216], or pp -collisions, as in Refs. [217, 218].³ Especially, the pp -interaction models are quite popular as they are closer to AGN. There has already been a quite detailed study on neutrinos from MQs in case of pp -interactions by Romero and Reynoso [143], which also includes similar effects from magnetic fields as obtained from our analysis. The second, and more basic, consequence is that this result proves (again) that multi-messenger approaches are very well suited to obtain stronger bounds on models in general. Even though we used a model which was originally designed for GRBs, and only slightly adapted it, we were able to obtain neutrino predictions for a MQ, Cyg X-3.

³Note that it was pointed out in Ref. [219] that there is a mistake in the boost factors in Ref. [217]. This needs to be considered for accurate calculations.

7. Summary and conclusions

We are currently living through great times for multi-messenger astrophysics and, especially, neutrino astrophysics, with advances on the technological side through $\mathcal{O}(\text{km}^3)$ -neutrino telescopes, such as IceCube or the up-coming KM3NeT, and the first detection of cosmic neutrinos, see Refs. [12, 13]. With this progress on the experimental side, it is now time again for the theoretical calculations to catch up. One of the prime examples for this are the models for cosmic ray acceleration in GRBs. Different approaches have started to rule out certain internal shock fireball models as the sole sources of UHECR, either based on the observation in gamma-rays [135], or through the “one neutrino per cosmic ray”-paradigm [161]. During the progress of this thesis, we have shown that the aforementioned results are actually weaker than initially thought or that it is possible to circumvent certain constraints.

We started our calculations by introducing an efficient way to calculate the neutrino spectra from individual GRBs based on the photohadronic interactions involved in the neutrino production. Our approach is based on a semi-analytical approximation of the $p\gamma$ interaction cross section, model Sim-B from Ref. [139], which is able to reproduce the photohadronic interaction results gained with the Monte-Carlo-code SOPHIA [131]. Our numerical approach allows for an individual treatment of secondary particles (including losses on the secondaries), magnetic field effects, helicity-dependent muon decays, and neutrino mixing during propagation, see Refs. [139, 142]. Based on this treatment of the particle physics, we could show that the neutrino flux shape changes from a plateau (Waxman-Bahcall spectrum [122, 123]) to a double peak with a high-energy component from kaon decays, see discussion in chapter 2. In a next step, we applied the numerical model to the IC40 GRB analysis, and showed that the (re-calculated) neutrino flux prediction is actually one order of magnitude lower than initially thought [136], which was independently confirmed by other groups, see Refs. [137, 138]. Additionally, we discussed the uncertainties introduced by using fixed “standard burst parameters” as well as the statistical uncertainty from extrapolating to a quasi-diffuse flux limit [107]. Especially, the uncertainty on the parameters can affect the nominal flux prediction by orders of magnitude, with the Lorentz factor Γ having the greatest effect on the normalization. Unfortunately, the Lorentz factor is one of the hardest to obtain parameters of a GRB, and current predictions based on observational data will always suffer from this uncertainty. A recent consequence of the aforementioned work is the current ANTARES GRB analysis, for which we provided the neutrino flux prediction using our NeuCosmA code and helping adapt the search strategy based on said prediction [153].

In chapter 3, we addressed the additional constraint which arises from the connection of cosmic ray and neutrino escape from a GRB. We discussed, that we can

identify three distinct CR escape regimes based on a microphysics treatment of escape [152]. We showed that the commonly used paradigm of one neutrino per cosmic ray [135, 161] holds only in the optically thin neutron escape regime. This regime is, however, limited to a small region of the parameter space, sandwiched between the direct escape regime (with more CRs than neutrinos) and the optically thick neutron escape regime (with more neutrinos than CRs). Additionally, we tested our CR escape model on four actually measured bursts, showing that the direct escape can play a role for actual bursts. Hence, the cosmic ray flux from a GRB could be enhanced due to this additional component, while the neutrinos would remain unchanged. Nonetheless, the accelerated protons must first of all reach at least the observed UHECR energies. For this, either a high acceleration efficiency, *e.g.* $\eta = 1$, is needed, or few bursts with specific parameters need to dominate.

To really quantify how many UHECR would actually reach us from a theoretical distribution of GRBs, we then used our photohadronic interaction code to create a simple large scale CR propagation code. In chapter 4, we first discussed the losses due to interactions with the cosmic background photon fields, namely the CMB and the CIB. For the propagation itself, we included an approach which describes the propagation with its losses as a Boltzmann equation, as proposed in Refs. [161, 162]. With this approach, we were able to simultaneously calculate the UHECR, the prompt GRB neutrinos, as well as the cosmogenic neutrinos. We could normalize the spectra by fitting our CR prediction to the publicly available HiRes UHECR data. Consistency checks comparing our cosmogenic neutrino prediction to previous predictions, such as from Ref. [183], confirmed the validity of our approach. Moreover, we tested two scenarios of the cosmic ray escape: one with only the standard CR escape via neutrons, and a second one which included the direct escape of protons. We could show that the direct escape dominated model is, as opposed to the neutron escape model, not yet ruled out based on neutrino data. However, by normalizing to the HiRes UHECR data, we needed to increase the baryonic loading by about a factor of 40, which is somewhat in contrast to existing models. There are, nonetheless, still a lot of uncertainties regarding the parameters going into the model. One of our current projects is to test the viability of the approach when changing certain parameters or taking a different evolution in redshift [185]. Also, first simulations indicate that a change of the spectral proton index has a significant effect on the CR results. Therefore, more work in this regard needs to be done to better understand the underlying connections of multi-messenger observations.

As an additional possibility to extend our numerical calculation, we discussed the possibility of including neutrino lifetime effects in chapter 5. We tested a simple decay model of neutrinos into invisibles, without going into the details of the decay process. This effective treatment allowed us to focus on the effect the finite neutrino lifetime has on the neutrino spectra. First, we tested the general effect based on the decay of all three mass eigenstates. The surprising result was that the decay is always complete below a certain critical energy, which solely depends on the lifetime κ^{-1} of the neutrino mass eigenstates. These basic considerations, however, did not obey the current lifetime bounds set by the neutrino observation from SN1987A, which suggest that ν_1 is stable, while ν_2 and ν_3 can decay. Using this modified

scenario of stable ν_1 and decaying ν_2 and ν_3 , we discussed the effect of decay on the neutrino flux predictions, based on a single burst as well as the re-calculated quasi-diffuse flux prediction from the IC40 GRB sample [136]. We could derive that the muon and tau neutrino flux predictions get suppressed by about one order of magnitude. The electron neutrinos, however, were only slightly affected. As a result, the expected ratio of muon tracks to cascade events shifts towards the amount of cascades. We could show that the muon neutrino flux prediction could drop below the sensitivity of the full IceCube detector after ten years of operation, depending on the lifetime. However, cascade events would still give a significant signal. This approach obtained some justification, when the first neutrino events passing all background cuts were actually cascades [12]. However, newer results with lower energy data do not indicate an enhanced amount of cascades [13], which indicates that the discussed decay scenarios are not able to describe the observations. Even though decay is now again not likely, it is nonetheless a possibility to resolve the constraints on GRB neutrino data coming from the normalization to the UHECR. As for the additional cosmic ray component, decay would change the relative level of CRs to neutrinos, breaking the paradigm of one neutrino per cosmic ray.

Finally, we showed that we can even apply similar calculations as in the GRB internal shock fireball model to different objects, such as microquasars. At the example of the MQ Cyg X-3, we showed how to calculate the neutrinos based on the observed X-rays. The predicted neutrino spectra for a simple internal shock scenario for MQ peak at a lower energy than the ones from GRBs, however, as MQs are galactic objects, it is more likely to obtain a signal from a single source. Still, as for GRBs, the predictions are subject to large uncertainties.

8. Outlook

On the base of what we described in this work regarding neutrino and cosmic ray production in GRBs, there are still numerous ways to further investigate the multi-messenger connection, and GRBs in general. We only briefly touched the subject of the different correction factors going into the calculations in chapter 4. We still need to test, how a different distribution in redshift affects the prediction [185]. For example, a strong evolution as proposed by Kistler et al. leads to a high value of f_z , while the prediction for a pure SFR would be significantly lower. If there are more bursts at low redshift, these would have to contribute less on average than in the strong evolution case, and the needed baryonic loading f_e^{-1} would be lower as well. Then, there are always ways to tweak the parameters of the bursts to somehow still be viable. We therefore need to start excluding parameter space regions based on the available data, such as combining the bounds on prompt GRB neutrinos, cosmogenic neutrinos, and UHECR to obtain exclusion limits. It would be nice to know if certain CR escape models such as the neutron escape model are really ruled out already for this (simple) internal shock fireball model. Also, we have so far only distributed the GRBs in redshift, while a distribution in several, if not all, other parameters is more realistic. As opposed to, *e.g.*, type Ia SN [220], GRBs are no standard candles, and have large variation among their parameters. This variation among the parameters can introduce additional unexpected effects such as the luminosity distribution has on the effective cosmic ray index, as discussed in Ref. [221]. Still, in the future, we can expect to have more data on GRBs, be it through more data from satellites or new techniques, such as detection of afterglows in the radio band [222], which will additionally improve neutrino predictions.

Apart from the on-going work on the different aspects which affect the CR propagation, there are also several possible aspects of the individual burst that need to be discussed in the future. For one, it is known from observations that the GRB light curves are violently varying. Hence, even though the approximation of using time-averaged quantities is justified by the statistically limited neutrino detection rate, a more realistic model would be to include these variations also in the neutrino flux calculations. One approach for this could be to treat the individual collisions of two shells as a burst of its own and calculate the neutrino spectra on a collision basis. Similar models, used to create artificial light curves, already exist, see, *e.g.*, Refs. [39, 149]. These would have to be adapted to give the photon and proton spectra for each collision, and then using our photohadronic interaction code to calculate the neutrino spectra for each collision. Of course, a drawback of this more detailed model will be that the simulation of a single burst will take much longer compared to the simple time-averaged model. The result should, however, be closer to reality. Also, this approach would allow for a discussion of the connection of the active time of the engine (which emits the shells) and the observed duration of a

burst (which is a result of the collisions), similar to the discussion in Ref. [223]. The higher luminosities over shorter timescales could actually help to improve the cuts in the neutrino searches. That is, whatsoever, assuming that there are no Lorentz violation effects or any other additional processes happening during propagation. Also, it would give a first possibility to also include a photon prediction into the analyses, together with the prompt neutrinos, cosmogenic neutrinos, and UHECR. As a goal for the (maybe distant) future, a full magnetohydrodynamical simulation of the jet of a GRB, including the calculation of neutrinos, cosmic rays, and photons, would be useful. Currently, these types of simulations are being developed for AGN. An application to GRBs is as of now still hindered by the high Lorentz factors Γ of GRBs. Based on the progress in simulations of SN, binary mergers, and jet simulations, this should nonetheless be possible in the future.

Moreover, one could also apply our photohadronic interaction code to other GRB models, such as photospheric models or magnetic reconnection models. As analytical estimates have shown, each model should have a different signal, see Ref. [68]. A more detailed study, similar to our work on the effects in the internal shock model, see Refs. [82, 136], would give insight on how these different scenarios could be distinguished using data from a neutrino telescope. There has been a recent work by Asano and Meszaros [224] on the photon and neutrino spectra of time-dependent photospheric models, which could be extended similar to the models for the artificial light curves in the internal shock model. It might also be interesting to model the different stages of a GRB, such as an acceleration phase similar to a choked GRB, as in, *e.g.*, Ref. [225], a decoupling phase similar to the photospheric models, a coasting phase with internal shocks, and then a final phase when the ejecta start to collide with the external medium. In general, more observational data on GRBs is needed. Currently we just do not know enough about these events to really prefer one model over the other. An additional advantage would be that the uncertainty due to the standard burst parameters would shrink, which in turn would help to clarify if a model is ruled out or not.

Furthermore, it may even be possible to apply the photohadronic interactions to other source classes (instead of applying other types of simulations to GRBs). For example, AGN and MQs are also interesting sources with respect to cosmic ray acceleration and neutrino astronomy. For AGN, detailed numerical models of the jets are needed, as for these the jet structures can be resolved. On the other hand, for MQs it might be sufficient to also apply an internal shock model, similar to the one used for GRBs. As we showed in the context of the microquasar Cygnus X-3, it is possible to obtain similar neutrino flux predictions from the X-ray data of the MQs (assuming the internal shock model is applicable for MQs), see Ref. [154]. Apart from that, it might also be interesting to have a code similar to the photohadronics treatment in NeuCosmA for pp -interactions. Proton-proton collisions are thought to be the main source of pion production in AGN jets. Hence, depending on the jet composition, they may also apply to GRBs. Moreover, our results for the baryonic loading needed to fit the UHECR data indicate a higher baryon amount inside the jet than initially thought. Therefore, pp -interactions would gain importance, if the values we obtained are applicable to real bursts. Based on LHCf data, see, *e.g.*, Ref. [226],

it should be possible to write a similar code for these complimentary interactions. With such a code it should even be possible to test how the relative contribution of neutrinos from pp -collisions is compared to those from $p\gamma$ -interactions.

In the end, the ultimate goal of multi-messenger physics remains to obtain a consistent model containing all the different messengers, for either a certain source or even a source class. Thanks to the detection of the first cosmic high-energy neutrinos, we will (hopefully) soon gain more insight on the different objects in space and what processes are relevant for them. And finally, it might even be possible to solve the 100 year old question “Where do UHECR come from?”.

Bibliography

- [1] V. Hess, *Physikalische Zeitschrift* **13**, 1084 (1912).
- [2] S. P. Swordy, *Space Sci. Rev.* **99**, 85 (2001).
- [3] K. Greisen, *Phys. Rev. Lett.* **16**, 748 (1966).
- [4] G. Zatsepin and V. Kuzmin, *JETP Lett.* **4**, 78 (1966).
- [5] T. K. Gaisser, T. Stanev, and S. Tilav, *Frontiers of Physics* (2013), arXiv:1303.3565.
- [6] A. M. Hillas, *Ann. Rev. Astron. Astrophys.* **22**, 425 (1984).
- [7] W. Hanlon, <http://www.physics.utah.edu/~whanlon/spectrum.html>.
- [8] K. Hirata *et al.*, *Phys. Rev. Lett.* **58**, 1490 (1987).
- [9] R. Bionta *et al.*, *Phys. Rev. Lett.* **58**, 1494 (1987).
- [10] T. K. Gaisser, *Cosmic Rays and Particle Physics* (Cambridge University Press, 1991).
- [11] S. Ando *et al.*, (2012), arXiv:1203.5192.
- [12] IceCube Collaboration, M. Aartsen *et al.*, *Phys. Rev. Lett.* **111**, 021103 (2013), arXiv:1304.5356.
- [13] IceCube Collaboration, N. Whitehorn, C. Kopper, and N. Neilson, *Results from icecube, talks given at the IceCube Particle Astrophysics Symposium (IPA) 2013, Madison, WI, USA, 2013.*
- [14] ANTARES Collaboration, M. Ageron *et al.*, *Nucl.Instrum.Meth.* **A656**, 11 (2011), arXiv:1104.1607.
- [15] IceCube, J. Ahrens *et al.*, *Nucl. Phys. Proc. Suppl.* **118**, 388 (2003), astro-ph/0209556.
- [16] I. Cholis and D. Hooper, *JCAP* **06**, 030 (2013), arXiv:1211.1974.
- [17] H.-N. He, T. Wang, Y.-Z. Fan, S.-M. Liu, and D.-M. Wei, *Phys. Rev.* **D87**, 063011 (2013), arXiv:1303.1253.
- [18] R. Laha, J. F. Beacom, B. Dasgupta, S. Horiuchi, and K. Murase, *Phys. Rev.* **D88**, 043009 (2013), arXiv:1306.2309.
- [19] K. Murase, M. Ahlers, and B. C. Lacki, (2013), arXiv:1306.3417.
- [20] L. A. Anchordoqui *et al.*, (2013), arXiv:1306.5021.

- [21] D. Fox, K. Kashiyama, and P. Mészáros, *Astrophys. J.* **774**, 74 (2013), arXiv:1305.6606.
- [22] O. E. Kalashev, A. Kusenko, and W. Essey, *Phys.Rev.Lett.* **111**, 041103 (2013), arXiv:1303.0300.
- [23] F. W. Stecker, *Phys. Rev.* **D88**, 047301 (2013), arXiv:1305.7404.
- [24] H.-N. He, R.-Z. Yang, Y.-Z. Fan, and D.-M. Wei, (2013), arXiv:1307.1450.
- [25] W. Winter, (2013), arXiv:1307.2793.
- [26] A. Neronov, D. Semikoz, and C. Tchernin, (2013), arXiv:1307.2158.
- [27] E. Roulet, G. Sigl, A. van Vliet, and S. Mollerach, *JCAP* **1301**, 028 (2013), arXiv:1209.4033.
- [28] P. Lipari, (2013), arXiv:1308.2086.
- [29] R. W. Klebesadel, I. B. Strong, and R. A. Olson, *Astrophys. J.* **182**, L85 (1973).
- [30] J. Hjorth *et al.*, *Nature* **423**, 847 (2003), arXiv:astro-ph/0306347.
- [31] K. Z. Stanek *et al.*, *Astrophys. J.* **591**, L17 (2003), arXiv:astro-ph/0304173.
- [32] J. Hjorth *et al.*, *Nature* **437**, 859 (2005), arXiv:astro-ph/0510096.
- [33] A. Nicuesa Guelbenzu *et al.*, *Astron. & Astrophys.* **548**, A101 (2012), arXiv:1206.1806.
- [34] T. Laskar *et al.*, (2013), arXiv:1307.6586.
- [35] B. Paczynski, *Astrophys. J.* **308**, L43 (1986).
- [36] P. Meszaros and M. Rees, *Astrophys. J.* **405**, 278 (1993).
- [37] S. E. Woosley, *Astrophys. J.* **405**, 273 (1993).
- [38] R. Sari and T. Piran, *Astrophys. J.* **485**, 270 (1997), arXiv:astro-ph/9701002.
- [39] S. Kobayashi, T. Piran, and R. Sari, *Astrophys. J.* **490**, 92 (1997), arXiv:astro-ph/9705013.
- [40] M. J. Rees and P. Meszaros, *Astrophys. J.* **430**, L93 (1994), arXiv:astro-ph/9404038.
- [41] T. Piran, *Rev. Mod. Phys.* **76**, 1143 (2004), arXiv:astro-ph/0405503.
- [42] P. Meszaros, *Rept. Prog. Phys.* **69**, 2259 (2006), arXiv:astro-ph/0605208.
- [43] M. Ruderman, Theories of gamma-ray bursts, in *Seventh Texas Symposium on Relativistic Astrophysics*, edited by P. G. Bergman, E. J. Fenyves, and L. Motz, *Annals of the New York Academy of Sciences* Vol. 262, pp. 164–180, 1975.
- [44] G. J. Fishman and C. A. Meegan, *Ann. Rev. Astron. Astrophys.* **33**, 415 (1995).

-
- [45] E. E. Fenimore *et al.*, *Nature* **366**, 40 (1993).
- [46] M. J. Rees, *Nature* **211**, 468 (1966).
- [47] <http://fermi.gsfc.nasa.gov/>.
- [48] E. Costa *et al.*, *Nature* **387**, 783 (1997), arXiv:astro-ph/9706065.
- [49] J. van Paradijs *et al.*, *Nature* **386**, 686 (1997).
- [50] M. R. Metzger *et al.*, *Nature* **387**, 878 (1997).
- [51] S. R. Kulkarni *et al.*, *Nature* **393**, 35 (1998).
- [52] S. D. Barthelmy *et al.*, *Space Sci. Rev.* **120**, 143 (2005).
- [53] A. Cucchiara *et al.*, *Astrophys. J.* **736**, 7 (2011), arXiv:1105.4915.
- [54] D. Guetta, E. Pian, and E. Waxman, *Astron. & Astrophys.* **525**, A53 (2011), arXiv:1003.0566.
- [55] W. Atwood *et al.*, *Astrophys. J.* **774**, 76 (2013), arXiv:1307.3037.
- [56] A. I. MacFadyen and S. E. Woosley, *Astrophys. J.* **524**, 262 (1999), arXiv:astro-ph/9810274.
- [57] D. Eichler, M. Livio, T. Piran, and D. N. Schramm, *Nature* **340**, 126 (1989).
- [58] R. Narayan, B. Paczynski, and T. Piran, *Astrophys. J.* **395**, L83 (1992), arXiv:astro-ph/9204001.
- [59] C. Kouveliotou *et al.*, *Astrophys. J.* **413**, L101 (1993).
- [60] W. Paciesas *et al.*, *Astrophys. J. Suppl.* **122**, 465 (1999), arXiv:astro-ph/9903205.
- [61] T. Sakamoto *et al.*, *Astrophys. J. Suppl.* **195**, 2 (2011), arXiv:1104.4689.
- [62] T. Piran, A. Shemi, and R. Narayan, *Mon. Not. Roy. Astron. Soc.* **263**, 861 (1993), arXiv:astro-ph/9301004.
- [63] P. Meszaros, P. Laguna, and M. Rees, *Astrophys. J.* **415**, 181 (1993), arXiv:astro-ph/9301007.
- [64] I. Vurm, A. M. Beloborodov, and J. Poutanen, *Astrophys. J.* **738**, 77 (2011), arXiv:1104.0394.
- [65] Fermi-LAT Collaboration, Fermi-GBM Collaboration, Swift Collaboration, GROND Collaboration, MOA Collaboration, M. Ackermann *et al.*, *Astrophys. J.* **763**, 71 (2013), arXiv:1212.0973.
- [66] S. Gao, K. Asano, and P. Meszaros, *JCAP* **1211**, 058 (2012), arXiv:1210.1186.
- [67] B. Zhang and H. Yan, *Astrophys. J.* **726**, 90 (2011), arXiv:1011.1197.
- [68] B. Zhang and P. Kumar, *Phys. Rev. Lett.* **110**, 121101 (2013), arXiv:1210.0647.

- [69] E. Waxman, *Lect. Notes Phys.* **598**, 393 (2003), arXiv:astro-ph/0303517.
- [70] D. Guetta, D. Hooper, J. Alvarez-Muniz, F. Halzen, and E. Reuveni, *Astropart. Phys.* **20**, 429 (2004), arXiv:astro-ph/0302524.
- [71] F. Halzen, *ArXiv Astrophysics e-prints* (1998), arXiv:astro-ph/9810368.
- [72] G. A. MacLachlan *et al.*, *Mon. Not. Roy. Astron. Soc.* **432**, 857 (2013), arXiv:1201.4431.
- [73] J. K. Becker, M. Stamatikos, F. Halzen, and W. Rhode, *Astropart. Phys.* **25**, 118 (2006), arXiv:astro-ph/0511785.
- [74] Y. Lithwick and R. Sari, *Astrophys. J.* **555**, 540 (2001), arXiv:astro-ph/0011508.
- [75] S. Razzaque, P. Meszaros, and B. Zhang, *Astrophys. J.* **613**, 1072 (2004), arXiv:astro-ph/0404076.
- [76] R. Sari and T. Piran, *Astrophys. J.* **520**, 641 (1999), arXiv:astro-ph/9901338.
- [77] Y.-C. Zou and T. Piran, *Mon. Not. Roy. Astron. Soc.* **402**, 1854 (2010), arXiv:0908.4418.
- [78] J. Lu *et al.*, *Astrophys. J.* **751**, 49 (2012), arXiv:1109.3757.
- [79] M. Cohen *et al.*, *Astrophys. J.* **658**, 232 (2007), arXiv:astro-ph/0611642.
- [80] D. Band *et al.*, *Astrophys. J.* **413**, 281 (1993).
- [81] K. Murase and S. Nagataki, *Phys. Rev.* **D73**, 063002 (2006), arXiv:astro-ph/0512275.
- [82] P. Baerwald, S. Hümmer, and W. Winter, *Phys. Rev.* **D83**, 067303 (2011), arXiv:1009.4010.
- [83] D. L. Freedman and E. Waxman, *Astrophys. J.* **547**, 922 (2001), arXiv:astro-ph/9912214.
- [84] R. Santana, R. B. Duran, and P. Kumar, (2013), arXiv:1309.3277.
- [85] A. M. Hopkins and J. F. Beacom, *Astrophys. J.* **651**, 142 (2006), arXiv:astro-ph/0601463.
- [86] I. K. Baldry and K. Glazebrook, *Astrophys. J.* **593**, 258 (2003), arXiv:astro-ph/0304423.
- [87] M. D. Kistler, H. Yüksel, J. F. Beacom, A. M. Hopkins, and J. S. B. Wyithe, *Astrophys. J.* **705**, L104 (2009), arXiv:0906.0590.
- [88] W. Pauli, *Phys. Today* **31N9**, 27 (1978).
- [89] E. Fermi, *Zeitschrift für Physik A Hadrons and Nuclei* **88**, 161 (1934), 10.1007/BF01351864.
- [90] C. L. Cowan, F. Reines, F. B. Harrison, H. W. Kruse, and A. D. McGuire, *Science* **124**, 103 (1956), <http://www.sciencemag.org/content/124/3212/103.full.pdf>.

-
- [91] G. Danby *et al.*, Phys. Rev. Lett. **9**, 36 (1962).
- [92] K. Kodama *et al.*, Phys. Lett. **B504**, 218 (2001).
- [93] C. Wu, E. Ambler, R. Hayward, D. Hoppes, and R. Hudson, Phys. Rev. **105**, 1413 (1957).
- [94] M. Goldhaber, L. Grodzins, and A. Sunyar, Phys. Rev. **109**, 1015 (1958).
- [95] B. Pontecorvo, Soviet Journal of Experimental and Theoretical Physics **6**, 429 (1958).
- [96] B. Pontecorvo, Soviet Journal of Experimental and Theoretical Physics **26**, 984 (1968).
- [97] N. Cabibbo, Phys. Rev. Lett. **10**, 531 (1963).
- [98] Z. Maki, M. Nakagawa, and S. Sakata, Prog. Theor. Phys. **28**, 870 (1962).
- [99] C. Giunti and C. W. Kim, Found. Phys. Lett. **14**, 213 (2001), arXiv:hep-ph/0011074.
- [100] Planck Collaboration, P. Ade *et al.*, (2013), arXiv:1303.5062.
- [101] Particle Data Group, J. Beringer *et al.*, Phys. Rev. **D86**, 010001 (2012).
- [102] LSND Collaboration, A. Aguilar-Arevalo *et al.*, Phys. Rev. **D64**, 112007 (2001), arXiv:hep-ex/0104049.
- [103] DAYA-BAY Collaboration, F. An *et al.*, Phys. Rev. Lett. **108**, 171803 (2012), arXiv:1203.1669.
- [104] RENO collaboration, J. Ahn *et al.*, Phys. Rev. Lett. **108**, 191802 (2012), arXiv:1204.0626.
- [105] Double Chooz Collaboration, Y. Abe *et al.*, Phys. Rev. **D86**, 052008 (2012).
- [106] G. Fogli *et al.*, Phys. Rev. **D86**, 013012 (2012), arXiv:1205.5254.
- [107] P. Baerwald, S. Hümmer, and W. Winter, Astropart. Phys. **35**, 508 (2012), arXiv:1107.5583.
- [108] M. Maltoni and W. Winter, JHEP **07**, 064 (2008), arXiv:0803.2050.
- [109] J. G. Learned and K. Mannheim, Ann. Rev. Nucl. Part. Sci. **50**, 679 (2000).
- [110] IceCube Collaboration, M. Aartsen *et al.*, (2013), arXiv:1305.6811.
- [111] Antares Collaboration, S. Adrian-Martinez *et al.*, Astrophys. J. **743**, L14 (2011), arXiv:1108.0292.
- [112] J. F. Beacom, N. F. Bell, D. Hooper, S. Pakvasa, and T. J. Weiler, Phys. Rev. **D68**, 093005 (2003), arXiv:hep-ph/0307025.
- [113] P. Miocinovic *et al.*, Tuning into UHE Neutrinos in Antarctica - The ANITA Experiment, in *22nd Texas Symposium on Relativistic Astrophysics*, edited by P. Chen, E. Bloom, G. Madejski, and V. Patrosian, pp. 765–770, 2005, arXiv:astro-ph/0503304.

- [114] A. Vieregg *et al.*, *Astrophys. J.* **736**, 50 (2011), arXiv:1102.3206.
- [115] RICE Collaboration, I. Kravchenko *et al.*, *Astropart. Phys.* **19**, 15 (2003), arXiv:astro-ph/0112372.
- [116] S. Razzaque, J. A. Adams, P. Harris, and D. Besson, *Astropart. Phys.* **26**, 367 (2007), arXiv:astro-ph/0605480.
- [117] P. Allison *et al.*, *Astropart. Phys.* **35**, 457 (2012), arXiv:1105.2854.
- [118] W. Winter, *Nucl. Phys. Proc. Suppl.* **203-204**, 45 (2010), arXiv:1004.4160.
- [119] P. D. Serpico and M. Kachelriess, *Phys. Rev. Lett.* **94**, 211102 (2005), arXiv:hep-ph/0502088.
- [120] K.-C. Lai, G.-L. Lin, and T.-C. Liu, (2013), arXiv:1308.1828.
- [121] S. Pakvasa, *Mod. Phys. Lett.* **A23**, 1313 (2008), arXiv:0803.1701.
- [122] E. Waxman and J. N. Bahcall, *Phys. Rev. Lett.* **78**, 2292 (1997), arXiv:astro-ph/9701231.
- [123] E. Waxman and J. N. Bahcall, *Phys. Rev.* **D59**, 023002 (1999), arXiv:hep-ph/9807282.
- [124] P. Lipari, M. Lusignoli, and D. Meloni, *Phys. Rev.* **D75**, 123005 (2007), arXiv:0704.0718.
- [125] E. Waxman, *Nucl. Phys. Proc. Suppl.* **118**, 353 (2003), arXiv:astro-ph/0211358.
- [126] A. Achterberg, Y. A. Gallant, J. G. Kirk, and A. W. Guthmann, *Mon. Not. Roy. Astron. Soc.* **328**, 393 (2001), arXiv:astro-ph/0107530.
- [127] W. Apel *et al.*, *Astropart. Phys.* **47**, 54 (2013), arXiv:1306.6283.
- [128] F. Stecker and M. Salamon, *Astrophys. J.* **512**, 521 (1999), arXiv:astro-ph/9808110.
- [129] R.-Y. Liu, A. Taylor, M. Lemoine, X.-Y. Wang, and E. Waxman, (2013), arXiv:1308.5699.
- [130] K. Mannheim, R. Protheroe, and J. P. Rachen, *Phys. Rev.* **D63**, 023003 (2001), arXiv:astro-ph/9812398.
- [131] A. Mücke, R. Engel, J. P. Rachen, R. J. Protheroe, and T. Stanev, *Comput. Phys. Commun.* **124**, 290 (2000), arXiv:astro-ph/9903478.
- [132] A. Mücke, J. P. Rachen, R. Engel, R. J. Protheroe, and T. Stanev, *Nucl. Phys. B Proc. Suppl.* **80**, C810 (2000), arXiv:astro-ph/9905153.
- [133] IceCube, R. Abbasi *et al.*, *Astrophys. J.* **710**, 346 (2010), arXiv:0907.2227.
- [134] IceCube Collaboration, R. Abbasi *et al.*, *Phys. Rev. Lett.* **106**, 141101 (2011), arXiv:1101.1448.

-
- [135] IceCube Collaboration, R. Abbasi *et al.*, Nature **484**, 351 (2012), arXiv:1204.4219.
- [136] S. Hümmer, P. Baerwald, and W. Winter, Phys. Rev. Lett. **108**, 231101 (2012), arXiv:1112.1076.
- [137] H.-N. He *et al.*, Astrophys. J. **752**, 29 (2012), arXiv:1204.0857.
- [138] Z. Li, Phys. Rev. **D85**, 027301 (2012), arXiv:1112.2240.
- [139] S. Hümmer, M. Rügner, F. Spanier, and W. Winter, Astrophys. J. **721**, 630 (2010), arXiv:1002.1310.
- [140] R. Moharana and N. Gupta, Astropart. Phys. **36**, 195 (2012), arXiv:1107.4483.
- [141] K. Nakamura and P. D. Group, Journal of Physics G: Nuclear and Particle Physics **37**, 075021 (2010).
- [142] S. Hümmer, M. Maltoni, W. Winter, and C. Yaguna, Astropart. Phys. **34**, 205 (2010), arXiv:1007.0006.
- [143] M. M. Reynoso and G. E. Romero, Astron. & Astrophys. **493**, 1 (2009), arXiv:0811.1383.
- [144] K. Mannheim and P. L. Biermann, Astron. & Astrophys. **221**, 211 (1989).
- [145] S. R. Kelner and F. A. Aharonian, Phys. Rev. **D78**, 034013 (2008), arXiv:0803.0688.
- [146] S. Kelner, F. A. Aharonian, and V. Bugayov, Phys. Rev. **D74**, 034018 (2006), arXiv:astro-ph/0606058.
- [147] Pierre Auger, J. Abraham *et al.*, Phys. Rev. **D79**, 102001 (2009), arXiv:0903.3385.
- [148] T. Kashti and E. Waxman, Phys. Rev. Lett. **95**, 181101 (2005), arXiv:astro-ph/0507599.
- [149] F. Daigne and R. Mochkovitch, Mon. Not. Roy. Astron. Soc. **296**, 275 (1998), arXiv:astro-ph/9801245.
- [150] M. V. Medvedev, Phys. Rev. **E67**, 045401 (2003), arXiv:astro-ph/0303271.
- [151] R. Schlickeiser, *Cosmic Ray Astrophysics* (Springer, 2002).
- [152] P. Baerwald, M. Bustamante, and W. Winter, Astrophys. J. **768**, 186 (2013), arXiv:1301.6163.
- [153] ANTARES Collaboration and P. Baerwald, S. Adrián-Martínez *et al.*, (2013), arXiv:1307.0304.
- [154] P. Baerwald and D. Guetta, Astrophys. J. **773**, 159 (2013), arXiv:1212.1457.
- [155] D. M. Coward *et al.*, Mon. Not. Roy. Astron. Soc. **432**, 2141 (2013), arXiv:1210.2488.

- [156] http://swift.gsfc.nasa.gov/archive/grb_table/fullview/.
- [157] D. Wanderman and T. Piran, *Mon. Not. Roy. Astron. Soc.* **406**, 1944 (2010), arXiv:0912.0709.
- [158] L. J. R. Lemos, C. Bianco, R. Ruffini, and M. Malheiro, (2013), arXiv:1309.3360.
- [159] S. Golenetskii *et al.*, GRB Coordinates Network **12362**, 1 (2011).
- [160] ANTARES Collaboration, S. Adrian-Martinez *et al.*, *JCAP* **1303**, 006 (2013), arXiv:1302.6750.
- [161] M. Ahlers, M. Gonzalez-Garcia, and F. Halzen, *Astropart. Phys.* **35**, 87 (2011), arXiv:1103.3421.
- [162] M. Ahlers, L. A. Anchordoqui, and S. Sarkar, *Phys. Rev.* **D79**, 083009 (2009), arXiv:0902.3993.
- [163] A. Pe'er and E. Waxman, *Astrophys. J.* **613**, 448 (2004), arXiv:astro-ph/0311252.
- [164] J. Kirk and P. Duffy, *J.Phys.* **G25**, R163 (1999), arXiv:astro-ph/9905069.
- [165] R. Ruffini, I. Siutsou, and G. Vereshchagin, *New Astronomy* **27**, 30 (2014), arXiv:1309.3857.
- [166] J. Lange and M. Pohl, *Astron. & Astrophys.* **551**, A89 (2013), arXiv:1301.2914.
- [167] F. Ryde *et al.*, *Astrophys. J.* **709**, L172 (2010), arXiv:0911.2025.
- [168] F. Ryde *et al.*, *Mon. Not. Roy. Astron. Soc.* **415**, 3693 (2011), arXiv:1103.0708.
- [169] L. Nava, G. Ghirlanda, G. Ghisellini, and A. Celotti, *Astron. & Astrophys.* **530**, A21 (2011), arXiv:1012.2863.
- [170] J. Greiner *et al.*, *Astron. & Astrophys.* **498**, 89 (2009), arXiv:0902.0761.
- [171] Fermi/GBM collaboration, Fermi/LAT Collaborations, Swift Team, A. Abdo *et al.*, *Astrophys. J.* **706**, L138 (2009), arXiv:0909.2470.
- [172] D. Gruber *et al.*, *Astron. & Astrophys.* **528**, A15 (2011), arXiv:1101.1099.
- [173] S. Hümmer, *Neutrinos aus photohadronischen Wechselwirkungen in kosmischen Beschleunigern (in German)*, PhD thesis, Würzburg University, 2013.
- [174] A. Franceschini, G. Rodighiero, and M. Vaccari, *Astron. & Astrophys.* **487**, 837 (2008), arXiv:0805.1841.
- [175] G. Blumenthal, *Phys. Rev.* **D1**, 1596 (1970).
- [176] M. J. Chodorowski, A. A. Zdziarski, and M. Sikora, *Astrophys. J.* **400**, 181 (1992).
- [177] P. Blasi, S. Burles, and A. V. Olinto, *Astrophys. J.* **514**, L79 (1999), arXiv:astro-ph/9812487.

-
- [178] A. Strong and I. Moskalenko, *Astrophys. J.* **509**, 212 (1998), arXiv:astro-ph/9807150.
- [179] K.-H. Kampert *et al.*, *Astropart. Phys.* **42**, 41 (2013), arXiv:1206.3132.
- [180] M. Schmidt, *Astrophys. J.* **523**, L117 (1999), arXiv:astro-ph/9908206.
- [181] M. Schmidt, *Astrophys. J.* **559**, L79 (2001), arXiv:astro-ph/0108459.
- [182] E. Waxman, *Astrophys. J.* **452**, L1 (1995), arXiv:astro-ph/9508037.
- [183] K. Kotera, D. Allard, and A. Olinto, *JCAP* **1010**, 013 (2010), arXiv:1009.1382.
- [184] HiRes, R. U. Abbasi *et al.*, *Phys. Rev. Lett.* **100**, 101101 (2008), arXiv:astro-ph/0703099.
- [185] M. Ahlers *et al.*, *In preparation* .
- [186] S. Pakvasa, Neutrino decays and neutrino telescopes, in *10th International Workshop on Neutrino Telescopes*, edited by M. Baldo-Ceolin, pp. 469–477, 2003, arXiv:hep-ph/0305317.
- [187] G. Raffelt, *Phys. Rev.* **D31**, 3002 (1985).
- [188] G. Gelmini and M. Roncadelli, *Phys. Lett.* **B99**, 411 (1981).
- [189] Y. Chikashige, R. N. Mohapatra, and R. Peccei, *Phys. Rev. Lett.* **45**, 1926 (1980).
- [190] R. Tomas, H. Pas, and J. Valle, *Phys. Rev.* **D64**, 095005 (2001), arXiv:hep-ph/0103017.
- [191] S.-L. Chen, X.-G. He, and H.-C. Tsai, *JHEP* **0711**, 010 (2007), arXiv:0707.0187.
- [192] S. Zhou, *Phys. Lett.* **B659**, 336 (2008), arXiv:0706.0302.
- [193] X.-Q. Li, Y. Liu, and Z.-T. Wei, *Eur.Phys.J.* **C56**, 97 (2008), arXiv:0707.2285.
- [194] D. Majumdar, *ArXiv e-prints* (2007), arXiv:0708.3485.
- [195] S. Pakvasa, A. Joshipura, and S. Mohanty, *Phys. Rev. Lett.* **110**, 171802 (2013), arXiv:1209.5630.
- [196] L. Dorame, O. Miranda, and J. Valle, (2013), arXiv:1303.4891.
- [197] P. Baerwald, M. Bustamante, and W. Winter, *JCAP* **1210**, 020 (2012), arXiv:1208.4600.
- [198] M. Blennow, T. Ohlsson, and W. Winter, *JHEP* **0506**, 049 (2005), arXiv:hep-ph/0502147.
- [199] A. S. Joshipura, E. Masso, and S. Mohanty, *Phys. Rev.* **D66**, 113008 (2002), arXiv:hep-ph/0203181.
- [200] A. Bandyopadhyay, S. Choubey, and S. Goswami, *Phys. Lett.* **B555**, 33 (2003), arXiv:hep-ph/0204173.

- [201] J. F. Beacom and N. F. Bell, Phys.Rev. **D65**, 113009 (2002), arXiv:hep-ph/0204111.
- [202] S. L. Glashow, Phys. Rev. **118**, 316 (1960).
- [203] IceCube Collaboration, A. Karle, IceCube, in *31st International Cosmic Ray Conference (ICRC 2009)*, 2010, arXiv:1003.5715.
- [204] A. Levinson and E. Waxman, Phys. Rev. Lett. **87**, 171101 (2001), arXiv:hep-ph/0106102.
- [205] I. Mirabel and L. Rodriguez, Ann. Rev. Astron. Astrophys. **37**, 409 (1999), arXiv:astro-ph/9902062.
- [206] R. Fender, Microquasars: Hard X-ray/ γ -ray emission, in *American Institute of Physics Conference Series*, edited by F. A. Aharonian and H. J. Völk, American Institute of Physics Conference Series Vol. 558, pp. 221–233, 2001, arXiv:astro-ph/0101233.
- [207] C. Distefano, D. Guetta, E. Waxman, and A. Levinson, Astrophys. J. **575**, 378 (2002), arXiv:astro-ph/0202200.
- [208] Z. Ling, S. N. Zhang, and S. Tang, Astrophys. J. **695**, 1111 (2009), arXiv:0901.2990.
- [209] A. J. Mioduszewski, M. P. Rupen, R. M. Hjellming, G. G. Pooley, and E. B. Waltman, Astrophys. J. **553**, 766 (2001), arXiv:astro-ph/0102018.
- [210] K. I. I. Koljonen, D. C. Hannikainen, M. L. McCollough, G. G. Pooley, and S. A. Trushkin, Mon. Not. Roy. Astron. Soc. **406**, 307 (2010), arXiv:1003.4351.
- [211] Fermi LAT Collaboration *et al.*, Science **326**, 1512 (2009).
- [212] AGILE Collaboration, M. Tavani *et al.*, Nature **462**, 620 (2009), arXiv:0910.5344.
- [213] A. Bulgarelli *et al.*, Astron. & Astrophys. **538**, A63 (2012), arXiv:1111.4960.
- [214] IceCube Collaboration, R. Abbasi *et al.*, Astrophys. J. **732**, 18 (2011), arXiv:1012.2137.
- [215] IceCube collaboration, R. Abbasi *et al.*, Astrophys. J. **763**, 33 (2013), arXiv:1210.3273.
- [216] G. Dubus, B. Cerutti, and G. Henri, Mon. Not. Roy. Astron. Soc. **404**, L55 (2010), arXiv:1002.3888.
- [217] G. E. Romero, D. F. Torres, M. K. Bernado, and I. Mirabel, Astron. & Astrophys. **410**, L1 (2003), arXiv:astro-ph/0309123.
- [218] AGILE Collaboration, G. Piano *et al.*, Astron. & Astrophys. **545**, A110 (2012), arXiv:1207.6288.
- [219] D. F. Torres and A. Reimer, Astron. & Astrophys. **528**, L2 (2011), arXiv:1102.0851.

- [220] S. A. Colgate, *Astrophys. J.* **232**, 404 (1979).
- [221] M. Kachelriess and D. V. Semikoz, *Phys. Lett.* **B634**, 143 (2006), arXiv:astro-ph/0510188.
- [222] G. Ghirlanda *et al.*, *Mon. Not. Roy. Astron. Soc.* (2013), arXiv:1307.7704.
- [223] D. Lazzati, M. Villeneuve, D. Lopez-Camara, B. Morsony, and R. Perna, (2013), arXiv:1309.1473.
- [224] K. Asano and P. Mészáros, *JCAP* **1309**, 008 (2013), arXiv:1308.3563.
- [225] K. Murase and K. Ioka, *Phys. Rev. Lett.* **111**, 121102 (2013), arXiv:1306.2274.
- [226] A. Tricomi, Results from LHCf Experiment, in *European Physical Journal Web of Conferences*, European Physical Journal Web of Conferences Vol. 28, p. 2003, 2012, arXiv:1202.2083.
- [227] A. M. Atoyan and C. D. Dermer, *Astrophys. J.* **586**, 79 (2003), arXiv:astro-ph/0209231.
- [228] L. A. Anchordoqui, H. Goldberg, F. Halzen, and T. J. Weiler, *Phys. Lett.* **B593**, 42 (2004), arXiv:astro-ph/0311002.
- [229] A. Einstein, *Ann. Phys.* **354**, 769 (1916).
- [230] E. Hubble, *Proceedings of the National Academy of Science* **15**, 168 (1929).
- [231] A. Weigert, H. J. Wendker, and L. Wisotzki, *Astronomie und Astrophysik: Ein Grundkurs* (Wiley-VCH, 2009).
- [232] WMAP Collaboration, E. Komatsu *et al.*, *Astrophys. J. Suppl.* **192**, 18 (2011), arXiv:1001.4538.
- [233] WMAP Collaboration, C. Bennett *et al.*, (2012), arXiv:1212.5225.
- [234] WMAP Collaboration, G. Hinshaw *et al.*, (2012), arXiv:1212.5226.
- [235] Planck Collaboration, P. Ade *et al.*, (2013), arXiv:1303.5076.
- [236] D. W. Hogg, *ArXiv Astrophysics e-prints* (1999), arXiv:astro-ph/9905116.
- [237] K. N. Abazajian *et al.*, *Astrophys. J. Suppl.* **182**, 543 (2009), arXiv:0812.0649.
- [238] A. Einstein, *Ann. Phys.* **322**, 891 (1905).

A. NeuCosmA

The C-code NeuCosmA (“Neutrinos from Cosmic Accelerators”) is designed to efficiently calculate photohadronic interactions and weak decays. It uses the factorization of the photohadronic interactions of the model “Sim-B” from Ref. [139], which is based on the physics of SOPHIA [131] and accurately reproduces the results by SOPHIA for power law-like spectra. The code itself is split into several modules for the different types of effects, *e.g.* for photohadronic interactions, weak decays, relativistic boosts, or steady state calculations. The whole calculation is divided into several steps, which can be turned on and off individually. We will give a short description of them, with more details on each step to be found in Ref. [142]. The basic calculation flow can be seen in Fig. A.1.

To start our photohadronic interaction calculation, our code needs steady spectra which are isotropic in the frame of calculation. Hence, to be consistent with our description of the GRB model in chapter 2, we denote these spectra as N'_p and N'_γ . These are then used to calculate the injection spectra of secondary mesons $Q'_b(E'_b)$ (in $[\text{GeV}^{-1} \text{cm}^{-3} \text{s}^{-1}]$), using

$$Q'_b(E'_b) = \int_{E'_b}^{\infty} \frac{dE'_p}{E'_p} N'_p(E'_p) \int_{\frac{\epsilon_{\text{th}} m_p c^2}{2 E'_p}}^{\infty} \epsilon' N'_\gamma(\epsilon') R_b(x, y) \quad . \quad (\text{A.1})$$

In this formula, the variable $x = E'_b/E'_p$ is the fraction of proton energy going into the secondaries, while $y \equiv (E'_p \epsilon') / (m_p)$ is related to the center of mass energy. The energy ϵ_{th} is the threshold photon energy in the proton rest frame above which photohadronic interactions can occur, compare to Fig. 2.1. The response function $R_b(x, y)$ is what factorizes the interaction cross section into different interaction types, for details see Ref. [139].

Since most of the secondary particles are charged and strong magnetic fields are assumed to be present inside the source, the secondary particles can actually lose energy due to synchrotron cooling (or other processes) before decaying. Assuming continuous energy losses, the kinetic equation for particle spectra is given by (see, *e.g.*, Ref. [227])

$$\frac{\partial N'(E')}{\partial t'} = \frac{\partial}{\partial E'} (-b(E') N'(E')) - \frac{N'(E')}{t'_{\text{esc}}} + Q'(E') \quad , \quad (\text{A.2})$$

where t'_{esc} is the characteristic escape time, b is the energy loss rate, and N' and Q' are the steady and the injection spectra, respectively. In principle, this approach is quite similar to the one used to model CR propagation in Eq. (4.4). For the particle

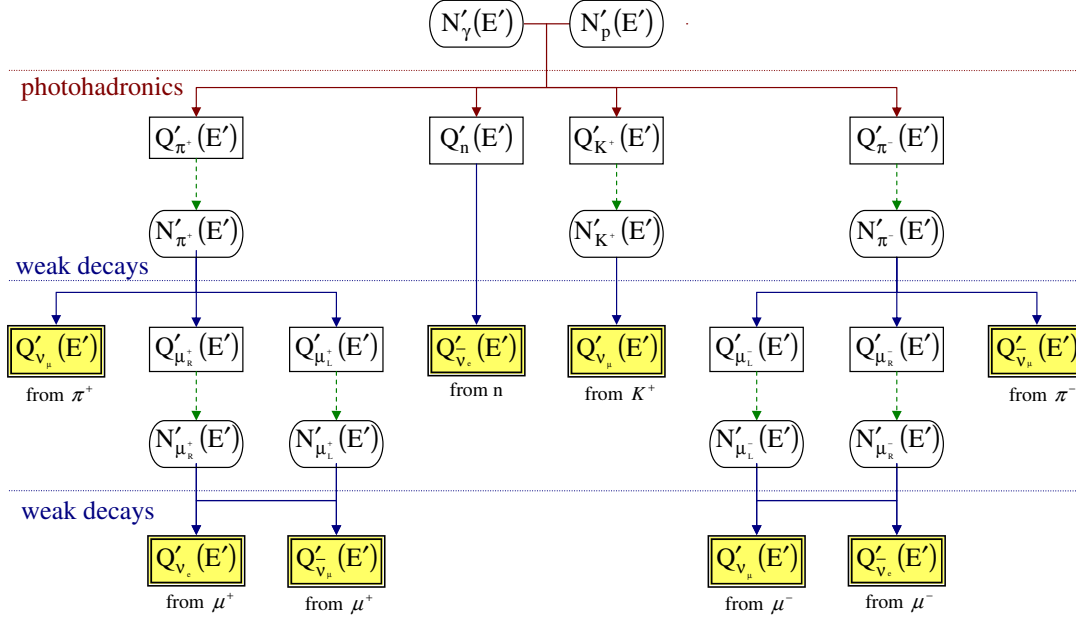


Figure A.1.: Basic calculation flow of the NeuCosmA code. The spectra denoted with $N'(E')$ are steady spectra in $[\text{GeV}^{-1} \text{cm}^{-3}]$, while $Q'(E')$ denote (injection) spectra per unit time (in $[\text{GeV}^{-1} \text{cm}^{-3} \text{s}^{-1}]$). The photohadronic interactions and the weak decays always need steady spectra as input, and return injection spectra; depicted as solid arrows. By balancing the injection against the losses as in Eq. (A.3), these injection spectra are in turn used to calculate new steady spectra; depicted as dashed arrows. The different neutrino spectra resulting from this calculation are highlighted with yellow boxes.

spectra, we however assume the special case of balance between losses (including escape) and gains through injection, leading to $\partial N'(E')/\partial t' = 0$. The kinetic equation from Eq. (A.2) then simplifies to

$$Q'(E') = \frac{\partial}{\partial E'} (b(E') N'(E')) + \frac{N'(E')}{t'_{\text{esc}}} \quad , \quad (\text{A.3})$$

and we can easily obtain the steady state spectra N' from the injection spectra Q' . This also allows us to treat the losses of the secondary particles individually; see dashed arrows in Fig. A.1. Moreover, in our calculation, steady spectra are always needed as inputs for photohadronic interaction calculations or the calculation of weak decays (solid arrows in Fig. A.1). Hence, this additional step to obtain N' is always needed between the results of photohadronic interactions and weak decays. While more details on this can be found in Ref. [142], there is one important difference to the approach from said reference. Here, in the case of GRBs, we do not discuss where the steady spectra for protons and photons actually come from or how realistic it is that these spectra are steady, since we are more interested in the neutrino results of the calculation. This need of steady spectra is, however, a major drawback. A realistic simulation would have to self-consistently solve the kinetic equation for the particles, as in Eq. (A.2), even for protons and photons. On the other hand, the additional requirement helps to speed up the code. Since neutrino measurements so far do not have the same time resolution as measurements in photons, it is sufficient to choose speed over accuracy.

The weak decays of the secondary particles are considered in additional steps of our calculation. For our code, we have implemented a scaling approach, based on Lipari et al. [124], which is generally applicable for the decay of ultra-relativistic parents of type a into daughter particles of type b . The resulting energy spectra of particle b

$$Q'_b(E'_b) = \sum_a \int_{E'_b}^{\infty} dE'_a N'_a(E'_a) t'_{a,\text{dec}}{}^{-1}(E'_a) \frac{1}{E'_a} F_{a \rightarrow b} \left(\frac{E'_b}{E'_a} \right) \quad (\text{A.4})$$

is a sum over all parents a using the scaling functions $F_{a \rightarrow b}$. The different functions for pions, kaons, and helicity-dependent muons are taken from Ref. [124], complemented by the scaling of π^0 -decay from Ref. [146] and neutron decay based on Ref. [228].

B. Cosmology and special relativity effects

In this section, we will take a look at the mathematical framework, currently used to describe our universe. More precisely, we will focus on the cosmological model which is currently used, based on field equations and the concept of general relativity which A. Einstein derived in 1916 [229]. With the appropriate metric, these field equations can be solved to give comparably simple solutions. Based on astronomical observations, it can be inferred that on large scales (above 100 Mpc) the universe is homogeneous and isotropic. To fulfill these attributes the metric of choice for our universe is the so-called Friedmann-Lemaître-Robertson-Walker (FLRW) metric

$$ds^2 = c^2 dt^2 - a(t)^2 [dr^2 + \Sigma(r)^2 d\Omega^2] \quad . \quad (\text{B.1})$$

In this representation, the factor $a(t)$ is the “scale factor”, which allows space of the universe to grow (or theoretically shrink) over the time t , as already observed by Hubble in 1929 [230]. Also, the differential of the solid angle can be expressed as $d\Omega^2 = d\theta^2 + \sin^2\theta d\phi^2$. Furthermore, the metric includes a factor to allow the spacetime to be curved, namely through $\Sigma(r)$. The values for $\Sigma(r)$ depend on the sign and value of the curvature, and, using the same hyperspherical coordinates as for the metric in Eq. (B.1), can be expressed as

$$\Sigma(r) = \begin{cases} \sqrt{-k} \sinh(r/\sqrt{-k}) & \text{for } k < 0 \\ r & \text{for } k = 0 \\ \sqrt{k} \sin(r/\sqrt{k}) & \text{for } k > 0 \end{cases} \quad (\text{B.2})$$

with k being associated with the curvature radius squared.¹

The FLRW metric can be used to solve the Einstein field equations. The solutions obtained for the metric lead to the Friedmann equations

$$\left(\frac{\dot{a}}{a}\right)^2 = \frac{8\pi G}{3} \rho - \frac{k c^2}{a^2} + \frac{\Lambda c^2}{3} \quad , \quad (\text{B.3})$$

$$2 \frac{\ddot{a}}{a} = -\frac{8\pi G}{c^2} p - \frac{k c^2}{a^2} + \Lambda c^2 - \left(\frac{\dot{a}}{a}\right)^2 \quad . \quad (\text{B.4})$$

In these equations, the homogeneous density ρ and pressure p of the universe are used as parameters. Moreover, the equations include Newton’s constant of gravity, given by G , as well as Λ , which is a relic quantity once introduced by Einstein himself to obtain a static universe. Once considered by Einstein as his “greatest blunder”,

¹Technically the choice of units for k also effects the units of the other parameters. When k is assumed to be a length⁻², then r has the unit length and $a(t)$ is unitless, which is the physically intuitive choice. However, if $k \in \{+1, 0, -1\}$ (and unitless), then r is unitless as well and $a(t)$ has to be a length.

Description	Symbol	<i>WMAP</i> +BAO+ H_0	<i>Planck</i>
Hubble constant	H_0	$70.4_{-1.4}^{+1.3} \text{ km s}^{-1} \text{ Mpc}^{-1}$	$67.4 \pm 1.4 \text{ km s}^{-1} \text{ Mpc}^{-1}$
Baryon density	Ω_b	0.0456 ± 0.0016	0.04858 ± 0.00073
Dark matter density	Ω_c	0.227 ± 0.014	0.2633 ± 0.0068
Dark energy density	Ω_Λ	$0.728_{0.016}^{+0.015}$	0.686 ± 0.020
Total density	Ω_{tot}	$1.0023_{-0.0054}^{+0.0056}$	

Table B.1.: Excerpt of the used cosmological parameters taken from Ref. [232], the *WMAP* seven-year report. The *Planck* data [235] is given for comparison reasons, to quantify the experimental progress during the time of this thesis. Except for Hubble’s constant all quantities are dimensionless. The first four values are obtained for a flat ($k = 0$) universe while the last entry, Ω_{tot} , is obtained with the possibility of $k \neq 0$. The *Planck* results do not include the total density as a parameter, but only state that the curvature is consistent with a flat spacetime on the percent level. For details on the acquisition, see Refs. [232, 235] and references therein. We will use simplified values derived from the *WMAP* values above. We set $H_0 = 70.5 \text{ km s}^{-1} \text{ Mpc}^{-1}$, the matter density $\Omega_m = \Omega_b + \Omega_c = 0.27$ and $\Omega_\Lambda = 0.73$. As can be seen from Fig. 5.1, the distances are hardly affected by the change of parameters, and the error from using the older values is not too high.

it is still used in current cosmological models since fits to the cosmic microwave background (CMB) give the best results with models including this Λ component. Due to this, the Λ is the namesake for current models. The so-called Λ CDM-model is the currently favored model, which includes “cold” (non-relativistic) dark matter apart from the Λ term. Normally, the Friedmann equations are re-written to define a model by a set of energy densities and Hubble’s constant H , *i.e.* the first Friedmann equation, given in Eq. (B.3), can be transformed to include the (vacuum) energy density ρ_Λ . Using $\rho_\Lambda = \Lambda c^2 / (8\pi G)$, the equation can be simplified to

$$\left(\frac{\dot{a}}{a}\right)^2 = \frac{8\pi G}{3} (\rho + \rho_\Lambda) - \frac{k c^2}{a^2} . \quad (\text{B.5})$$

In the above equation, the density ρ is short-hand for the matter (ρ_m) as well as the radiation density (ρ_γ). Note, however, that all densities can have a time dependence and only today’s values can be obtained from measurements, see Ref. [231]. The radiation density ρ_γ is proportional to t^4 when going back in time, while the matter density ρ_m is $\propto t^3$ and ρ_Λ is constant. Another step to improve the readability of the densities is to express everything in units of the critical density $\rho_{0,\text{crit}} = 3 H_0^2 / (8\pi G)$, where the index 0 denotes today’s ($t = t_0$) values. The dimensionless densities are normally denoted by Ω , and results from the satellite experiments *Wilkinson Microwave Anisotropy Probe (WMAP)* and *Planck* have set quite firm boundaries on the current densities. In our work, we used the results obtained by *WMAP* after 7 years of operation [232], neglecting the final update after 9 years of operation, see Refs. [233, 234], and also the recently published first *Planck* results, see Ref. [100] for an overview. This was done mainly due to consistency reasons, as only the 7 yr data of *WMAP* was available at the beginning of our work in 2010. In Table B.1, we give an excerpt of the values derived from the seven-year data of *WMAP* (and other experiments), as well as the results for *Planck* data for comparison reasons. The effect of using the slightly changed cosmological values is rather small. As can be seen from the values given in Table B.1, the energy density in the universe

is dominated by “dark energy” ($\Omega_\Lambda \approx 0.73$) and matter ($\Omega_m = \Omega_b + \Omega_c \approx 0.27$). Note that these values are obtained for a flat spacetime, leading to $k = 0$ and $\Omega_{\text{tot}} = 1$. For our simulations, we will use the aforementioned approximated values, and not the ones from the table itself. Compared to the other two densities the radiation density Ω_γ is negligible. For this reason, we have omitted this density from Table B.1. Additionally, note that the best-fit value of Ω_{tot} is obtained by relaxing the constraints on k , hence adding an additional degree of freedom. Still, the resulting best-fit is still close enough to unity to claim that our spacetime is flat.

An additional effect of the cosmic expansion is a shift in energy. Photons, for example, are observed at a lower frequency than they were emitted. As lower frequencies/longer wavelengths in the optical band mean shifting photons towards the “red” part of the spectrum, this whole process is considered to be a “red-shift”. Hence, as this principle of shifting photons to lower energies can be applied to all energy ranges, the redshift z was defined as

$$z = \frac{\lambda_{\text{obs}} - \lambda_{\text{emit}}}{\lambda_{\text{emit}}} \quad (\text{B.6})$$

with the observed wavelength given by λ_{obs} , and the emitted one by λ_{emit} . The scale factor $a(t)$ can be connected to z in our expanding spacetime by

$$a(t) = \frac{1}{1+z} \quad , \quad (\text{B.7})$$

assuming that $a(t = t_0) = 1$. When the redshift z can be measured, it is possible to calculate the distance between the observer and an object by utilizing the flat Λ CDM cosmology framework. Considering that the spacetime is expanding with $a(t)$, it is useful to have a distance measure² which already corrects for the cosmological expansion. Using these requirements as a starting point, the so-called comoving distance d_{com} is defined with respect to z as

$$d_{\text{com}}(z) = \frac{c}{H_0} \int_{\frac{1}{1+z}}^1 \frac{da}{\sqrt{\Omega_m a + \Omega_\Lambda a^4}} \quad . \quad (\text{B.8})$$

Here, c is the speed of light in vacuum, while the other factors are taken from Table B.1. Note that we use the rounded values, $\Omega_m = 0.27$ and $\Omega_\Lambda = 0.73$, for the densities in our actual calculations. Moreover, from this definition of d_{com} we can extract two definitions around the Hubble constant. On the one hand, we can extract the Hubble parameter depending on redshift³

$$H(z) = H_0 \sqrt{\Omega_m(1+z)^3 + \Omega_\Lambda} \quad . \quad (\text{B.9})$$

²A very nice overview of the different distance measures in cosmology can be found in Ref. [236]. Even though it is mostly for older cosmological parameters and “only” an online publication, it is still very useful resource for understanding why several different distance measures are actually needed in cosmology.

³This is done by substituting the integration over da with one over dz , and then combining H_0 with the denominator inside the integral.

On the other hand, we can also define the prefactor of the integral as the Hubble length

$$d_H = \frac{c}{H_0} \simeq 4255 \text{ Mpc} \quad . \quad (\text{B.10})$$

Due to the expansion of space as well as the energy shift described in Eq. (B.6), objects seem further away than they actually are according to d_{com} , when observed in photons. Hence, the classic relation of luminosity L_{iso} (in $[\text{erg s}^{-1}]$) and flux F (in $[\text{erg s}^{-1} \text{ cm}^{-2}]$),

$$L_{\text{iso}} = 4\pi d^2 \cdot F \quad , \quad (\text{B.11})$$

needs to be adapted to accommodate the additional effects of an expanding space-time. The main reasoning behind this formula is that a source radiating at a luminosity L_{iso} should give rise to a flux F at distance d . Since photons additionally lose energy due to the cosmological redshift as well as being affected by (cosmic) time dilation, the formula needs to be modified when using d_{com} as distance measure:

$$L_{\text{iso}} = 4\pi d_{\text{com}}^2 (1+z)^2 \cdot F \quad . \quad (\text{B.12})$$

To return to the initial form of the equation, given in Eq. (B.11), it is possible to define a “luminosity distance” d_L as

$$\begin{aligned} d_L &= (1+z) d_{\text{com}} \\ &= (1+z) \frac{c}{H_0} \int_{\frac{1}{1+z}}^1 \frac{da}{\sqrt{\Omega_m a + \Omega_\Lambda a^4}} \quad . \end{aligned} \quad (\text{B.13})$$

As a final remark on this topic, it should be noted the above mentioned calculations and distance measures only hold true on large scales. As mentioned during the introduction of the FLRW metric, the universe is assumed to be homogeneous and isotropic, which is not the case on scales below about 100 Mpc. The stars are not distributed evenly as can be seen by a simple observation such as looking into the night sky. Structures such as galaxies or even clusters of galaxies are anisotropic. They are gravitationally bound and move towards (or sometimes away from) one another, leading to Doppler shifts superposing the cosmological redshift. However, deep sky surveys, such as the Sloan Digital Sky Survey (SDSS) [237], have shown that on scales above 100 Mpc the universe is isotropic. This distance corresponds to a minimal redshift of about $z \simeq 0.024$, and no lower redshifts should be considered when discussing isotropic distributions.

Additionally, Einstein also discussed how quantities should transform from one frame of reference to another in 1905 [238]. Based on the two postulates that the speed of light is independent of the frame of reference and that physical laws and their effects are unchanged by the choice of the reference frame, the so-called theory of special relativity was developed. In said theory, changes of the frame reference are described by Lorentz boosts, which is especially important for the change of frames when one frame is moving (nearly) at the speed of light c relative to the other frame. In this case, additional effects, such as (relativistic) time dilation or length contraction, are the result of the Lorentz transformations. Since GRBs are

considered to be connected to ultra-relativistic shocks, these transformations are needed and a nice introduction into what transformations are relevant in case of GRBs can be found in the review by Meszaros [42].

We implicitly use the following boosts of time t , length (along the boost direction) r , and energy E throughout the work presented here:

$$d\tilde{t} = \Gamma dt' \quad (\text{time dilation}), \quad (\text{B.14})$$

$$\delta\tilde{r} = \Gamma^{-1} \delta r' \quad (\text{length contraction}), \quad (\text{B.15})$$

$$\tilde{E} = \Gamma E' \quad . \quad (\text{B.16})$$

Note that lengths perpendicular to the boost direction are unchanged. Hence, the volume is boosted as $d\tilde{V} = \Gamma^{-1} dV$. All other boosts can be derived from these basic relations.

Moreover, the measurement principles such as two photons need to be detected at the same time introduce an additional effect on the change of reference frame since there is no absolute simultaneity. Two photons which are emitted simultaneously in one frame are not necessarily observed simultaneously in the other frame. This effect is dependent on the viewing angle of the observer onto the boost. Said dependence can be expressed by a Doppler factor \mathcal{D} , which is calculated as

$$\mathcal{D} = \frac{1}{\Gamma(1 - \beta \cos\theta)} \quad . \quad (\text{B.17})$$

Here, β is the velocity v in units of c , $\beta = v/c$, and θ is the viewing angle towards the direction of the boost. For GRBs with highly boosted jets ($\theta \leq \Gamma$), \mathcal{D} is roughly equivalent to Γ , *i.e.* it ranges from $\mathcal{D}(\theta = \Gamma) = \Gamma$ to $\mathcal{D}(\theta = 0) = 2\Gamma$. Hence, even though Doppler factors are actually needed for observed objects, plain Lorentz factors are still sufficient in case of GRBs as the error is at most only a factor two.

C. Photon-photon interactions

Since the resulting spectra from photohadronic interactions are closely related to the target photon spectra, a few general considerations on the photon spectra and the escape of high-energy photons are also needed for a self-consistent multi-messenger approach. In the following, we will discuss how the usage of a given spectrum affects the prediction of the resulting (secondary) spectra.

In principle, the maximal photon energy has a significant effect on photohadronic interactions. This is due to the photohadronic interaction cross-section only being non-zero above the threshold of 200 MeV photon energy in the proton rest frame. Hence, the maximal energy of the photon spectrum defines the minimal energy of the secondary spectrum, such as the neutrons or the neutrinos. While most studies with generic bursts normally assume an arbitrary cutoff, it is actually better to calculate the maximal photon energy based on the parameters of a burst. For actual observations, this problem is somewhat reduced by the observation of photons up to a certain maximum. For theoretical considerations, it is however essential to understand how the maximal photon energy is limited. In this respect, the pair production due to photon-photon interactions is normally used as the indicator to evaluate the possibility of photons to escape a source. The basic formula for the (inverse) $\gamma\gamma$ interaction length $l'_{\gamma\gamma}$ can be derived in the same way as the photohadronic interaction length $ct'_{p\gamma}$, see Eq. (2.14), as

$$l'_{\gamma\gamma}(\epsilon'_t) = \int_{-1}^{+1} \frac{d \cos \theta}{2} (1 - \cos \theta) \int_0^{\infty} d\epsilon'_\gamma \sigma_{\gamma\gamma}(\epsilon'_\gamma) \cdot n'_\gamma(\epsilon'_\gamma, \cos \theta) \quad (\text{C.1})$$

where ϵ'_t is the energy of the test photon and ϵ'_γ the energy of a target photon. The density of target photons is given by n'_γ , while θ is the incident angle between the test photon and a target photon. The photon-photon interaction cross-section $\sigma_{\gamma\gamma}$ already includes the contribution from the integration over ϕ . Moreover, all quantities are primed as they are in the SRF. This has the major advantage that the target photon density can be considered to be isotropic, removing the $\cos\theta$ -dependence from n'_γ . Additionally, it is normally assumed that even though the interaction cross-section $\sigma_{\gamma\gamma}$ first drops $\propto \log(\epsilon)/\epsilon$ above threshold and then rises slightly again, see Ref. [101], the drop-off of the target spectrum $dN_\gamma/dE \propto E^{-\alpha}$ is considered “fast enough” for $\sigma_{\gamma\gamma}$ to be assumed to be constant, as in Ref. [69]. As stated in said reference, the constant value is assumed to be $\sigma_{\gamma\gamma} = 3/16 \sigma_T$ with $\sigma_T = 0.665\,245\,8734(13) \cdot 10^{-24} \text{ cm}^2$, the Thompson cross-section. Therefore, we can insert the following parameterization of $\sigma_{\gamma\gamma}$ into Eq. (C.1):

$$\sigma_{\gamma\gamma}(\epsilon'_\gamma) = \begin{cases} 0 & \epsilon'_\gamma < \epsilon'_{\text{th}} \\ \frac{3}{16} \sigma_T & \epsilon'_\gamma \geq \epsilon'_{\text{th}} \end{cases}, \quad (\text{C.2})$$

where ϵ'_{th} is the threshold energy for $\gamma\gamma$ pair creation interactions, based on kinematics given by

$$\epsilon'_{\text{th}} = \frac{2m_e^2}{\epsilon'_t(1 - \cos\theta)} \quad . \quad (\text{C.3})$$

Even though it is theoretically possible to calculate the interaction length for arbitrary spectra with a numerical code, we will, for the sake of simplicity, still incorporate a further set of analytical tweaks. Namely, we will assume that the photon density n'_γ can be approximated by only the high-energy part, because the break energy $\epsilon'_{\gamma,\text{break}} \ll m_e (= 511 \text{ keV})$. Furthermore, we will assume that the standard upper photon index is $\beta_\gamma = 2$, which allows us to perform the integration over ϵ'_γ analytically. Because of this choice of β_γ the result will no longer be applicable to a realistic calculation with a distribution of the spectral indices, or for a calculation with actually observed parameters. However, for our calculations done in this work the result is sufficient. Moreover, the simplified result shown in Eq. (C.4), which is obtained using these steps, is similar to the analytical result from Ref. [69]. And finally, we do not include the assumed maximal photon energy of the spectrum, but keep the upper integration bound at ∞ . Technically, the spectrum of the test and the target photons is the same, and we are dealing with a self-absorption effect. Now, if the spectrum extended only to photon energies below 511 keV, there would be no self-absorption whatsoever, since the threshold energy would never be reached. Yet, since we do not know what the actual maximal energy inside the shock is (before absorption effects) we can leave it at ∞ . We know that the maximal photon energy must be limited from acceleration considerations/plasma physics, but this can be safely ignored as the result with ∞ is actually more conservative on the escaping maximal energy. With all these simplifications Eq. (C.1) can be reduced to the form

$$l'_{\gamma\gamma}(\epsilon'_t) \simeq \frac{1}{8} \sigma_{\text{T}} C'_\gamma \cdot \epsilon_{\gamma,\text{break}}'^2 \cdot \frac{\epsilon'_t}{m_e^2} \quad (\text{C.4})$$

with C'_γ being the normalization constant of the photon density. By comparing this interaction length to the size of the region from Eq. (1.4), it is possible to estimate if photons of an energy ϵ'_t can escape or not. When we now assume equality of both length scales, it is possible to obtain

$$\epsilon'_{t, \text{max}} = 8 \frac{(1+z) m_e^2}{\Gamma c t_v \cdot \sigma_{\text{T}} C'_\gamma \epsilon_{\gamma,\text{break}}'^2} \quad , \quad (\text{C.5})$$

which can now be used to calculate the threshold energy for photohadronic interactions using Eq. (2.3). Note that t_v is in the observer's frame. Moreover, the result obtained through Eq. (C.5) can be used to estimate, if the assumed parameters allow for bursts which are visible in a certain energy range, *e.g.* the *Fermi* LAT range (more than 30 MeV) or above 100 MeV.

Acknowledgements

I gratefully acknowledge the support of the GRK 1147 “Theoretical Astrophysics and Particle Physics” of the DFG.

I would like to thank Walter Winter for giving me the opportunity to carry on in this interesting field of particle astrophysics. For all the discussions, encouragements, and help throughout the last three years. I am grateful for the time working with Svenja Hümmer and for the fun we had while being partially overwhelmed by all the problems of the new code. Without your and Carlos Yaguna’s work on the photohadronic interactions, this one here would have never been possible. Also, I like to thank Mauricio Bustamante for enriching the project with new aspects (and new physics), lots of programming, and discussions about comics.

Moreover, I would like to thank Martin Krauß for all the explanations on mass generation for neutrinos, and Stephan Richter for all the lengthy discussions on plasma physics and why everything is way more complicated in reality. Furthermore, I would like to thank Christoph Uhlemann for all the insight on mathematical physics which enriched (and lengthened) our lunch breaks.

I am obliged to express my gratitude towards Werner Porod and the other professors (and post-docs) of the GRK as well as my fellow PhD students. You made this time worth the while.

I am thankful for Julia Schmid’s initiative to optimize the ANTARES GRB analysis based on our NeuCosmA code, and for the collaboration for going along with it.

Also, I would like to thank Eli Waxman, Dafne Guetta, Amyad Spector, and all the other guys and girls from the Weizmann Institute for the great time there. It was really fascinating to work with you.

Moreover, I am grateful for my time at the Wisconsin IceCube Particle Astrophysics Center. I have to thank Francis Halzen and Markus Ahlers for giving me the opportunity to be a guest at the “heart” of IceCube. Also, Nathan Whitehorn, Claudio Kopper, Naoko Kurahashi Neilson, Ben Riedel, and all the rest of the people in Madison.

And last but not least, I like to thank my parents and, especially, my wife, Silvi, for all their love and support.

Para ti, mi vida.

Eidesstattliche Erklärung

Hiermit erkläre ich, Philipp Baerwald, geboren am 23.04.1986 in Marburg, an Eidesstatt, diese Arbeit selbstständig und ohne unlautere Hilfe angefertigt und keine anderen als die angegebenen Quellen und Hilfsmittel verwendet zu haben.

Würzburg, 30.09.2013